1995

Oxidation and creep behavior of Mo5Si3 based materials

Mitchell Karl Meyer
Iowa State University

Oxidation and creep behavior of Mo_5Si_3 based materials

by

Mitchell Karl Meyer

A Dissertation Submitted to the

Graduate Faculty in Partial Fulfillment of the

Requirements for the Degree of

DOCTOR OF PHILOSOPHY

Department: Materials Science and Engineering
Major: Ceramic Engineering

Approved:

Signature was redacted for privacy.

In Charge of Major Work

Signature was redacted for privacy.

For the Major Department

Signature was redacted for privacy.

For the Graduate College

Iowa State University
Ames, Iowa

1995

TABLE OF CONTENTS

CHAPTER 1: GENERAL INTRODUCTION

I. Dissertation Organization

This dissertation is written in an alternate format. The dissertation is composed of three original manuscripts, preceeded by a general introduction and followed by a general conclusion. References cited within each manuscript are located immediately after the manuscript. References cited within the general introduction and general conclusion follow the general conclusion.

The general introduction gives a broad overview of the driving force behind this research, as well as an overview on previous research into Mo_5Si_3 based materials and related topics. Also included in the general introduction is information on processing and properties not included in the manuscripts for the sake of brevity.

The first manuscript, "Oxidation behavior of Boron Modified Mo_5Si_3 at 800°-1300°C," was submitted to *The Journal of the American Ceramic Society* in December of 1994. The second manuscript, "Development of Oxide Scales on Mo-Si-B Intermetallics at 600°-1075°C," will be submitted to *The Journal of the American Ceramic Society* in 1995. The third manuscript, "Compressive Creep Behavior of Sintered Mo_5Si_3 with the Addition of Boron," will also be submitted to *The Journal of the American Ceramic Society* in 1995.

The general conclusion section summarizes the results of the manuscripts and the general introduction, and gives suggestions for future research.

Although all three papers are largely the work of the dissertation author, the work could not have been completed without the contributions of the co-authors. Dr. Mufit Akinc has made a significant contribution as major professor and appears as a co-author on all three papers. Dr. Matthew Kramer was responsible for help in creep testing and TEM studies and interpretation and appears as co-author in Chapter 4.

II. Background

High temperature materials are the enabling technology for many next generation technological applications. The most widely repeated example is that of turbine engines, where a higher operating temperature allows higher specific power output (power output /mass of engine) and lower specific fuel consumption (mass fuel consumed/unit power output). For example, an experimental 693 kW turboprop engine was retrofitted with a partially ceramic hot end that allowed for a 200°C rise in turbine inlet temperature. A 30% power increase and 7% decrease in fuel consumption were recorded[1]. Another example is the ATTAP ceramic turboshaft engine developed by General Motors and Allison to run at a turbine inlet temperature of 1371°C. The engine was projected to have a 30% fuel economy increase when used in place of a standard 2.5 L four cylinder engine.

Other applications include electric high temperature furnace elements, turbocharger rotors, diesel engine exhaust particulate filters, jet engine exhaust and afterburner components, high temperature spray nozzles, hot extrusion dies, piston engine components, and high temperature heat exchangers. As an example, consider jet engine afterburner components. Exhaust gas temperatures can reach 1700°C with afterburners on[2]. Normally the afterburner components are cooled using engine bypass air. If this air flow can be eliminated from afterburner and exhaust components and used instead as combustion air, performance gains will result.

Intermetallic compounds as a group hold promise as high temperature structural materials. Many metals combine with other metals or metalloids to form compounds with desirable properties such as high melting point, high temperature creep resistance, high temperature oxidation resistance, and high stiffness. Most intermetallic research to date has been directed toward synthesis of the titanium, iron, and nickel aluminides. Transition and

refractory metal silicide intermetallic compounds are a group of materials that, with a few exceptions, have been largely unexplored in terms of properties and phase relations.

One well characterized silicide intermetallic is molybdenum disilicide. The most common type of heating elements used above 1500°C in air are molybdenum disilicide ($MoSi_2$) elements. Although this material is far superior for this use than others, it still has shortcomings. $MoSi_2$ heating elements suffer from dimensional instabilty above 1200°C due to a high creep rate, and will creep under their own weight. The maximum use temperature is 1700°C. Below 800°C the elements are subject to disintegration by oxidation 'pesting'. The high creep rate of $MoSi_2$ precludes this material from use as a structural component above 1000°C. A material with traits similar to $MoSi_2$, but with an extended range of use temperatures, would be extremely useful to industry.

Figure 1 shows creep data for several molybdenum disilicides at 1200°C in compression[3]. As mentioned above, poor high temperature creep resistance is regarded as a major shortcoming of $MoSi_2$ for use as a high temperature structural material. In this plot, points to the lower right are most desirable in a material for high temperature use. Also shown in the plot is data for creep resistance of an Mo_5Si_3 based material. Figure 1 shows that the creep rate of the Mo_5Si_3 based material is lower than that of even whisker reinforced $MoSi_2$ at high stress levels.

Unfortunately, Mo_5Si_3 has been shown by several studies to have poor oxidation resistance. Materials engineering offers at least two possible solutions to obtaining a molybdenum silicide that has both high temperature creep resistance and high temperature oxidation resistance. The first possibility is to move the molybdenum:silicon ratio to a range between 1:2 and 5:3. This creates a two phase material that retains some of the superior oxidation resistance of $MoSi_2$ and may provide better creep properties. Although there is a

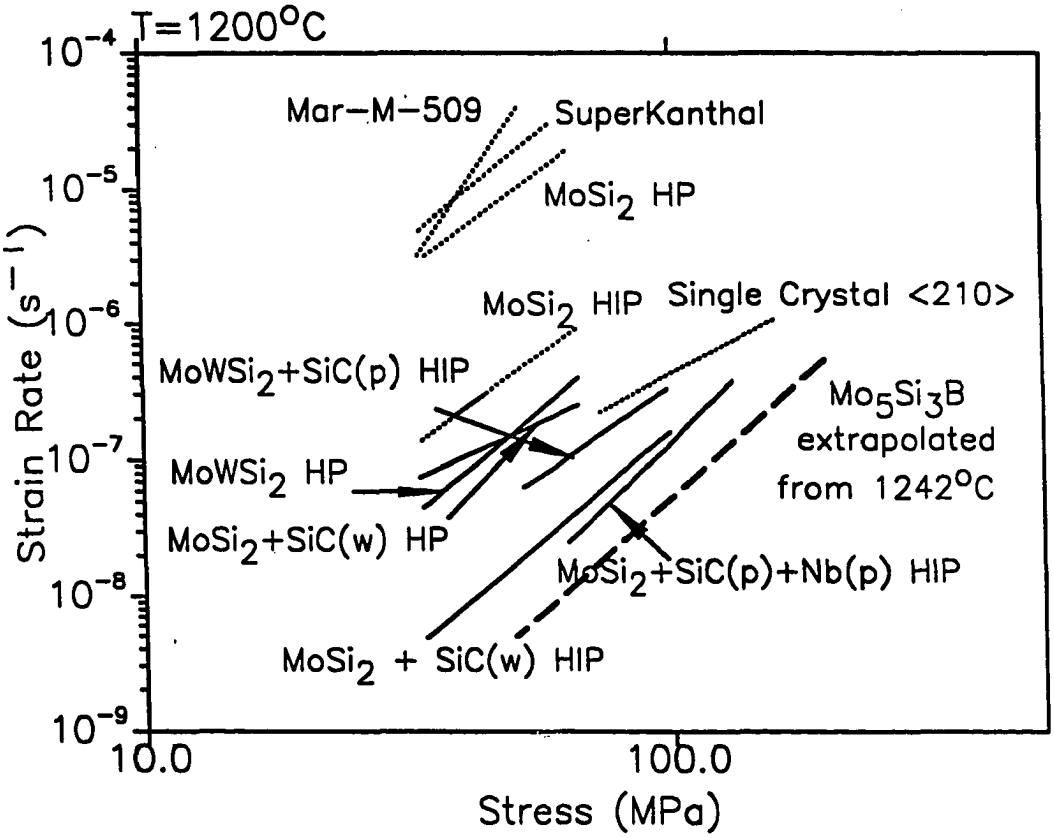

Figure 1. Comparison of creep rates of a boron modified Mo_5Si_3 based material with several $MoSi_2$ based monoliths and composites

slight melting point depression, the eutectic composition at 53 weight percent silicon can be exploited to create a natural 'in situ' composite material.

Another possible route to obtaining an oxidation resistant material is via third element additions to the 5:3 compound. Boron has been shown in this work to increase oxidation resistance of Mo_5Si_3, up to 5 orders of magnitude at 1200°C. This increase in oxidation resistance comes with a negligible decrease in creep resistance, as shown in Figure 1.

The development and characterization of a monolithic silicides with improved creep resistance is a broad topic currently being at investigated in our group. Ti_5Si_3 and Mo_5Si_3 based materials were chosen for further study based on preliminary screening tests. Mo_5Si_3 doped with carbon and boron and $Mo_5Si_3/MoSi_2$ eutectic compositions were considered as candidate Mo_5Si_3 based materials. Boron modified Mo_5Si_3 was found to have oxidation resistance superior the other compositions tested, and was chosen for further study of creep resistance and limited mechanical properties testing. The oxidation and creep behavior of boron modified Mo_5Si_3 is the primary emphasis of this work

III. Literature Review

(1) Mo_5Si_3 Crystal Structure and Properties

Refractory (Mo, W, Ta) metals form only a few compounds with silicon along the binary composition range. Figure 2 shows the molybdenum-silicon phase diagram, with small terminal solid solubility ranges and three compounds. Of the three compounds, only $MoSi_2$ has been well characterized. Mo_5Si_3 (in the absence of impurities) has a tetragonal crystal structure of space group I4/mcm (No. 140 [4]). The unit cell is large and complex, as shown in Figure 3, a view down the c axis of the unit cell. The unit cell is composed of four formula units, and is body centered.

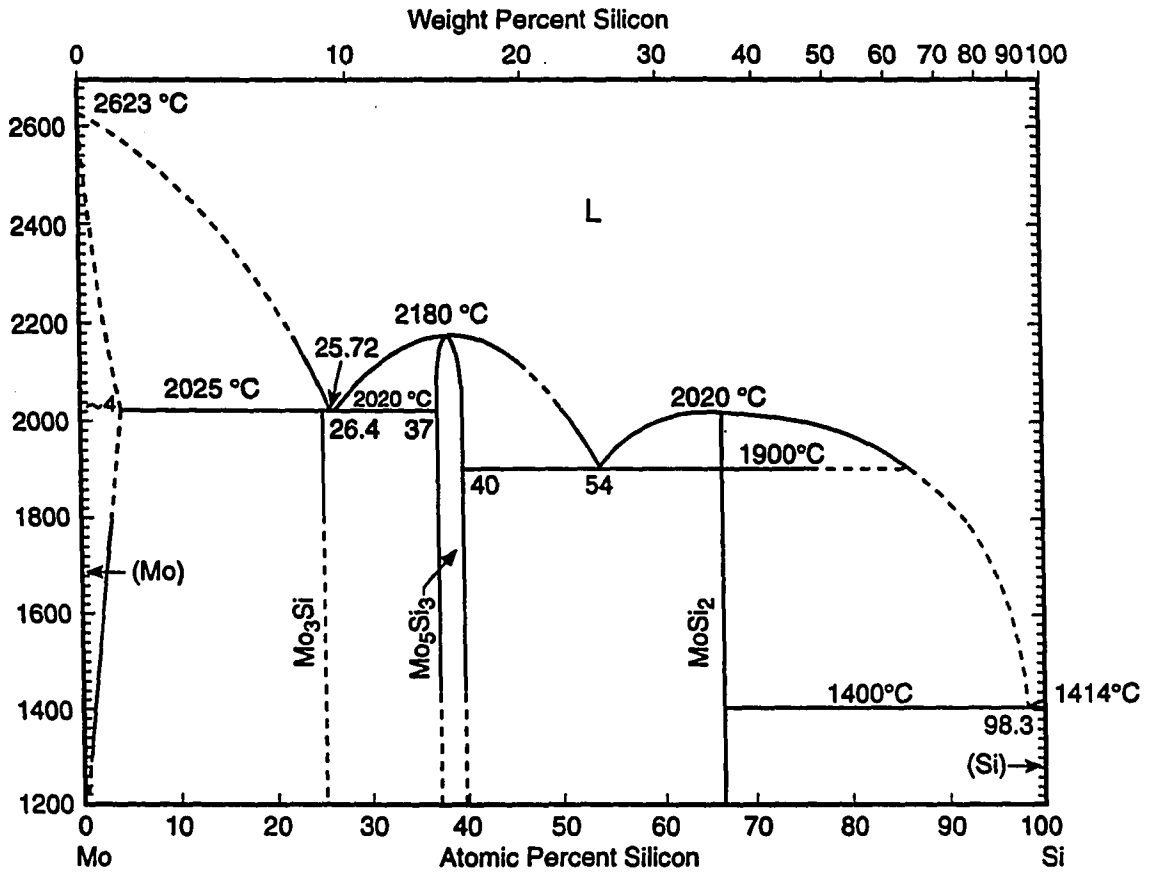

Figure 2. Mo-Si binary phase diagram.

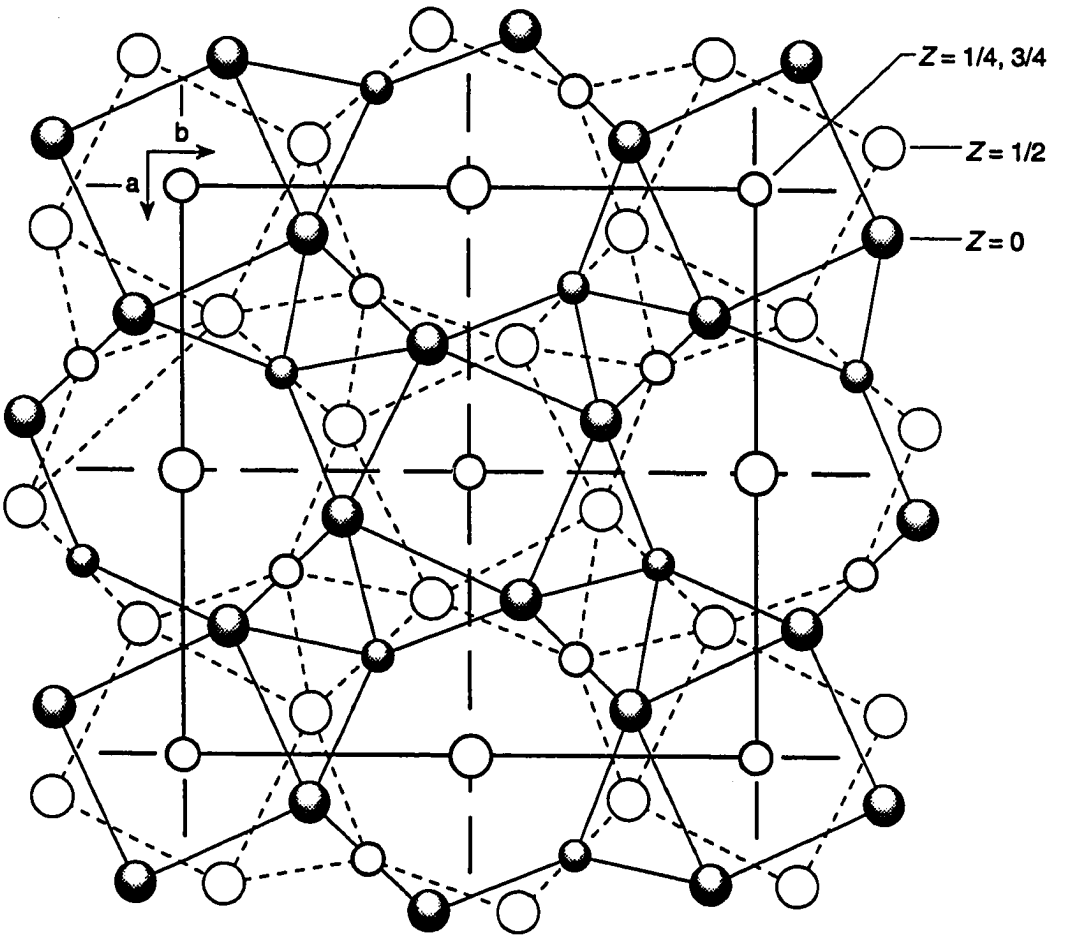

Figure 3. [001] projection of Mo_5Si_3 unit cell. W_5Si_3 prototype, space group number 140 (I4/mcm). Unit cell contains four Mo_5Si_3 formula units. Large open circles are molybdenum at Z=½, large shaded circles are molybdenum at Z=0. Small open circles are silicon at Z=¼, ¾, small shaded circles are silicon at Z=0.

Because silicon carbide fibers and whiskers are used as reinforcement for $MoSi_2$, there has been some recent interest in the Si-C-Mo ternary phase equilibria. Synthesis of Mo_5Si_3 was first claimed by Brewer[5], et al., who identified the stoichiometry of the compound as Mo_3Si_2 . The ternary Mo-Si-C phase, which has a carbon stabilized hexagonal structure, was first reported by Nowotny[6], et al. (Metal-Si-C phases of the hexagonal Mn_5Si_3 structure (No. 193) are now known as Nowotny phases.) Note that although Mo_5Si_3C was discovered as a ternary phase, the binary phase was still considered to be Mo_3Si_2. Aronsson[7], identified the correct stoichiometry as Mo_5Si_3 and crystal structure as body centered tetragonal (No. 140), and another neutron diffraction study several years later confirmed these findings.[8] Parthe' et al [9] studied the structure of $Mo_{4.8}Si_3C_{0.6}$ by neutron diffraction. Parthe' concluded that the space group of the ternary compound was No. 193, with Mn_5Si_3 as the prototype. Interest in the hexagonal stabilization of compounds with the W_5Si_3 structure by ternary element additions led to the generation of an isothermal (1600°C) Mo-Si-B phase diagram, as shown in Figure 4.

In 1957 Searcy[10] reviewed what was then known about the oxidative stability of silicides. Searcy noted that Mo-Si compounds containing "nearly 50% [atomic] molybdenum" were oxidatively stable. Cherniak et al.[11] found that when heated above 1600°C in vacuum, $MoSi_2$ decomposed by loss of silicon to form Mo_5Si_3. When Mo_5Si_3 was formed as a surface coating, the rate of silicon loss was slowed. It was speculated that diffusion of silicon through the 5:3 phase is much slower than diffusion of silicon through $MoSi_2$. At 1900°C, the authors reported that the Mo_5Si_3-$MoSi_2$ eutectic liquid was formed. On cooling, the eutectic structure was reported to form cracks. The weight loss data correlated well with the partial presure of silicon above $MoSi_2$ as measured by Searcy and Tharp.[12] No data on material purity was given. Maloy, et al.[13] observed a large mass loss

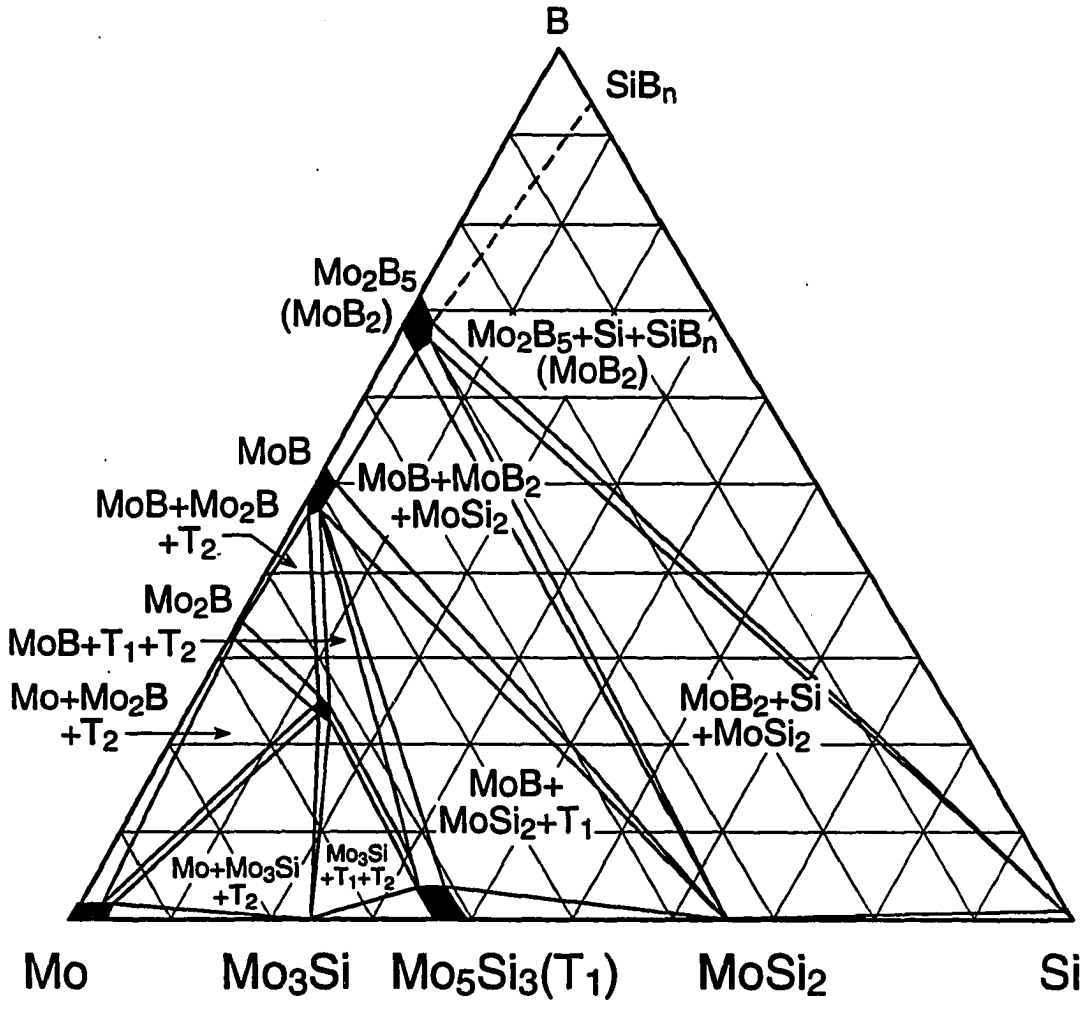

Figure 4. Mo-Si-B ternary phase diagram.

when hot pressing carbon doped $MoSi_2$ at 1830°C in argon. A sample with 2 wt% carbon lost 20% weight, and a sample with 4 wt% carbon lost 47% weight. The starting $MoSi_2$ contained 14 vol% (2.8 wt%) SiO_2 prior to hot pressing, and this large weight loss could not be attributed solely to the reduction of silica (SiO_2) to form SiC, CO(g), and SiO(g). The proposed mechanism of mass loss was oxidation of molybdenum due to catalyitic activity of carbon. No analysis was presented to support this theory. Anton and Shah[14] included $MoSi_2$ and Mo_5Si_3 in a group of seven intermetallic compounds selected for testing as a high temperature structural material. The results of these tests for Mo_5Si_3 are shown in Table I. Note the low creep rate of Mo_5Si_3 at 1200°C. The creep rate of $MoSi_2$ in the same paper was measured as 2.1×10^{-7} sec^{-1}. Mo_5Si_3 also
exhibited considerable ductility in this study, and an anomolously low activation energy for creep. The ultimate strength of the material was very low, with failure occurring by macroscopic cracking. The odd behavior of Mo_5Si_3 in this test can probably be explained by the microstructure of the test specimens. The ductility noted may have been due to the sliding of a loose assemblage of grains. The specimens were arc cast. Although no grain size or microstructural information was provided by the authors, arc melting generally produces a large grain (100-1000 μm) material that cracks transgranularly on cooling due to the thermal expansion anisotropy between the a and c axis of the tetragonal unit cell. Mo_5Si_3 prepared in this work by arc melting always exhibited large grain size and severe microcracking. It is quite possible then that the properties presented by Anton and Shah are not representative of the actual material properties of the compound, but represent the properties of microcracked specimens. Note that the creep data was obtained from compressive creep tests. In compressive creep testing, mode I cracks are forced to close, and creep results might not be seriously affected by the presence of microcracks.

Table I. Mechanical properties data for arc cast Mo_5Si_3

Property	Value	Notes
fracture strength	12 MPa	tensile
creep stress exponent (n)	1.9	1200°C
creep rate	4×10^{-8} sec^{-1}	1200°C, 69 MPa
creep activation energy	42 kJ/mole	1200°C, 69 MPa
ductile to brittle transition	none found	1200°C max.

Table II lists other relevant properties of molybdenum silicides. The value of thermal expansion coefficient is similar to that of alumina (7×10^{-6}/K). Young's modulus falls in the range between transition metals and ceramics. For example, carbon steel has a modulus of 200 MPa and aluminum oxide has a modulus of 390 MPa. In comparison to other intermetallics, Mo_5Si_3 also has a mid level Young's modulus (E_y). Values of E_y for other intermetallics[16] are 305 GPa for NiAl, 170 GPa for Ni_3Al, 215 GPa for Al_3Ti, 180 GPa for TiAl, 150 GPa for Ti_3Al, and 125 GPa for Fe_3Al. Microhardness (Vicker's hardness number, VHN) again falls in the range between metals and ceramics. The hardness of some alumina compositions is over 20 GPa (VHN), while metals fall in the range of 5-10 GPa (VHN). Fracture toughness is on the same level as dense alumina.

(2) Alloying and Third Element Additions to Silicides

Many of the A_5Si_3 refractory metal silicides are isostructural. This is also the case in the ASi_2 family of compounds. Thus fairly broad ranges of solid solution can be expected between members of each group, allowing material properties to be tailored to a certain degree. By alloying WSi_2 with $MoSi_2$, Petrovic and Honnell[18] fabricated SiC whisker based

composites with 50% WSi_2-50% $MoSi_2$ matrix. The alloy composite had a (4 point bend) yield stress of 590 MPa at 1200°C, compared to 410 MPa for an unalloyed $MoSi_2$ matrix SiC whisker composite. The high temperature oxidation resistance of $MoSi_2$ is due to the formation of a surface layer of SiO_2 on heating. On cooling or during low temperature service, this coating may spall off due to thermal expansion mismatch between SiO_2 and the

Table II. Other properties of molybdenum silicides.[15]

Material	Property	Value	Notes
Mo_5Si_3	thermal expansion	4.3 x 10^{-6}/K	300-550 K
Mo_5Si_3	thermal expansion	6.7 x 10^{-6}/K	500-1350 K
$MoSi_2$	thermal expansion	8.25 x 10^{-6}/K	300-1350 K
Mo_3Si	thermal expansion	6.5 x 10^{-6}/K	450-1350 K
$MoSi_2$	E_y	390 GPa	RT, Srinivasan[15]
Mo_5Si_3	E_y	280 GPa	RT, Fleisher[17]
Mo_3Si	E_y	304 GPa	no details
$MoSi_2$	tensile strength	400 MPa	1273 K
		100 MPa	1623 K
$MoSi_2$	compressive	1500 MPa	293 K
	strength	420 MPa	1673 K
All Compounds	micro hardness	12-15 GPa	293 K
$MoSi_2$	K_{IC}	3.6 MPa m½	Hot Press 1600°C

$MoSi_2$ matrix. Fitzer et al.,[19] alloyed $MoSi_2$ with $MoGe_2$ so that a SiO_2-GeO_2 surface oxide layer would form. This oxide layer has a thermal expansion coefficient of 6 x 10^{-6} /K (20-300°C), which compares quite well to the thermal expansion of (all) molybdenum silicides. The germanide addition resulted in a lowered Young's modulus, but did not effect ultimate strength. Best oxidation resistance at 1400°C was obtained with a 10 weight percent $MoGe_2$

addition. In the same work, niobium wire reinforcements were made to the silicide/germanide material. In this case, germanium additions greatly improved the ductility of the wire reinforced composite. The researchers also noted that Mo_5Si_3 and Nb_5Si_3 formed a continuous solid solution at the Nb wire/$MoSi_2$ interface.

Maloy et al.[13] made a 2 weight percent carbon addition to $MoSi_2$ and recorded improved fracture toughness and hardness values. They attributed these gains to the reduction of SiO_2 present in the grain boundaries of $MoSi_2$ and to the presence of Mo_5Si_3C and SiC in the microstructure. Wade and Petrovic[20] identified a $MoSi_2$-Mo_5Si_3 lamellar structure formed on the surface of hot pressed $MoSi_2$. Micrographs show that the lamellae have spacing of about 1 μm, and in contrast to Cherniak et al's observations, no microcracking can be seen. Wade and Petrovic did not comment on mechanical properties of the material with the eutectic layer.

Srinivasan and Schwartz[15] measured the elastic constants for two Mo_5Si_3-$MoSi_2$ alloys and one $MoSi_2$ -WSi_2 alloy by sonic excitation. Their values are presented in Table III. Note that 50 weight percent Mo_5Si_3 is very nearly the Mo_5Si_3/$MoSi_2$ eutectic composition.

(3) Oxidation Resistance of Molybdenum Silicides

There has been widespread interest in the mechanism of oxidation resistance of $MoSi_2$.[21-27] Oxidation behavior varies with extrinsic as well as intrinsic material properties,[28] but it is expected that the same basic oxidation mechanisms are operative for Mo_5Si_3. Although $MoSi_2$ exhibits excellent oxidation resistance at temperatures greater than 800°C in air, it exhibits catastrophic oxidation failure at certain combinations of temperature and oxygen partial pressure. This low temperature catastrophic oxidation is known as pesting. The actual temperature range for pest is a function of extrinsic specimen properties.

It has been reported that dense polycrystalline and single crystal $MoSi_2$ samples are immune to pest oxidation.[24]

Pest in $MoSi_2$ occurs due to continual active oxidation on specimens that lack a continuous passivating SiO_2 surface layer. Below about 800°C, the growth kinetics of the protective SiO_2 layer are slow.[27] The formation of MoO_3, usually at grain and void

Table III. Elastic constants of $MoSi_2$, $MoSi_2$-WSi_2, and $MoSi_2$-Mo_5Si_3 alloys

Material wt% Mo_5Si_3	Ey, GPa	G, GPa	Poisson's Ratio	Density, g/cm^3 :%theoretical
$MoSi_2$	387.5	168.9	0.15	6.02 :96%
$MoSi_2$-27Mo_5Si_3	337.5	137.9	0.22	7.09 :98%
$MoSi_2$-50Mo_5Si_3	320.3	128.4	0.25	7.49 :97%
$MoSi_2$-50WSi_2	401.2	172.1	0.16	7.65: 97%

boundaries produces a 250% volume change.[27] Below 800°C, the large volume expansion accompanying the formation of molybdenum oxides causes internal stresses that lead to microcracking and formation of fresh surface, and the process repeats until molybdenum is consumed and the specimen is reduced to oxide powder. In contrast, above 800°C, MoO_3 volatilizes, leaving a localized area with high silicon activity that forms a protective silicon dioxide scale. The diffusing species in silicon dioxide scale formation on silicides is generally accepted as oxygen,[29] and the scale forms at the silicide/oxide interface.

The oxidation resistance of Mo_5Si_3 has generally been found to be unacceptable for high temperature use in air. It is characterized by a porous scale formation and active oxidation except at very high temperatures.[19] Oxidation data is summarized in Figure 5. Figure 5 shows that at temperatures below 1000°C, passive oxidation occurs only at oxygen

partial pressures lower than 10 Pa. As temperature is increased to 1650°C, a dense, protective oxide layer is formed at atmospheric oxygen pressure. In order to reach this point, however, the material must be subjected to active oxidation while heating in air to 1650°C. Also included in this plot is a line dawn from a model proposed by Bartlett, et al.[27] to explain the lack of oxidative stability of Mo_5Si_3 at low temperatures.

The oxidation model proposed by Bartlett is based on the premise that in order to maintain P_{O_2} at the level thermodynamically dictated by Si/SiO_2 equilibria, the rate of silicon supply to the oxidation interface must be faster than the rate of silicon consumption due to reaction with oxygen. If the silicon consumption rate is greater than the maximum rate of silicon supply, the oxidation interface becomes silicon depleted. Si/SiO_2 equilibria is established at a high oxygen partial pressure at the silicon depleted interface. P_{O_2} may increase to a level where the oxidation of molybdenum is thermodynamically favorable, leading to molybdenum oxidation. At T<750°C molybdenum oxidation may cause pest. At T>750°C molybdenum volatilizes, leading to rupture or formation of a non-passivating, porous scale.

The maximum rate of silicon supply to the interface was assumed by Bartlett to be the same as the rate of Mo_3Si interlayer formation in a $Mo/MoSi_2$ diffusion couple. The rate of silicon consumption was assumed to be the same as for the oxidation of silicon metal. A plot of the relative rates of silicon consumption and supply are shown in Figure 6. The intersection of the three lines for the oxidation of silicon with the line for dissociation of Mo_5Si_3 at points A, B, and C make up the curve shown in Figure 5. It was found that at ambient oxygen pressure the rate of silicon supply was lower than the rate of consumption at temperatures below 1650°C resulting in a silicon depleted interface, consistent with

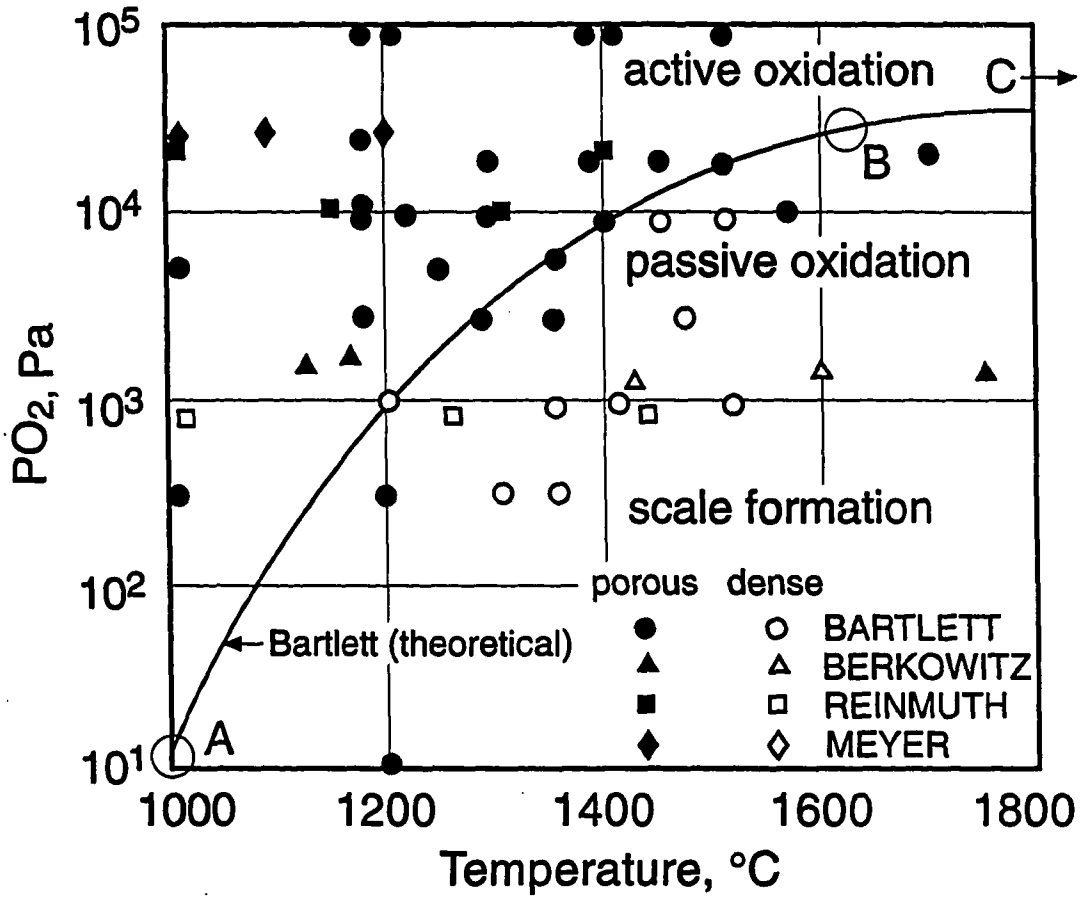

Figure 5. Compilation of oxidation data for Mo_5Si_3. Curve is expected boundary between protective and non-protective scale formation according to Bartlett's model.

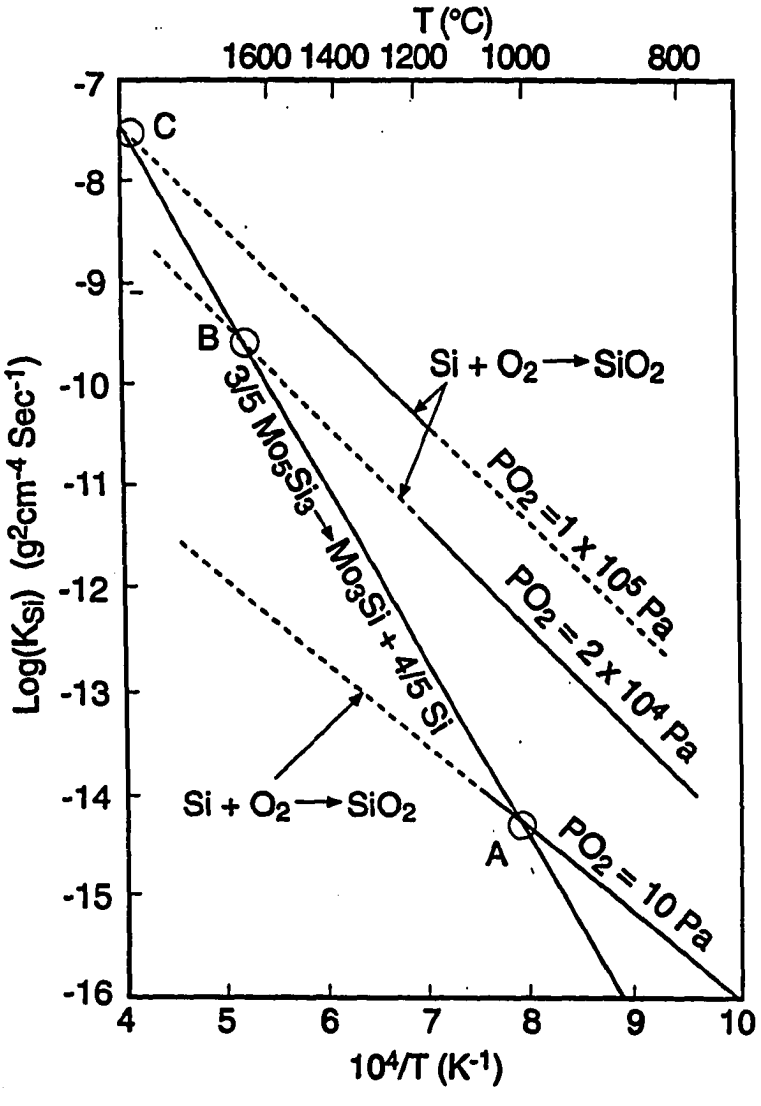

Figure 6. Relationship between dissociation of Mo_5Si_3 to Mo_3Si and silicon and oxidation rate of silicon (after Bartlett[27]).

experimental oxidation data. There was, however, no experimental evidence presented for the formation of an Mo_3Si interlayer during oxidation of Mo_5Si_3. It has been shown[30] that SiO_2 can exist in equilibrium with Mo and Mo_5Si_3 so that formation of an Mo_3Si layer is not thermodynamically necessary. In the case of Mo interlayer formation, the rate of silicon supply would be established by the rate(s) of silicide dissociation followed by diffusion of silicon through a Mo layer.

Berkowitz-Mattuck and Dils[31] studied the oxidation of Mo_5Si_3 by monitoring oxygen consumption during oxidation at temperatures of 1107°-1737°C and oxygen pressures of 1082-1750 Pa (8.5-13.1 Torr). Oxidation times were 80-110 minutes. At 1107° and 1137°C, oxygen consumption was rapid over the duration of the oxidation test, indicating active oxidation, and implying non-protective scale formation. Above 1377°C, specimens exhibited a plateau region of slow oxygen uptake after an initial transient period of rapid oxidation. Total oxygen consumption during an oxidation test decreased as oxidation temperature increased. High temperature passivation was proposed to be due to the temperature dependent lateral flow of SiO_2 to form a continuous layer. The interlayer that formed between the silicide and scale was determined to be a molybdenum rich terminal solid solution alloy, with no evidence for Mo_3Si formation.

Most recently, Anton and Shah[14] reported catastrophic oxidation of arc cast Mo_5Si_3 within 20 cycles to 1149°C. The oxidation product was α-cristobalite. Previous oxidation data for Mo_5Si_3 is consistent with the results of this work.

Mueller et al.[32] found that $(Mo,W)(Si,Ge)_2$ alloy coatings on niobium had better oxidation resistance than $Mo(Si,Ge)_2$ coatings. Both had better oxidation resistance than $MoSi_2$. The increased oxidation resistance is attributed to lower glass formation temperature in germanium containing alloys and lower glass viscosity at high temperatures. The lower viscosity allows the glass to flow and heal cracks that form. No pesting behavior was

observed between 500° and 700°C for the $(Mo,W)(Si,Ge)_2$. The researchers attributed this to a more closely matched coefficient of thermal expansion between the (Ge,Si) oxide glass film and the substrate silicide. Since the expansions are matched on cooling, no cracks form in the coating below the glass transition temperature.

IV. Results of Preliminary Research

Since little background information is available on processing Mo_5Si_3 to dense bodies for properties evaluation, experiments were conducted pertaining to compound synthesis and subsequent material processing procedures. This section also contains information on hardness, bend strength, and the results of preliminary oxidation tests used to screen Mo_5Si_3 based materials for further testing.

(1) Compound Synthesis

Synthesis of intermetallics may be accomplished by perhaps a dozen methods. Of these, arc melting, reactive sintering, and mechanical alloying have been attempted. Arc melting has been determined to be best suited to the requirements of this project.

Arc Melting Arc melting involves placing the reactants on a water cooled copper hearth in inert atmosphere and passing a high electrical current through the reactants to melt and homogenize. The melting is normally repeated three times. The product of the arc melting process is a button of large grain material. The material is often macro and microcracked due to the high thermal stresses involved. Since the melting temperatures of silicon and molybdenum differ by 1200°C, some silicon is often lost by evaporation during arc melting. This shows up as the presence of Mo_3Si in the x-ray diffraction pattern. An

addition of 0.5 weight percent extra silicon moves the arc melted composition back into the Mo_5Si_3 phase field.

Chemical analysis of the impurity elements present (by laser mass spectrometry) in two samples of Mo_5Si_3 are shown in Table IV. The first column in the table is Mo_5Si_3 that was reactively sintered at 1440°C with 8 wt% silicon powder, 49 wt% molybdenum powder, and 43 wt% Mo_5Si_3 powder ground from an arc melt button. These powders were milled in an argon atmosphere glovebox. The starting particle size of the molybdenum powder was 5 μm (mean), the silicon powder had mean size 5.4 μm. The Mo_5Si_3 powder was milled for 1.5 hours. Particle size was not measured, but previous experience shows that mean size will be less than 1 μm. Reported oxygen content of the silicon powder is 0.2-0.7 weight percent, with overall purity of 99%. Reported purity of the molybdenum powder is 99.95%, with no oxygen content given. The second column represents the chemical analysis of a pellet sintered from powder ground from the same batch of arc melt buttons. Starting material for arc melting was silicon chunck of 99.995% reported purity and molybdenum rod of 97.4% purity. Arc melting was done in argon. The arc melt button was ground for 1.5 hours to a mean particle size of 0.27 μm in an argon atmosphere glove box. The fine powder was then pressed into a pellet in air and sintered to 1420°C in argon. The data shows that arc melting produces a material with lower oxygen content when compared to reactive sintering. This is probably due to the fact that the starting materials used in arc melting are large chunks of silicon and molybdenum, which have less surface area than fine powders, and therefore less opportunity for reaction with atmospheric oxygen. The iron content in the arc melted material is higher, however, due to iron impurity in the molybdenum rod used as stock.

Carbon and boron containing compositions were also arc melted. The carbon containing compounds show a loss of carbon, possibly due to combination with the oxides present on the silicon starting material. No oxygen analysis data is available to support this

assumption. The relatively high tungsten content is believed to be due to the tungsten electrode used arc melting. This impurity is not believed to be significant for the purpose of this study.

Mechanical Alloying Mechanical alloying involves subjecting elemental powders to high energy attrition in an impact mill. The process requires upwards of 50 hours milling

Table IV. Laser-MS chemical analysis of arc melted Mo_5Si_3.
Analysis given is weight ppm.

Impurity	Reactively sintered	Sintered from arc melt Mo_5Si_3 powder
Oxygen	1100	180
Aluminum	690	360
Iron	480	1000
Titanium	410	55
Nickel	380	530
Chromium	240	300
Tungsten	530	580
Vanadium	68	73
Carbon	9	29
Calcium	31	57

time[33] for $MoSi_2$ formation. The milling process generates a substantial amount of heat, which can result in rapid attrition of the container walls and a significant amount of impurity can be introduced into the batch. Liquid nitrogen is often used to cool the mill vial and contents, but this can lead to nitride formation. For this reason a molybdenum lined mill vial was used for milling of powders. The chief advantage of mechanical alloying is that

nanocrystalline powders are produced which can lead to enhanced sintering behavior. Rather than relying on mechanical alloying alone, a combination of mechanical alloying and reactive sintering were used to produce compounded powders. Elemental molybdenum and silicon powders were combined and milled for a 4 hours. Only a small amount of compound formation occurred as a result of this milling. The powders were then compacted and sintered at 1440°C to compound them. After sintering, the compacts were reground. X-ray diffraction patterns show that phase pure Mo_5Si_3 is formed after this step. Although this process produced x-ray pure material, it is a labor intensive, low volume process. There are several opportunities for contamination during processing. Because of the large volumes of relatively pure material needed for mechanical properties testing, arc melting was chosen as the preferred method for obtaining Mo_5Si_3 based materials used in this study.

(2) Densification

Four methods of densification were attempted. These were hot isostatic pressing (HIPping) of green bodies encapsulated in glass, reactive HIPping, reactive liquid phase sintering, and solid state sintering.

Glass encapsulated HIPping For glass encapsulated HIPping powder compacts were first spray coated with a hexagonal boron nitride barrier layer and imbedded in 16 mesh pyrex glass powder. The boron nitride layer was applied as a spray coating using ethanol as a carrier. The glass was melted in the HIP at T>1250°C, and then 30 ksi pressure was applied for 4-10 hours at 1440°C. The glass did provide for pressure transmission to the sample, and resulted in some specimens with 90+% density. It was quite difficult to remove specimens intact from the 7740 Pyrex™ glass slug after HIPping. For this reason, HIPping in sealed tantalum cans was also investigated.

Reactive HIPping Reactive HIPping of elemental molybdenum powders in tantalum cans was investigated as a trial case to determine whether the canning system was adequate. Elemental powders were used because they are much less expensive and more readily available than Mo_5Si_3 powder. The elemental powders used were -325 mesh as received from the supplier. The HIP containers were made from 0.030" thick 1" diameter tantulum tubing. Tantalum end caps were electron beam welded on in vacuo over molybdenum foil disks. The density of the billet after HIPping at 35 ksi and 1420°C was 72.5% of full density, which is a considerable improvement over reactively sintered bodies, but certainly not good enough for materials property testing. The heavy walled (0.030") can was used in two instances, and cracked once. Thinner walled cans may be more resistant to cracking and more effective at transmitting force to the sample. Another alternative may be the use of more ductile niobium cans.

Liquid phase sintering In order to liquid phase sinter with silicon, but stay within the Mo_5Si_3 phase field, both silicon and molybdenum elemental powders were added to Mo_5Si_3 powder. Submicron Mo_5Si_3 and molybdenum with starting mean particle size of 7.5 μm were milled for 1 hour under argon. Silicon with mean size 5.4 μm was added, and the mixture was milled for an additional 10 minutes to mix. The mixed powders were compacted at 15 ksi and sintered at 1400°C, 1420°C, and 1440°C under argon. The results of this experiment are shown in Figure 7. As can be seen, at higher silicon and molybdenum compositions, less densification was seen. The addition of a considerable amount of molybdenum was required to offset the silicon added to liquid phase sinter. For example, in the case of the 24 vol% silicon samples, the final compact contained 43 wt% molybdenum powder. Molybdenum powder does not attain high density when sintered at 1400-1440°C, and probably acted to impede densification of the compacts. A better approach may be to start with precompounded powders of Mo_3Si and add silicon to liquid phase sinter,

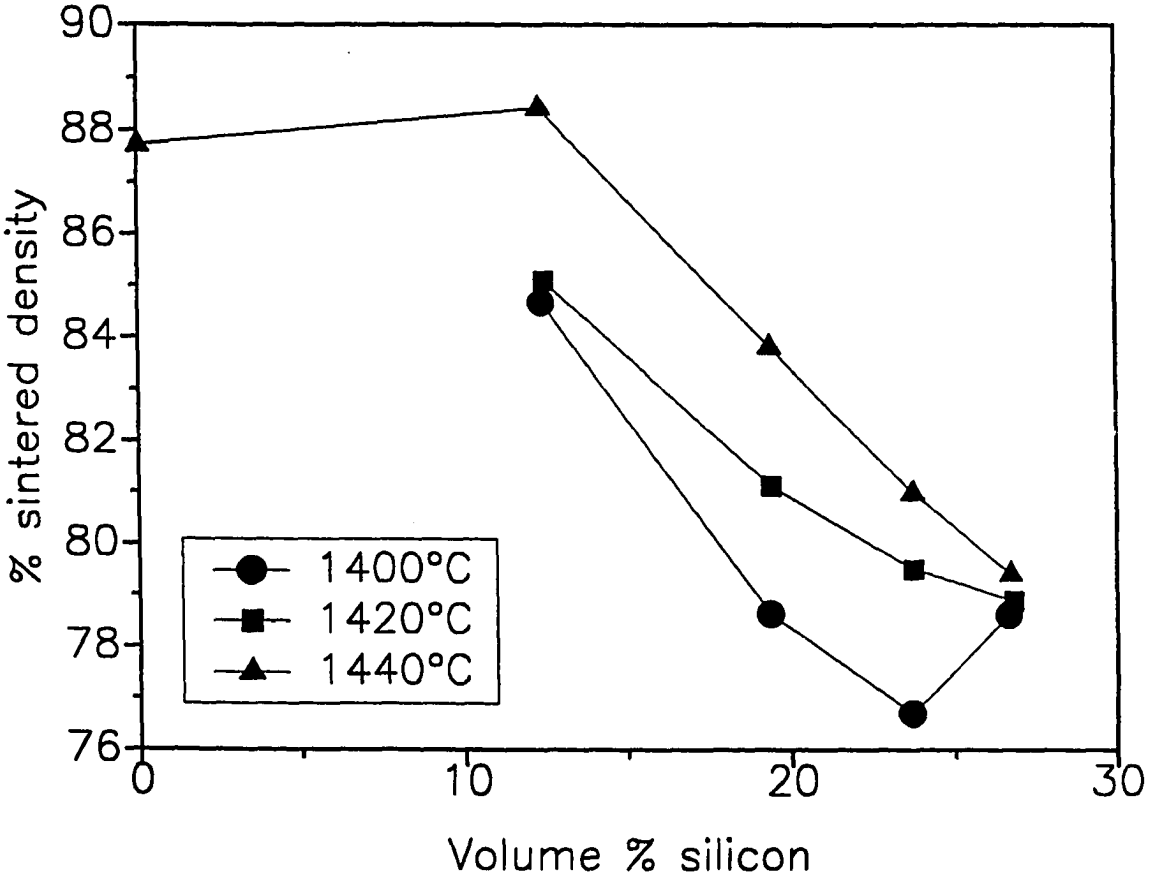

Figure 7. Density results for reactively sintering Mo_5Si_3 with Mo+Si powders.

eliminating molybdenum from the powder compact.

Solid state sintering Significant densification was achieved by solid state sintering. Sintered density was very dependent on starting particle size, as shown in Figure 8. In order to attain high density at a temperatures as low as possible, powder particle size was reduced by impact (SPEX®) milling.

Particle size data was obtained by using a centrifugal Stoke's law particle size analyzer. Powders were cold pressed at 15 ksi into pellets, then sintered for 30 minutes at 1440°C under argon. Each point is the density of two pellets measured simultaneously in a helium pyncnometer. Because it was difficult to reproduce the ultrafine particle size required to sinter to high density at 1440°C, the sintering temperature was increased to 1800°C. The procedure adopted for densification processing is as follows. Arc melt material was ground for six 30 minute cycles in a tungsten carbide or molybdenum lined impact mill vial. One weight percent of methyl cellulose was added to prevent powder agglomeration that otherwise occured during the milling process. Milled powders were sieved to -635 mesh by brushing over a screen with an acid brush for 3 minutes. The use of an ultrasonic sifter increased the amount of -635 mesh powder passing through the screen. This also had the affect of including a large fraction of powder near the nominal screen opening size of 25 μm, increasing the mean particle size significantly, and lowering sintered density 5-8%. After sieving, powder was dry pressed into green bodies. The methyl cellulose added during milling was burned out by heating at 5°C/min. to 600°C in a tube furnace under argon flow. Final sintering occured in a tungsten mesh furnace at 1800°C under high purity argon flow. Ramp rates for this procedure were 20°C/min on both heating and cooling. (X-ray diffraction results on creep specimens prior to creep indicate that the fairly rapid cooling rate may introduce residual stresses into the sintered body, as evidenced by line broadening.) Sintered density of 96% for Mo_5Si_3 and 97.5% for Mo_5Si_3/B were attained using this procedure. The

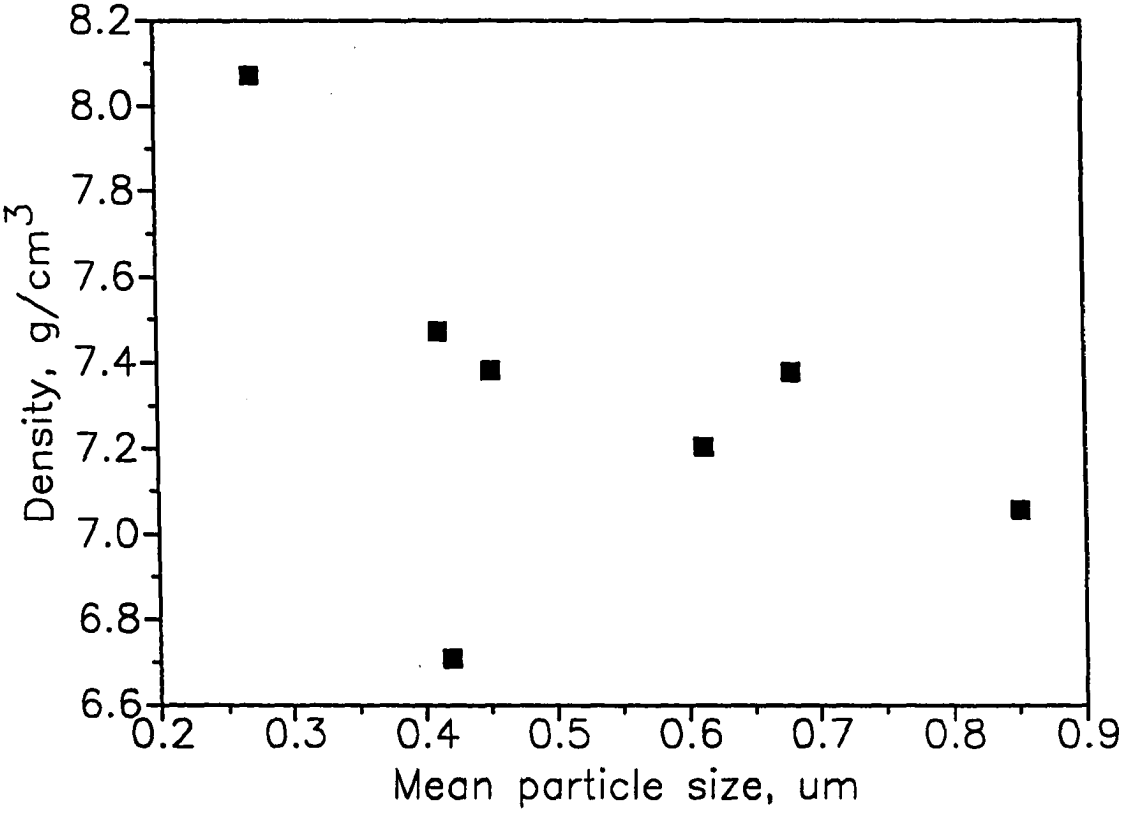

Figure 8. Density results for solid state sintering of Mo_5Si_3 powder at 1440°C. Theoretical density is 8.21 g/cm^3.

three phase microstructure in the case of boron modified Mo_5Si_3 acted to inhibit grain growth. This phenomenon is common in duplex microstructures.[34]

(3) Phase Analysis of $Mo_5Si_3B_x$ and $Mo_5Si_3C_x$

Qualitative phase analysis of materials compounded by arc melting and annealed is given in Table V. Analysis was made by x-ray diffraction and least squares fitting of peaks. Indexing of diffraction patterns of arc melted Mo_5Si_3 and Mo_5Si_3C confirms results by other

Table V. Qualitiative x-ray phase analysis of some $Mo_5Si_3(B,C)_x$ materials produced by arc melting.

Composition	X-ray phase analysis
$Mo_{2.6}Si_3$	$Mo_5Si_3/MoSi_2$ eutectic
$Mo_{4.93}Si_3$	T-Mo_5Si_3
Mo_5Si_3	T-Mo_5Si_3 + trace Mo_3Si
$Mo_5Si_3C_{0.1}$	H-Mo_5Si_3 + T-Mo_5Si_3
$Mo_5Si_3C_{0.5}$	H-Mo_5Si_3 + T-Mo_5Si_3
Mo_5Si_3C	H-Mo_5Si_3
$Mo_5Si_3C_{1.5}$	unknown
$Mo_5Si_3B_{0.1}$	T-Mo_5Si_3 + MoB (tetragonal)
$Mo_5Si_3B_{0.5}$	T-Mo_5Si_3 + MoB (tetragonal)
Mo_5Si_3B	T-Mo_5Si_3 + MoB (tetragonal)
$Mo_5Si_3B_{0.5}C_{0.5}$	unknown

researchers. There is very limited solid solubility of the light elements in the Mo_5Si_3-B and Mo_5Si_3-C systems. Upon addition of small amounts of boron or carbon, a second phase forms. This is in contrast to some other A_5Si_3 materials (Ti_5Si_3) that form in the hexagonal Mn_5Si_3 structure in the 'pure' state. The Mn_5Si_3 structure has large voids at the corners of

the unit cell that are easily filled with interstitial atoms. No such interstitial sites occur in the tetragonal W_5Si_3 structure.

(4) Mechanical Properties of Mo_5Si_3

Limited strength and indentation testing was carried out as a screening tool for the selection of promising materials for further study of creep and oxidation behavior.

Indentation Testing Indentation test results are summarized in Table VI and Figure 9. The values of K_{IC} presented here are quite good for brittle materials. This data must be interpreted with caution since assumptions made about crack geometery may not be true. In brittle materials, radial cracking around the hardness indentation is usually observed, and gives some measure of fracture toughness if certain assumptions about crack geometry and superposition of elastic and plastic strain are made. Lawn[35], Evans[37], Chiang[37], and Anstis[38], have all treated this problem. The method of Anstis involves using an empirical calibration constant to take into consideration geometrical factors that are difficult to calculate. The equation is as follows:

$$(2) \qquad K_{IC} = P\xi \sqrt{\frac{E}{HC_o^3}}$$

Here P is the applied indentation load, E is the Young's Modulus of the sample, H is the hardness, C_O is crack ½ length, and ξ is a calibration constant found by Anstis to be 0.016. An accuracy of 30 to 40% is predicted when compared to conventional K_{IC} measurements so that the method is more of a tool for comparison between similar materials than an absolute measure of fracture toughness. Fracture toughness data from the indentation cracks (method of Anstis) has been obtained for some materials. The fracture toughness values are similar to those quoted for other brittle ceramics and intermetallics. The partially lamellar eutectic

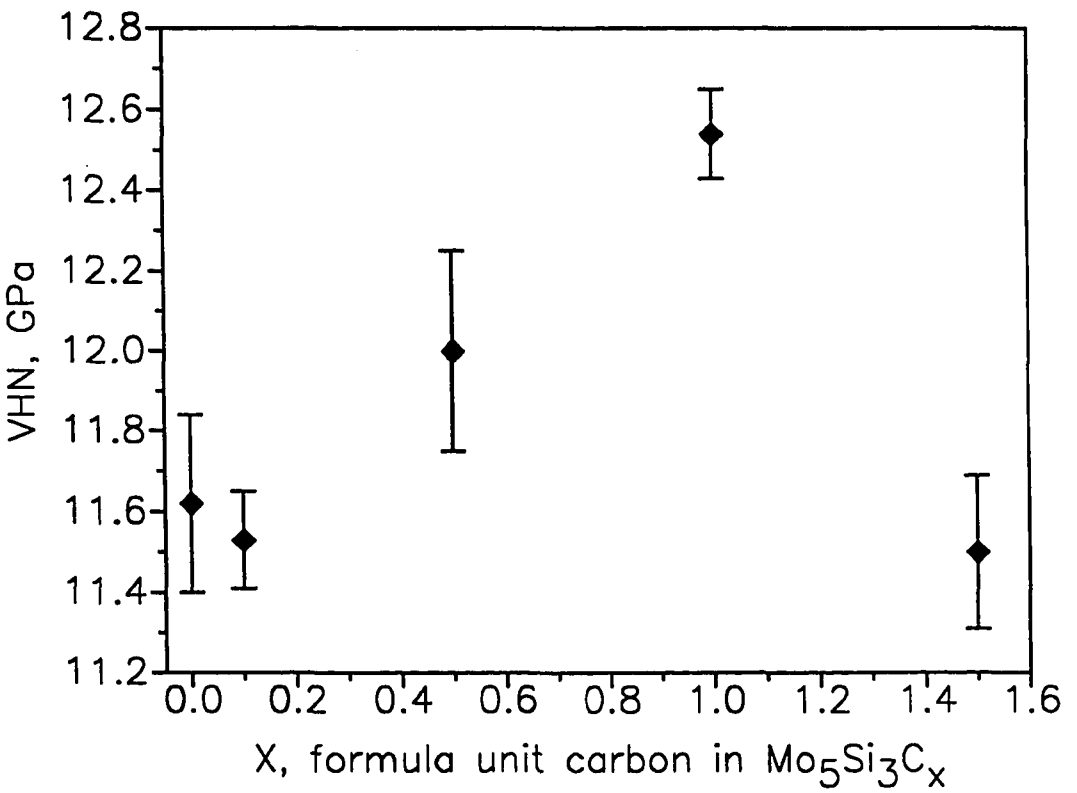

Figure 9. Hardness of $Mo_5Si_3C_x$. Error bars represent 99% confidence intervals

Table VI. Micro-indentation data for $Mo_5Si_3(B,C)_x$, 9.8 N load. Range indicates 99% confidence interval.

Composition[1]	Hardness[2], GPa	K_{IC}[3]	Density[4]
Mo_5Si_3	12.04±0.26	2.9±0.20	97%
$Mo_5Si_3C_{0.1}$	12.03±0.34	4.6±0.57	91%
$Mo_5Si_3C_{0.5}$	12.23±0.28	4.7±0.38	91%
Mo_5Si_3C	12.84±0.26	4.4±0.20	92%
$Mo_5Si_3C_{1.5}$	11.71±0.37	4.1±0.33	unknown
Mo_5Si_3/B[5]	11.8±0.30	3.4±0.40	84%
eutectic	11.39±0.15	4.9±0.40	91%

[1]Nominal compositions. [2]Range is 99% confidence interval. Load is 1000 [3]K_{IC} based on literature value of moduli: 260 GPa for $Mo_5Si_3Z_x$ and 320 GPa for eutectic material. [4]Theoretical density of 8.24 g/cm^3 for $Mo_5Si_3Z_x$ and 7.72 g/cm^3 for eutectic. [5]500g load data

microstructure of the $Mo_5Si_3/MoSi_2$ eutectic material may exhibit a slight increase in fracture toughness over Mo_5Si_3. This is not completely clear however, due to the difference in porosity between the two materials and the uncertainty in Young's modulus.

The addition of carbon to Mo_5Si_3 does appear to increase hardness, as seen in Figure 9. This may correspond to an increase in the amount of carbon stabilized Mn_5Si_3 structure present. At one formula unit of carbon (Mo_5Si_3C) the material is 100% hexagonal Mn_5Si_3 phase, and the highest hardness values are obtained. As the amount of carbon increases past one formula unit, hardness values again decrease. X-ray diffraction shows that the C=1.5 composition is neither the hexagonally stabilized Mn_5Si_3 structure or the tetragonal W_5Si_3

structure but some as yet undetermined structure. Pyncnometric density values are also plotted given in Table VI, since density has a large bearing on hardness.

Four point bend tests Four point bend tests were completed on specimens that were reactively HIPped in a tantalum can, as discussed above. The specimens were electro-discharge machined (EDM) from a billet, and polished in progressively finer steps down to 0.3μm alumina. Specimen density was only 72.5% from the reactive HIPping process. Specimens were loaded in an articulating 4-point bend fixture to reduce the effects of friction and misalignment, and loaded at a rate of 1 mm/min crosshead deflection rate. All specimens broke between the inner load points of the 4-point bend fixture. Average strength of the bars was 92.4 MPa, with 95% confidence interval limits of 80-105 MPa. The specimens have only about one fourth the strength of monolithic $MoSi_2$. Surface defects due to EDM flaws (that were not completely removed on polishing), and low specimen density contributed to low strength. Note, however, that even this value is a large improvement over the 12 MPa tensile strength reported by Anton and Shah.[14]

Elastic modulus A determination of the elastic modulus of a specimen cut from the same billet was made at temperatures up to 1200°C using sonic resonance. The room temperature elastic modulus was 116 GPa, a low value, but to be expected from a porous specimen. A plot of the percent of room temperature elastic modulus retained as a function of temperature is shown in Figure 12. Also plotted is the same data for alumina of density from 94% to 99%, and a single crystal superalloy oriented in the <111> direction. It can be seen that the behavior of Mo_5Si_3 is similar to that of alumina, in that a greater fraction of the modulus is retained at 1200°C than for the superalloy. Note that both the 94% dense alumina

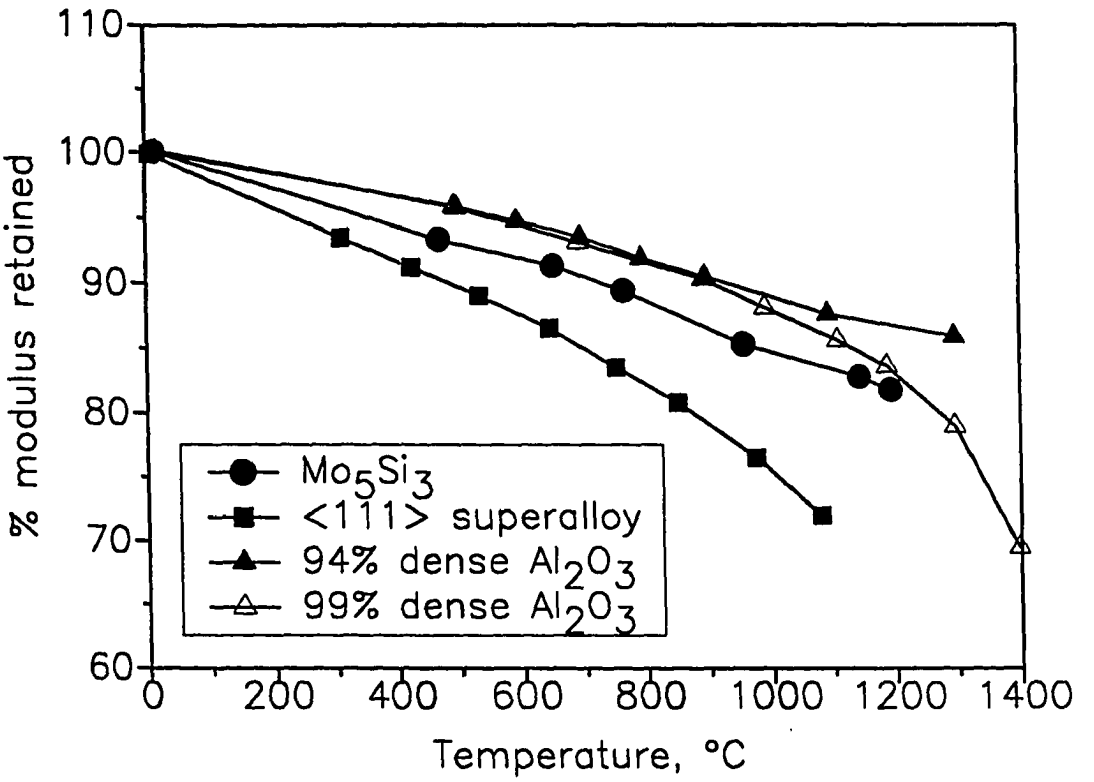

Figure 10. Elastic modulus of Mo_5Si_3 and other materials as a function of temperature.

and Mo_5Si_3 exhibit a tail near 1200°C. This is probably due to further densification, or healing of microcracks in the specimens. Retention of specific stiffness (modulus/density) at high temperatures is an important consideration for materials that are to be used in rotating assemblies.[39]

(5) Oxidation Resistance

As mentioned above, the oxidation resistance of silicides stems from the growth of a non porous SiO_2 surface layer. If the mass change of the specimen decreases parabolically with time, then oxidation is generally regarded as diffusion controlled.[40] The relevant oxidation model is summarized by the equation: $\Delta W = k\sqrt{t}$, where ΔW is the mass gain, and k is a rate constant. The diffusing species in silica layer formation is oxygen, so that the scale grows at the silicide/oxide interface rather than the air/oxide interface. The oxide species that may form at the silicide/oxide interface depend on the partial pressure of oxygen at the interface and the relative free energies of formation of the elemental species present at the interface. The types of elemental species present at the interface depend on the initial composition of the body and on the rate of diffusion of the elements to the interface.

Oxidation kinetics of a specimen that are linear with time suggest that oxidation is reaction rate controlled or controlled by boundary layer diffusion. This indicates that a coherent oxide scale is not forming, and that oxygen supply to the interface is not diffusion limited. A change in oxidation rate with oxygen flow indicates that oxidation is not diffusion limited. Two primary reasons for formation of a non coherent scale are scale cracking and formation of a porous oxide. Scale cracking may occur due to thermal stresses or mechanical microstresses associated with the volume change on formation of oxidation products. Porous oxide scales may form due to inhomogeneous distribution of the oxide forming component in a body or insufficient chemical activity of the oxide forming component. Volatilization of one

of the oxides or alloy components may cause bubble to form and burst in the scale, forming holes. The model equation for linear oxidation is simply $\Delta W = kt$.

Two types of oxidation tests were carried out to determine the suitability of materials for service in air. First, cyclic oxidation tests in static air were conducted as a means of choosing compositions for further study. Compositions that showed promise were selected for further kinetic study using a continuous recording balance. The results from the two different test conditions are quite different. These differences emphasize the need for a material that maintains oxidative stability under a range of atmospheric conditions.

Cyclic oxidation Experimental results of the cyclic oxidation of Mo_5Si_3, $Mo_5Si_3/MoSi_2$, Mo_5Si_3B, and $Mo_5Si_3C_x$ are presented in Figures 11 and 12. Irregularly shaped HIPped specimens of varying porosity (see Table VI for density data) were subjected to this simple test to determine which compositions merit further study as oxidation resistant materials. Specimens were heated in alumina crucibles at 20°C/min to 1000°C, held for 10 hours at 1000°C, furnace cooled to 200°C, then reheated. A $MoSi_2$ element furnace was used to heat the specimens in ambient air. Mass data was taken at intervals during this process. It can be seen from Figures 11 and 12 that Mo_5Si_3 and $Mo_5Si_3C_x$ have quite poor oxidation resistance in comparison to $Mo_5Si_3/MoSi_2$ and Mo_5Si_3B. These tests also also indicate that these materials will not fail due to oxidative instability enhanced by thermal cycling.

Thermogravimetric study of oxidation kinetics On the basis of the cyclic oxidation results, 4 compositions were chosen for study of the oxidation kinetics at 800°C, 1000°C, and 1200°C. HIPped pellets of compositions Mo_5Si_3, $Mo_5Si_3C_{0.1}$, Mo_5Si_3B, and $Mo_5Si_3/MoSi_2$ (eutectic) were suspended in a vertical tube thermo gravimetric analyzer at high temperature under flowing air. The air used was compressed ambient 'breathing air' which contains 200-600 ppm water vapor. Use of this oxidant but is much more representative of 'real world'

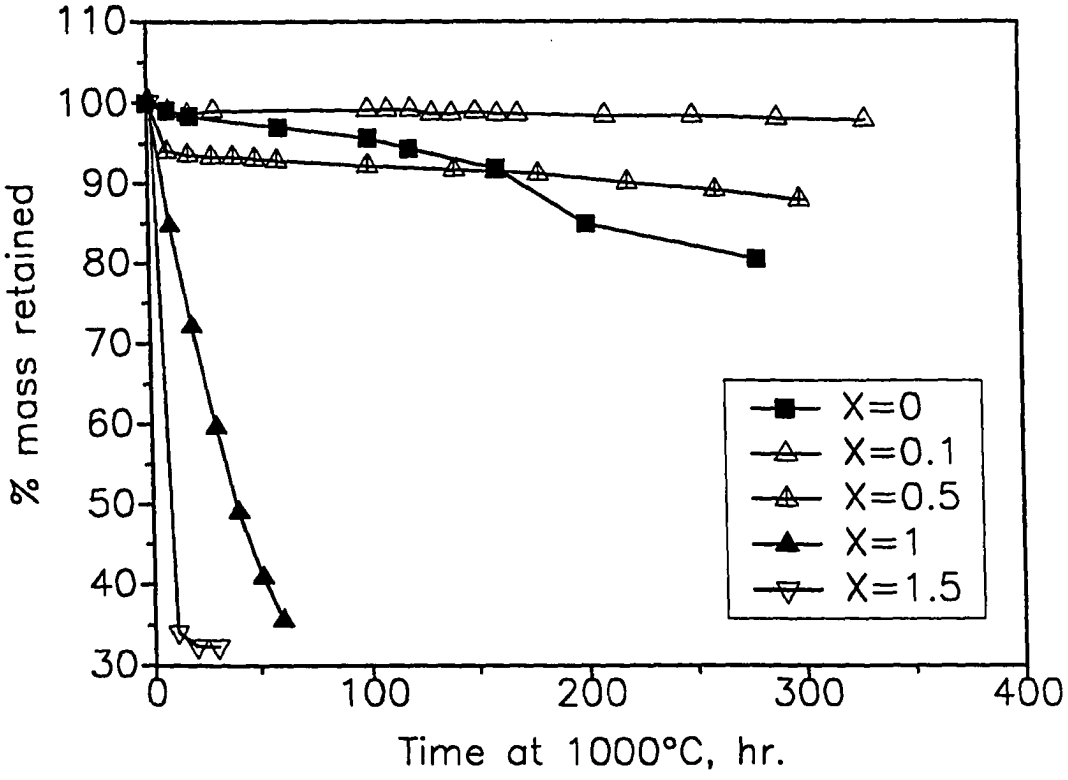

Figure 11. Cyclic oxidation behavior of Mo_5Si_3 and $Mo_5Si_3C_x$.

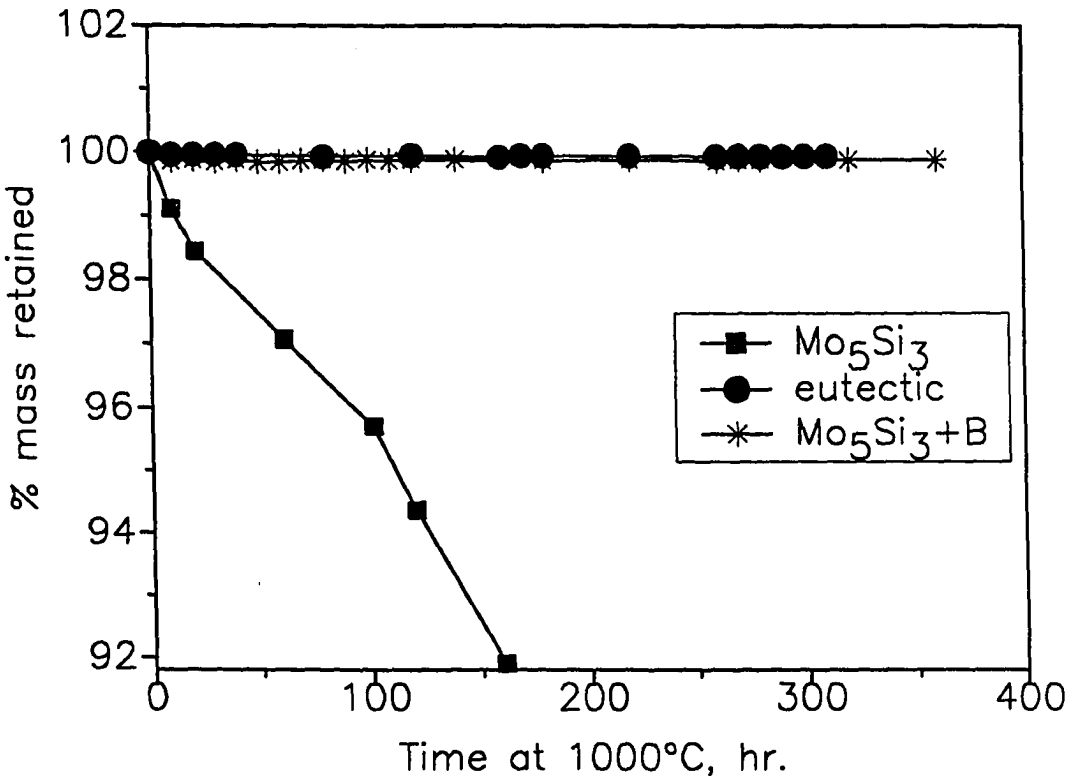

Figure 12. Cyclic oxidation of Mo_5Si_3, Mo_5Si_3B, and $Mo_5Si_3/MoSi_2$ eutectic compositions.

conditions but presents some problems in interpretation of oxidation rate due to the possibility of variable moisture content. Mass change was monitored as a function of time at temperature for periods of 50-300+ hrs. Kinetic data is summarized in Table VII. A plot of the 1000°C isothermal oxidation of the 4 compositions along with Mo_5Si_3 doped at higher carbon levels is shown in Figure 13, which includes the initial ramping up to temperature at 20°C/min (the first 50 minutes of plot).

The oxidation of $Mo_5Si_3C_{0.1}$ in flowing air at 1000°C was catastrophic. A large coherent section of scale came loose when the specimen was removed from the TGA, and there was visible evidence of molybdenum oxide formation beneath the scale. This indicates that $Mo_5Si_3C_x$ compositions are prone to pest under conditions in which a high temperature structural material would be most useful. Mo_5Si_3 exhibited linear oxidation kinetics, with oxidation rate somewhat slower than that of $Mo_5Si_3C_{0.1}$. SEM observation of surface of the oxide scale shows that it is cracked, porous, and not acting as a diffusion barrier to oxygen. A more complete analysis of the oxidation behavior of Mo_5Si_3 is given in Chapter 2. The eutectic composition (15.5 wt% Si) showed slow linear oxidation kinetics and continual mass loss. The steady state mass loss after 200 hours of oxidation is approximately the same as the steady state mass gain of Mo_5Si_3B. While showing a thirty fold improvement in oxidation rate over Mo_5Si_3, the scale still exhibits small cracks and some porosity.

The addition of less than 2 weight percent boron to form the nominal composition Mo_5Si_3B gives a dramatic increase in oxidation resistance. The specimen initially shows a mass loss on heating, again presumably due to MoO_3 volatilization, followed by a slow weight gain due to the formation of a protective oxide scale. Note that the specimen exhibits a mass gain on oxidation as opposed to a weight loss in the case of pure Mo_5Si_3. The mass gain is parabolic, indicating classic formation of a passive protective scale.

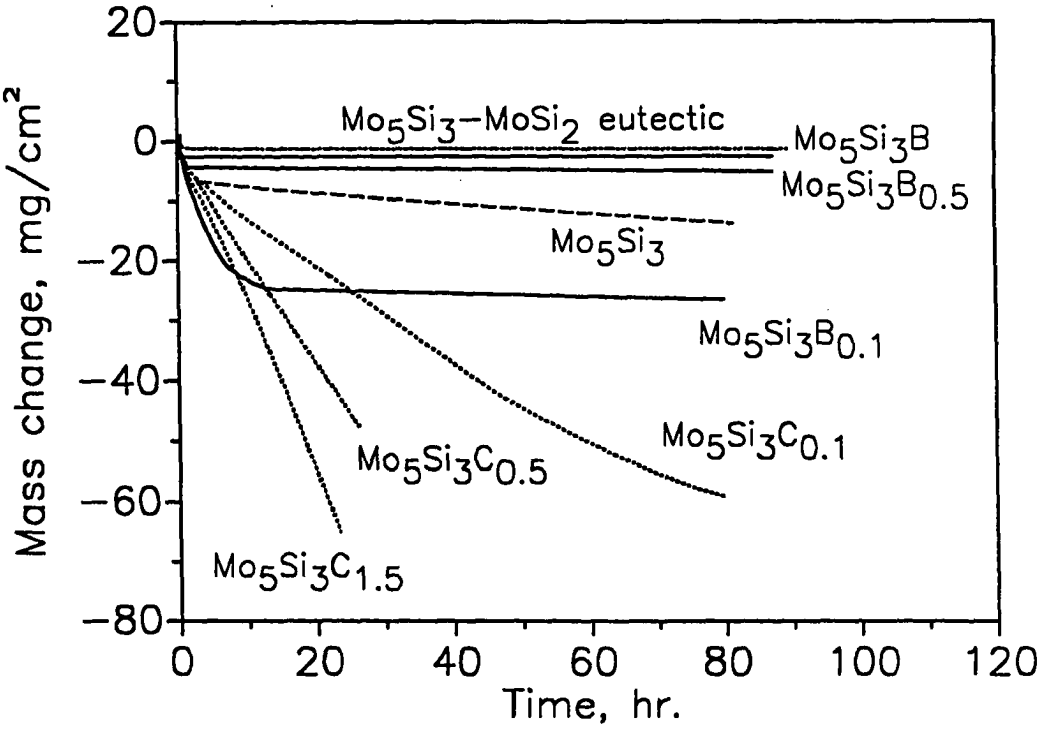

Figure 13. Isothermal oxidation of Mo_5Si_3 based materials at 1000°C.

Table VII. Kinetic data for the oxidation of $Mo_5Si_3(B,C)_x$ compositions at 800°C-1200°C

Oxidation temp., °C	Kinetic model	Steady state [1] rate constant	Correlation coeff. (R^2)	Run time, hr.
Mo_5Si_3				
800	no steady state	----	----	15
1000	linear	$-3.2x10^{-2}$	0.997	80
1200	linear	$-1.3x10^{+3}$	0.997	3
$Mo_5Si_3C_{0.1}$				
800	linear	$-1.1x10^{-2}$	0.996	50
1000	linear	$-6.9x10^{-1}$	0.999	40
1200	no steady state	----	-----	1
Eutectic				
800	linear	$-1.8x10^{-3}$	0.794	100
1000	linear	$-1.0x10^{-3}$	0.945	240
1200	linear	$-9.2x10^{-5}$	0.492	200
Mo_5Si_3B				
800	linear	$-1.9x10^{-3}$	0.927	100
1000	parabolic	$+4.0x10^{-4}$	0.968	200
1200	parabolic	$+3.1x10^{-4}$	0.987	200

[1]Rate constant in units of $mg/(cm^2\ hr)$ for linear model and $mg^2/(cm^4\ hr^{0.5})$ for parabolic model. Note that these rate constants may differ slightly from those in Chapter 2 due to batch to batch variations in arc melt material.

Based on the results of oxidation data presented above, boron doped Mo_5Si_3 was chosen as the primary material for further investigation. More complete oxidation tests and creep tests were carried out on this material. Results of these investigations are given in the manuscripts contained in this thesis.

CHAPTER 2:

OXIDATION BEHAVIOR OF BORON MODIFIED Mo_5Si_3 AT 800°-1300°C

A manuscript submitted to the *Journal of the American Ceramic Society*

Mitchell K. Meyer and Mufit Akinc

Ames Laboratory and Department of Materials Science and Engineering

Abstract

Mo_5Si_3 shows promise as a high temperature creep resistant material. The high temperature oxidation resistance of Mo_5Si_3 has been found to be poor, however, limiting its use in oxidizing atmospheres. Undoped Mo_5Si_3 exhibits mass loss in the temperature range 800°-1200°C due to volatilization of molybdenum oxide, indicating that the silica scale does not provide a passivating layer. The addition of boron results in protective scale formation and parabolic oxidation kinetics in the temperature range of 1050°-1300°C. The oxidation rate of Mo_5Si_3 was decreased by 5 orders of magnitude at 1200°C by doping with less than two weight percent boron. Boron doping eliminates catastrophic 'pest' oxidation at 800°C. The mechanism for improved oxidation resistance of boron doped Mo_5Si_3 is due to scale modification by boron.

I. Introduction

For structural applications in harsh environments, a material should have adequate strength, creep resistance, and oxidation resistance. Intermetallic materials have received considerable attention for use as high temperature structural materials. Silicides may be especially well suited for such applications due to the potential for good oxidation resistance at high temperatures. Mechanical properties[1,2,3,4,5,6,7] and oxidation resistance[8,9,10,11] of molybdenum disilicide ($MoSi_2$) have been investigated over the last several decades, with increasing activity in the past several years.[12,13] Although $MoSi_2$ has excellent oxidation resistance at temperatures in excess of 1600°C in air, it has a high creep rate[5,14] above 1200°C, making it unsuitable as a high temperature load bearing material. Pentamolybdenum trisilicide (Mo_5Si_3), on the other hand, has a more complex unit cell[15,16] that may lead to better creep resistance. The slip systems in this unit cell have not been studied, but limited experimental data supports this assumption. The creep rate and some mechanical properties of arc cast Mo_5Si_3 were recently measured by Anton and Shah[17]. The compressive creep rate was measured as 4×10^{-8} sec^{-1} at 1200°C and 69 MPa. For comparison, the creep rate of $MoSi_2$ in the same paper was reported as 2.1×10^{-7} sec^{-1}, nearly an order of magnitude higher.

The oxidation resistance of Mo_5Si_3 has generally been found to be unacceptable for high temperature use in air. It is characterized by a porous scale formation and active oxidation below about 1650°C, with a transition to protective scale formation and passive oxidation at higher temperatures.[18] Bartlett, et al.[19] plotted regions of active and passive oxidation of Mo_5Si_3 as a function of oxygen partial pressure (P_{O_2}) and temperature based on experimental data. Experimental data was compared to a model based on the net rate of silicon depletion at the oxidation interface. The model is based on the premise that in

order to maintain P_{O_2} at the level thermodynamically dictated by Si/SiO_2 equilibria, the rate of silicon supply to the oxidation interface must be faster than the rate of silicon consumption due to reaction with oxygen. Conversely, if the silicon consumption rate is greater than the maximum rate of silicon supply, the oxidation interface becomes silicon depleted. Consequently, Si/SiO_2 equilibria is not established and oxygen partial pressure at the interface increases. An increase in P_{O_2} may lead to molybdenum oxidation and volatilization, causing the scale to rupture and become non-passivating.

The maximum rate of silicon supply to the interface was assumed to be the same as the rate of Mo_3Si interlayer formation in a $Mo/MoSi_2$ diffusion couple. The rate of silicon consumption was assumed to be the same as for the oxidation of silicon metal. It was found that at ambient oxygen pressure the rate of silicon supply was lower than the rate of consumption at temperatures below 1650°C resulting in a silicon depleted interface, consistent with experimental oxidation data. There was, however, no experimental evidence presented for the formation of an Mo_3Si interlayer during oxidation of Mo_5Si_3. It has been shown[20] that SiO_2 can exist in equilibrium with Mo and Mo_5Si_3 so that formation of an Mo_3Si layer is not thermodynamically necessary. In the case of Mo interlayer formation, the rate of silicon supply would be established by the rate(s) of silicide dissociation followed by diffusion of silicon through a Mo layer.

Berkowitz-Mattuck and Dils[21] studied the oxidation of Mo_5Si_3 by monitoring oxygen consumption during oxidation at temperatures of 1107°-1737°C and oxygen pressures of 1082-1750 Pa (8.5-13.1 Torr). Oxidation times were 80-110 minutes. At 1107° and 1137°C, oxygen consumption was rapid over the duration of the oxidation test, indicating active oxidation and implying non-protective scale formation. Above 1377°C, specimens exhibited a plateau region of slow oxygen uptake after an initial transient period of rapid oxidation. Total oxygen consumption during an oxidation test decreased as

oxidation temperature increased. High temperature passivation was proposed to be due to the temperature dependent lateral flow of SiO_2 to form a continuous layer. The interlayer that formed between the silicide and scale was determined to be a molybdenum rich terminal solid solution alloy, with no evidence for Mo_3Si formation.

Anton and Shah[17] most recently reported data from cyclic oxidation tests. Catastrophic oxidation of arc cast Mo_5Si_3 occurred within 20 one hour cycles to 1149°C. The oxidation product was primarily α-cristobalite.

Since Mo_5Si_3 exhibits high creep resistance, it is desirable to improve the oxidation resistance while retaining high resistance to creep. At temperatures below 1650°C, oxidation is catastrophic due to the absence of a passivating layer. At higher temperatures, a passivating layer does form due to flow of SiO_2 or enhanced kinetics of silicon supply to the oxidation interface. The primary objective of this study was to improve oxidation resistance of Mo_5Si_3 by altering the composition of the scale. After establishing baseline oxidation resistance, Mo_5Si_3 was doped with boron to modify scale formation and improve oxidation resistance. The mechanism for improved oxidation resistance due to boron addition was studied.

II. Experimental Procedure

(1) Sample Preparation

Mo_5Si_3 and boron doped Mo_5Si_3 were synthesized by arc melting of the elements in a non-consumable tungsten arc melt furnace under argon atmosphere. The molybdenum source was commercial rod stock (Mi-Tech Metals, Indianapolis, IN) of 98% purity, silicon was in the form of 3-20 mm pieces (Alpha Chemicals, Danvers, MA) of purity 99.995%, and boron was 2-3 mm size material of 99.5% purity (AESAR, Ward Hill, MA). Addition of 1.87 weight percent boron produced a three phase mixture of

Mo_5Si_3, MoB, and $MoSi_2$, with the nominal stoichiometry of Mo_5Si_3B. This material will be subsequently referred to as Mo5Si3/B. Impurity analysis was performed using laser ablation mass spectroscopy (laser-MS). The ten most prevalent impurities in a sintered body made from an arc melted powder ground under an argon atmosphere are given in Table I. Tungsten contamination is most likely due to the tungsten electrode used in the arc melting process, while aluminum and transition metal impurities are likely due to impurities in the molybdenum stock.

Table I. Laser-MS chemical analysis of sintered Mo_5Si_3.

Impurity	Concentration, weight ppm
Oxygen	180
Aluminum	360
Iron	1000
Titanium	55
Nickel	530
Chromium	300
Tungsten	580
Vanadium	73
Carbon	29
Calcium	57

Arc melt buttons were ground to submicron size powders in an impact mill (Model 2000 Mixer/Mill, SPEX Industries, Edison, NJ) contained in an argon filled glovebox. After milling, powders were sieved through -400 mesh (<38 μm). Mo5Si3/B was dry pressed into 75 x 8.5 x 8.5 mm bars at 46 MPa. The bars were spray coated with

hexagonal boron nitride, then placed in a molybdenum lined graphite crucible and encapsulated in borosilicate glass (Corning 7740, Corning Glassworks, Corning NY) at 900°C under argon. The bars were then HIPed at 1440°C and 210 MPa for 4 hours. After HIPing, the bars were removed from the encapsulant glass and sectioned into oxidation coupons approximately 17 x 6.5 x 1 mm in size. The resulting coupons had a density approximately 92.5% of theoretical, measured using a helium gas pycnometer (Model 1305, Micromeritics, Norcross Georgia). Bulk chemical analysis by ICP-AES (inductively coupled plasma-atomic emission spectroscopy) of Mo5Si3/B coupons gave a composition (weight percent) of 82 (±2.5)% Mo, 16.1 (±0.5)% Si, and 1.24 (±0.04)% B.

Undoped Mo_5Si_3 powder was sieved through -635 (20 μm) mesh and pressed into 9.5 mm diameter pellets at 62.5 MPa. The pellets were sintered at 1800°C for two hours under argon to a bulk density of 99% of theoretical. All oxidation coupons were polished in successive steps to 0.3 μm alumina and ultrasonically cleaned in water. Specimens were rinsed in ethanol and dried at 105°C in air before high temperature oxidation.

(2) High Temperature Oxidation

Coupons were suspended from a sapphire wire in a vertical tube thermogravimetric analyzer (System 3, Cahn Instruments, Cerritos, CA). Compressed breathing air with measured dew point -30°±5°C (200-600 ppm water) was flowed over the samples at 100 ml/min. The specimen chamber was purged for 2 hours before each run with the oxidizing gas. Specimen temperature was then increased at 20°C/minute to a set temperature, and held for times up to 410 hours. Specimen mass change and temperature were continuously recorded. Oxidation data for boron modified Mo_5Si_3 differ slightly from previous results reported by us,[22] due to differences in sample processing.

Oxidation data presented here is for powder processed specimens, while previous experiments were carried out on as arc melted samples.

(3) Characterization

Following oxidation runs, samples were characterized for scale composition and microstructure using x-ray diffraction (XRD, Scintag XDS 2000, Scintag USA, Sunnyvale, CA), scanning electron microscopy (SEM, JSM 6100, JEOL USA, Peabody, MA) and energy dispersive spectroscopy(EDS, Oxford Instruments, Oak Ridge, TN), and electron spectroscopy for chemical analysis (ESCA, PHI 5500, Perkin Elmer, Minneapolis, MN) techniques.

III. Results

(1) Oxidation of Mo_5Si_3

Plots of oxidation induced mass change versus time for Mo_5Si_3 at 800° - 1200°C are shown in Figure 1. These plots include the initial ramping up to temperature at 20°C/minute. The mass change behavior during the initial transient temperature region for oxidation of Mo_5Si_3 at 1000°C is shown in Figure 2. The initial rapid mass gain is due to formation of MoO_x ($x \leq 3$) and SiO_2 on the silicide surface. If the oxidation temperature is held at 600°C for long times, a mixed MoO_x and SiO_2 scale develops, as detected using EDS and XRD. As the oxidation temperature is ramped past 750°C, a rapid mass loss is observed due to volatilization of molybdenum oxide. Large amounts of white to yellow crystals with needle-like habit condense on the cooler portions of the furnace tube. These crystals were found by x-ray diffraction to be MoO_3.

At an oxidation temperature of 800°C (Figure 1) continuous mass loss in the steady state temperature region indicates active oxidation of molybdenum, with sudden drops in

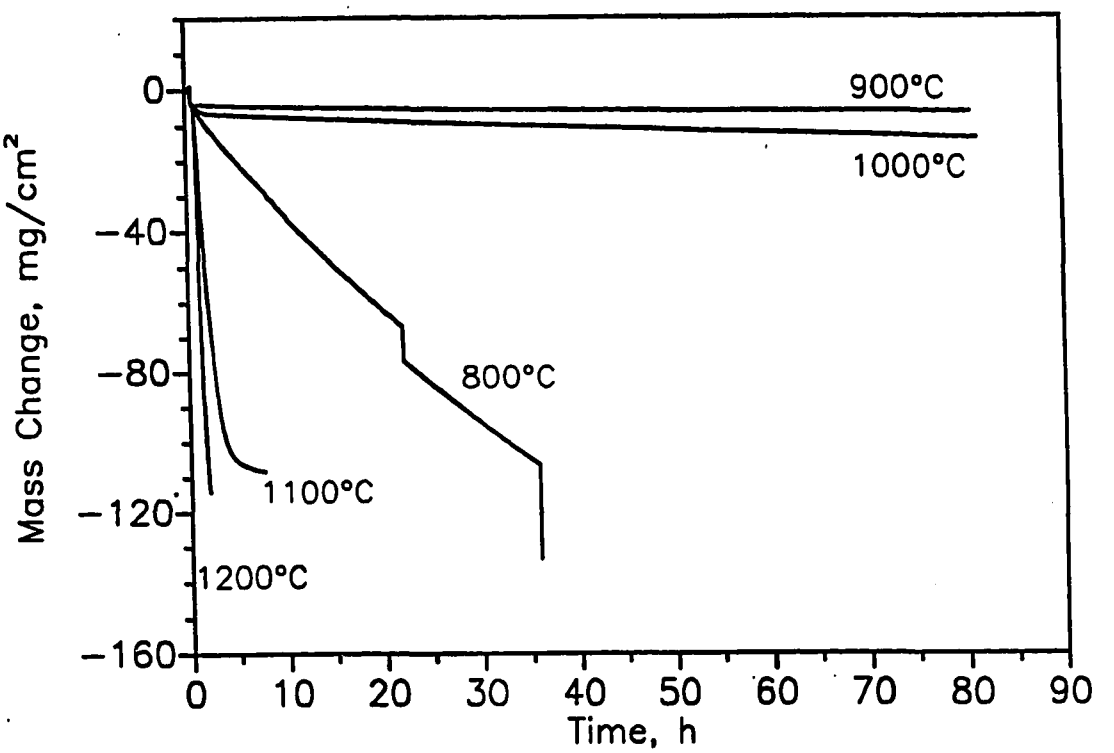

Figure 1. Mass change of Mo_5Si_3 as a function of time on oxidation in air at 800°-1200°C. Experiments halted at 1100° and 1200°C to preserve silicide/oxide interface.

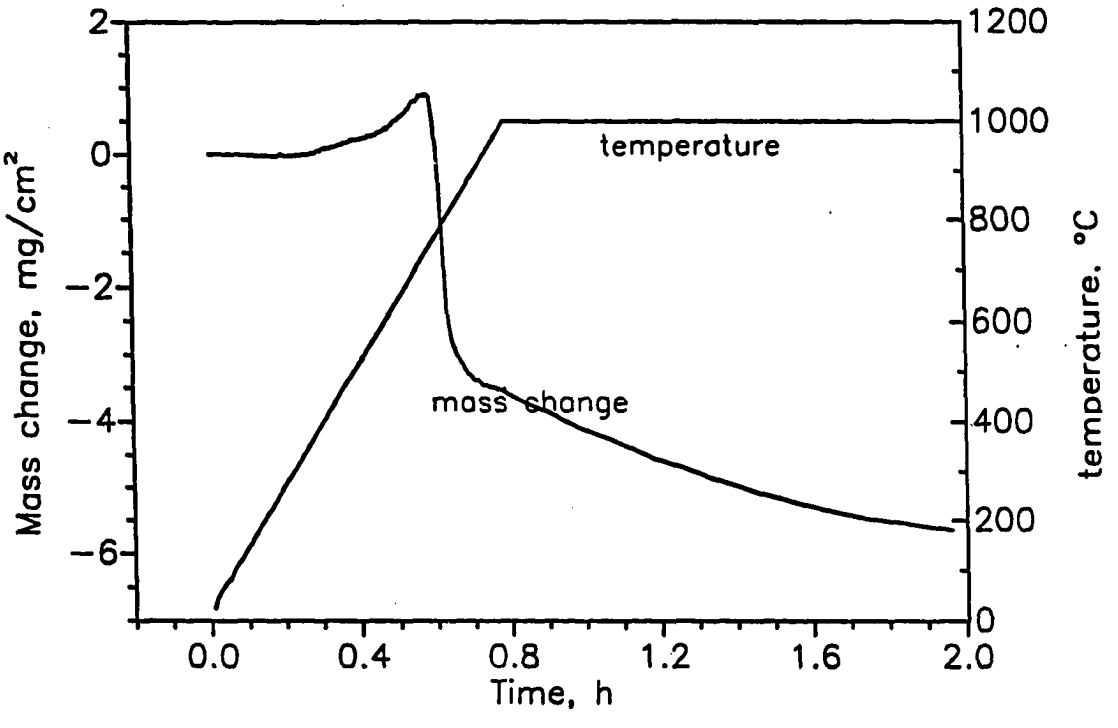

Figure 2. Mass change behavior of Mo_5Si_3 during initial temperature ramp. Initial mass gain due to oxidation of molybdenum and silicon is followed by mass loss due to molybdenum oxide volatilization.

mass indicating material loss due to spallation. The oxidative behavior is similar to the pest[23] commonly observed in low temperature oxidation of $MoSi_2$. After 35 hours at 800°C a mass of loosely held yellow-green oxide powder remains, as shown in Figure 3(a). Spallation was confirmed by accumulation of oxide powder at the bottom of the furnace tube. A portion of the x-ray diffraction pattern of the oxide powder is shown in Figure 4. The pest oxidation product does not match any indexed diffraction pattern[24] for molybdenum silicides, molybdenum and silicon oxides, or hydrated molybdenum and silicon oxides. This unknown phase will be subsequently referred to as U1. There are at least four known mixed valence molybdenum oxides in the stoichiometry range $MoO_{2<x>3}$, and also reports of nonequilibrium phases.[25] It is possible that U1 is a complex mixture of oxides or a nonequilibrium phase. Since the nature of the molybdenum oxide is not known, condensed species will be referred to as MoO_x. Vapor phase species will be referred to as $(MoO_3)_x$.[26]

Oxidation resistance is best at 900°C, with a mass loss of about 0.6 mg/cm^2 in 50 hours after the initial transient period. A buff white scale forms at this temperature, and a small amount of powder can be removed from the scale surface by scraping with a steel probe. X-ray diffraction patterns (Figure 4) of the oxidized surface show some peaks due to the underlying Mo_5Si_3 substrate, as well as formation of an unknown phase, labeled U2. Mo_5Si_3 lines are shifted somewhat from those of the unoxidized substrate, possibly due to solid solution of Mo_5Si_3 with oxygen or strain near the oxidation interface. Lattice parameter refinement indicates that the tetragonal W_5Si_3 structure is retained. No peaks due to crystalline silica were identified, indicating that silica formed is amorphous at this temperature. Some lines from unknown phase U2 match with peaks from U1, indicating that U1 may be a combination of two or more phases. The oxidation rate at 1000°C is 6 times faster than that at 900°C. An SEM micrograph of a cross section of the oxidation

Figure 3. Micrographs of Mo_5Si_3 after oxidation. Top to bottom: a) 800°C for 35 hours, b) 1000°C for 80 hours, c) 1100°C for 8 hours. Fracture cross sections are shown. Note condensation of MoO_x in scale at 1000°C.

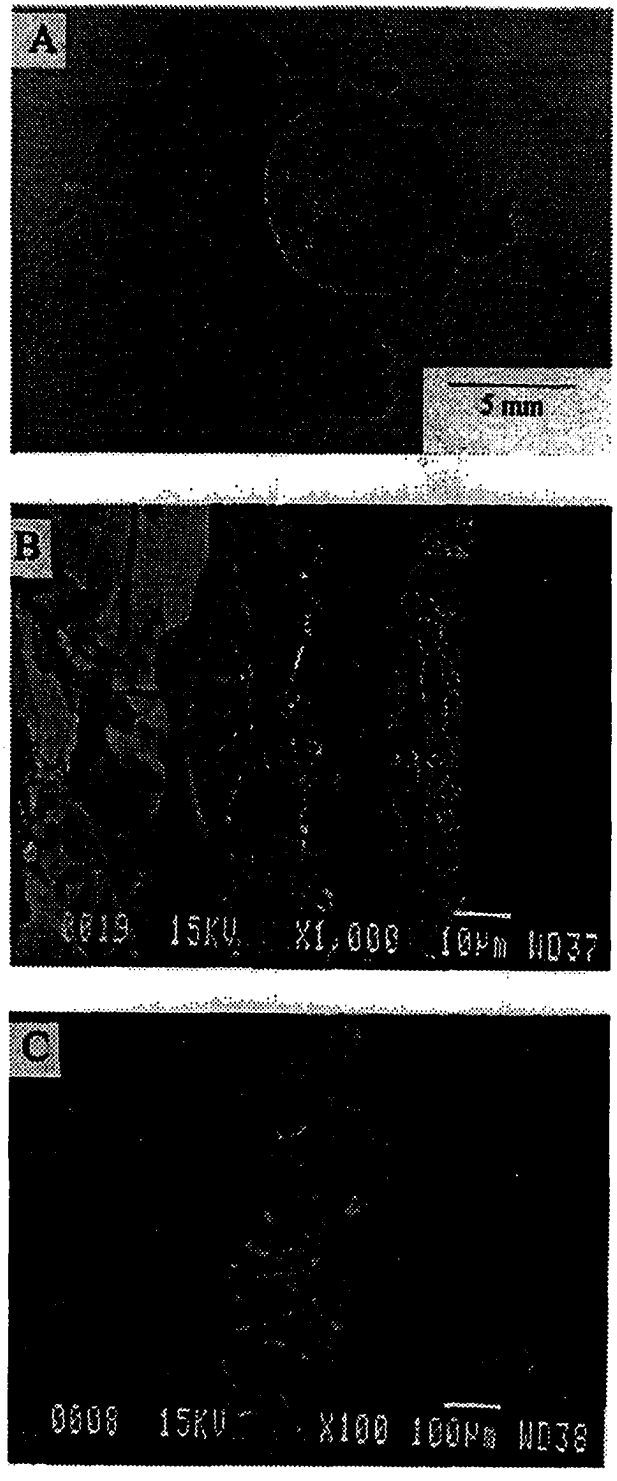
A
5 mm
B
15KV X1,000 10µm WD37
C
15KV X100 100µm WD38

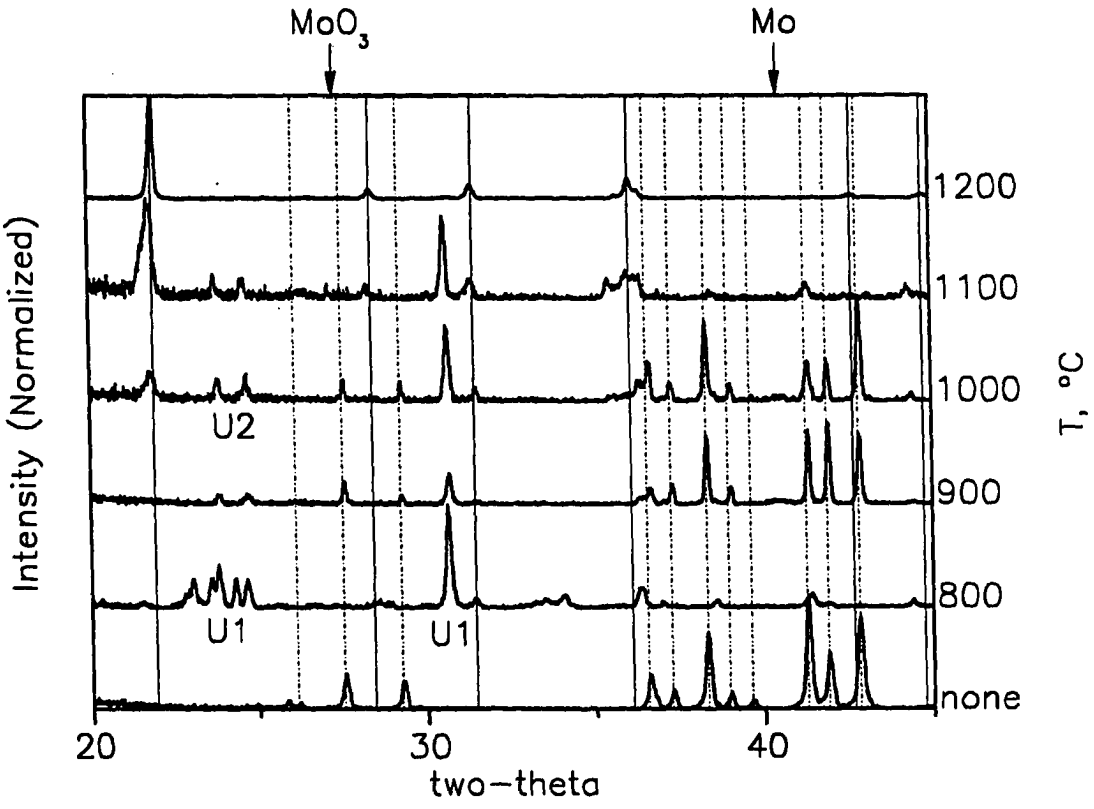

Figure 4. X-ray diffraction patterns of Mo_5Si_3 after oxidation at 800°-1200°C. Solid lines indicate cristobalite (JCPDS 39-1425); dashed lines indicate tetragonal Mo_5Si_3 (JCPDS 34-371). Also shown are positions of MoO_3 and Mo 100% intensity lines. U1 and U2 indicate unknown phase(s).

coupon after 80 hours of oxidation at 1000°C is shown in Figure 3(b). The scales of oxidized specimens were delicate and contained interesting features (such as MoO_3 crystals) that were destroyed on polishing, so that fracture cross sections are shown here. The fracture cross section shows large transverse voids in the scale, with needle-like molybdenum oxide crystals growing into the voids. X-ray diffraction shows the scale to be composed of cristobalite and phase U2. Total scale thickness after 80 hours of oxidation at 1000°C is approximately 50 μm. Oxidation at temperatures above 1000°C becomes very rapid, with the rate at 1100°C being 2400 times faster than at 900°C. A decrease in oxidation rate occurs at 1100°C after the majority of the silicide in the coupon is consumed. Oxidation experiments were stopped at short times at 1100° and 1200°C in order to leave some of the substrate unoxidized and allow for analysis of the oxidation interface. An SEM image of a fracture cross section of the substrate after oxidation for 10 hours at 1100°C is shown in Figure 3(c). The oxidation coupon shows little silicide (bright phase) remaining. An x-ray diffraction pattern (Figure 4) taken after 8 hours of oxidation at 1100°C shows that the (100) diffraction peak from cristobalite has a higher intensity relative to phase U2, when compared to the sample oxidized at 1000°C. No diffraction peaks due to Mo_5Si_3 are evident, consistent with the fact that the substrate is almost completely oxidized. At 1200°C, the oxidation coupon is completely converted to silicon dioxide in less than one hour. The oxidation coupon remained intact at 1200°C, in contrast to the pest oxidation observed at 800°C. X-ray diffraction shows strong peaks due to cristobalite, with no other phases present.

In order to quantify the temperature dependence of the oxidation rate, oxidation data was fit to a linear model. Linear rate constants are given in Table II . Fit to a linear model was good over a the majority of the data range at temperatures of 900°C and 1000°C. Data at 800°C was discontinuous and was not used in rate calculations. A well

defined steady state behavior was not attained at 1100°C and 1200°C. The oxidation rates for these two temperatures represents an average mass loss rate prior to complete conversion of the substrate to SiO_2.

(2) Oxidation of Mo5Si3/B

Figure 5 shows the mass change during isothermal oxidation of Mo5Si3/B at temperatures from 800°- 1300°C. In this temperature range, a hard blue-black scale forms on oxidation, in contrast to the chalky white scale formed on undoped Mo_5Si_3. Initial oxidation behavior of Mo5Si3/B in the transient temperature regime is similar to that undoped Mo_5Si_3, and is not shown. In order to quantify the temperature dependence of the oxidation rate, mass change data was fit to linear or parabolic models after the initial transient oxidation period. Rate constant data from mass change experiments are tabulated in Table III. At 900° and 1000°C, oxidation kinetics were fit to a linear model, with slow mass loss occurring after the initial transient oxidation period. In the range 1050°-1300°C specimens show a slow mass gain at long times. Mass change at long times was modeled by a parabolic equation. Fits of the parabolic model to the data at 1050°-1300°C are shown in Figure 6. Data at 1150°C and 1200°C showed long period oscillations, but tended toward parabolic kinetics at long times. At 800°C no pesting behavior is observed, in contrast to the behavior of undoped Mo_5Si_3. Mass loss data indicates that there are two distinct regimes of oxidation, with oxidation rate slowing by an order of magnitude after approximately 150 hours. The cause of this change in rate is the subject of further study. An x-ray diffraction pattern taken from the scale surface after oxidation at 800°C for 280 hours is shown in Figure 7. The diffraction pattern indicates that the scale contains cristoballite, and that a molybdenum interlayer has formed, presumably at the oxidation interface. An SEM micrograph of the polished scale

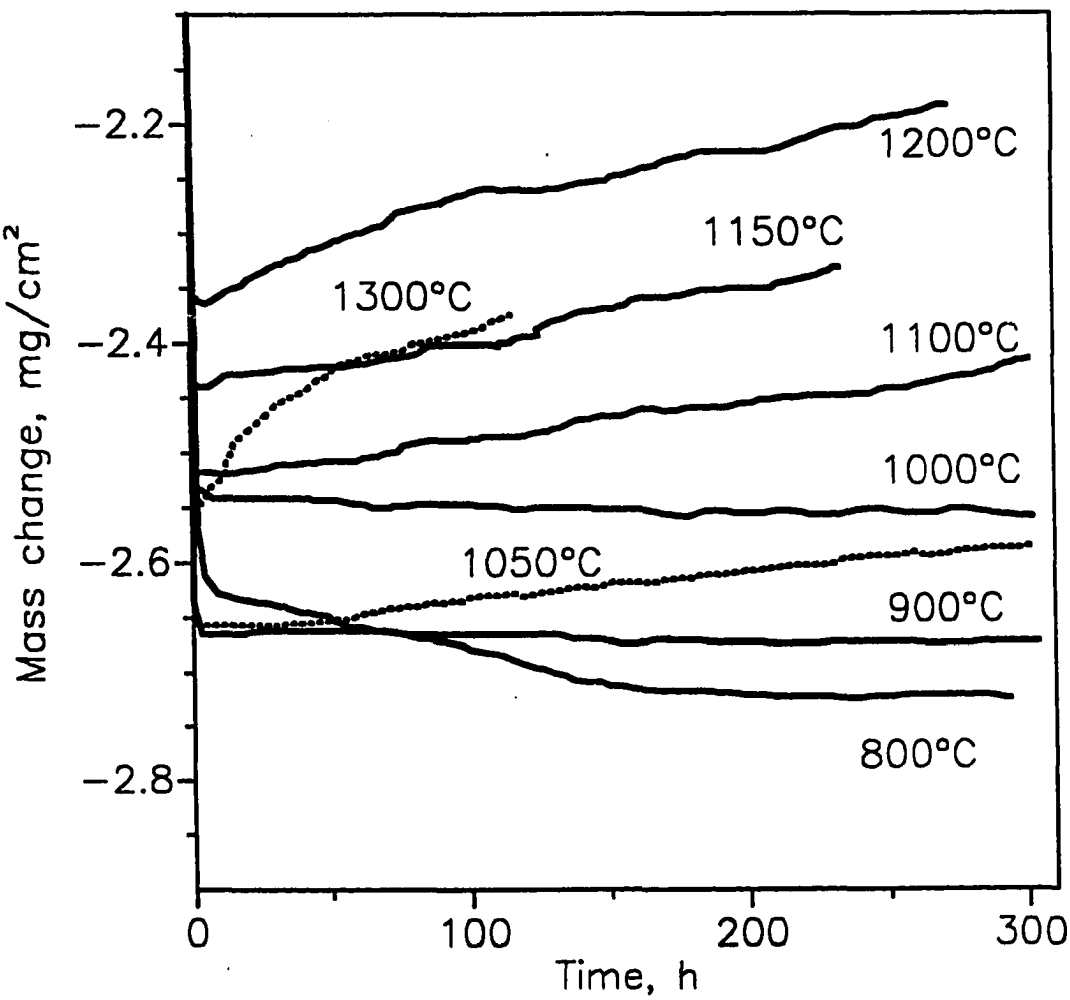

Figure 5. Mass change of Mo5Si3/B as a function of time on oxidation in air at 800°-1300°C. Behavior changes from mass loss to mass gain near 1050°C.

Table II. Rate constants for the oxidation of Mo_5Si_3 based on linear model.

Temperature, °C	Steady state rate constant[1]	Run time, hr.
800	pest	35
900	-1.2×10^{-2}	80
1000	-7.2×10^{-2}	80
1100	$-2.9\times10^{+1}$	10
1200	$-1.3\times10^{+3}$	3

[1]Rate constants given in units of mg cm^{-2} hr^{-1}. Negative rate indicates mass loss.

Table III. Rate constants for the oxidation of Mo5Si3/B.

Temperature, °C	Kinetic model	Steady state[1] rate constant	Run time, hr.
800[2]	linear	-6.0×10^{-4}	15-150
	linear	-5.4×10^{-5}	150-278
900	linear	-3.7×10^{-5}	300
1000	linear	-4.4×10^{-5}	410
1050	parabolic	$+4.3\times10^{-5}$	300
1100	parabolic	$+5.9\times10^{-5}$	300
1150	parabolic	$+9.2\times10^{-5}$	245
1200	parabolic	$+1.6\times10^{-4}$	280
1300	parabolic	$+2.8\times10^{-4}$	115

[1]Rate constants given in units of mg cm^{-2} hr^{-1} for linear model and mg^2 cm^{-4} hr^{-1} for parabolic model. Negative rate indicates mass loss. [2]Break in oxidation rate modeled by two linear rates.

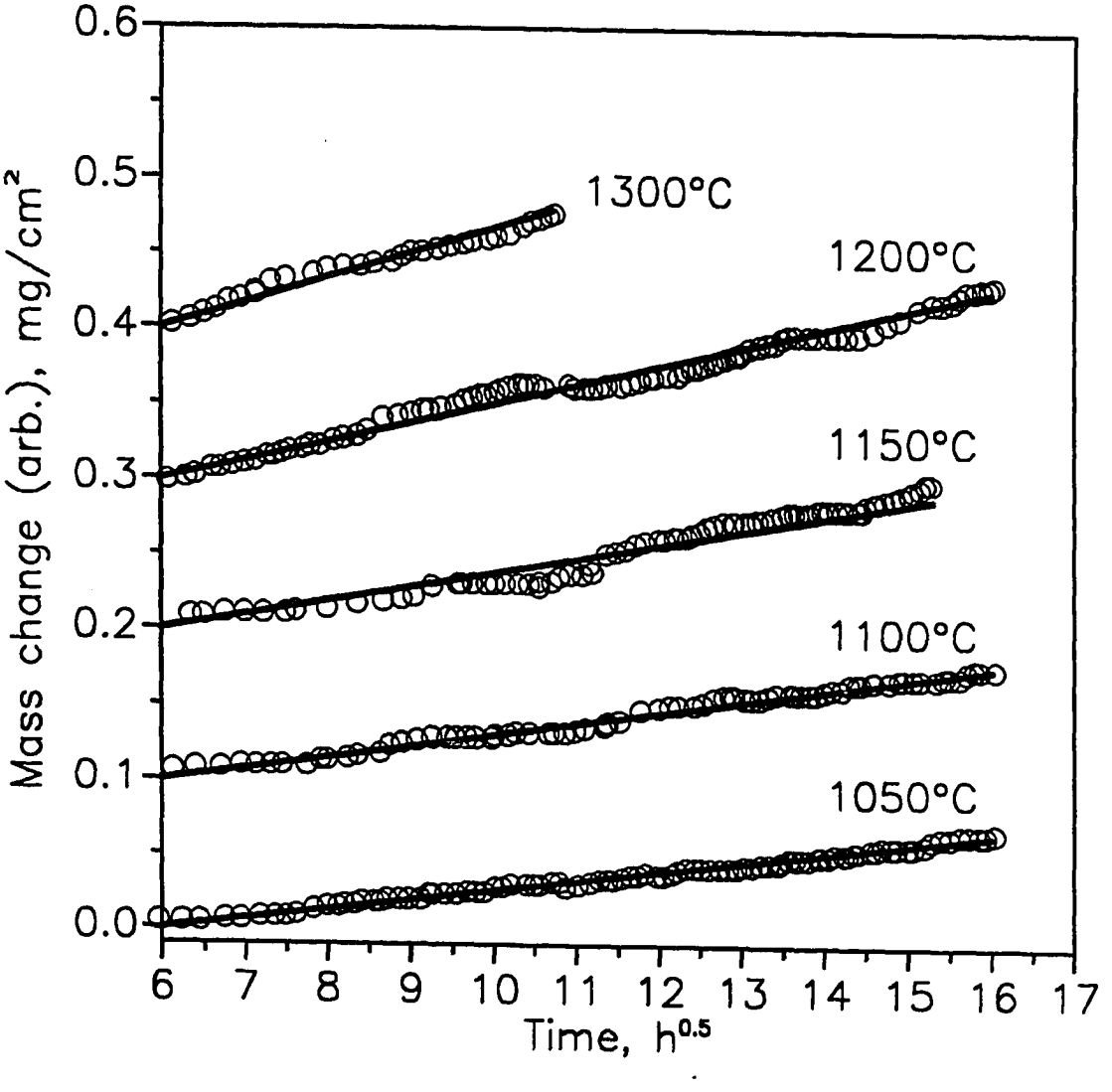

Figure 6. Fit of parabolic model to Mo5Si3/B oxidation data for 1050°-1300°C.

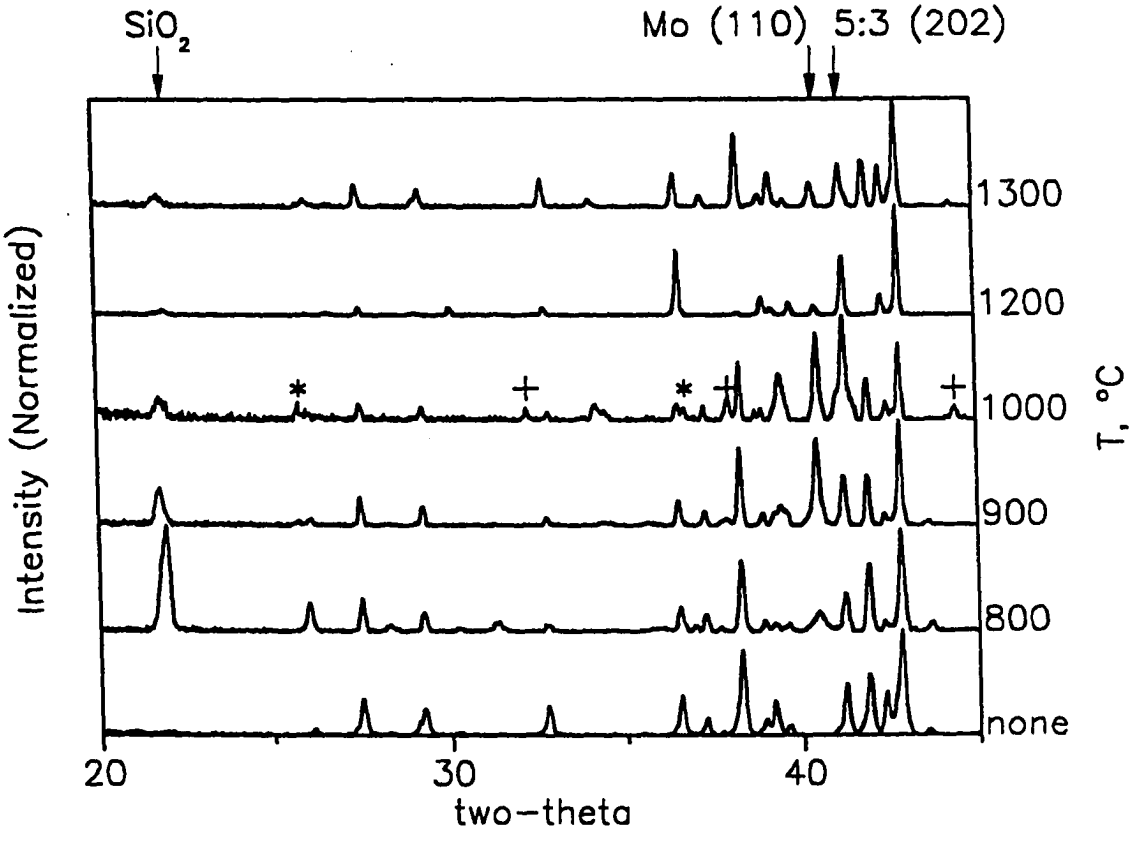

Figure 7. X-ray diffraction patterns of Mo5Si3/B after oxidation at 800°-1300°C. SiO_2 indicates cristobalite (JCPDS 39-1425) and Mo indicates molybdenum (JCPDS 4-0898). Mo_3Si (JCPDS 4-814) peaks are marked by * and Mo_2B (JCPDS 25-561) peaks by +.

cross section is shown in Figure 8(a). The scale is glassy in appearance, nonporous, and about 7 μm thick. SEM of the scale surface indicates that cristobalite forms as particles 1-3 μm in diameter. The molybdenum layer found by x-ray diffraction cannot be detected using EDS elemental mapping or SEM imaging, indicating that the layer is less than 0.5 μm thick. In contrast to undoped Mo_5Si_3, there is no evidence of molybdenum oxide formation in the scale by SEM, XRD, or EDS. As the oxidation temperature is increased to 900°C and 1000°C, x-ray diffraction (Figure 7) indicates that the degree of crystallinity in the scale decreases. This behavior parallels the temperature dependence of devitrification of borosilicate glass.[27] Figure 8(b) is an SEM image of a scale cross section after oxidation at 1000°C for 410 hours. The scale shows no cracking or porosity. Scale thickness is on the order of 7 μm. ESCA analysis indicates that the scale surface resembles borosilicate glass in chemical composition and bonding. An ESCA depth profile shows that the scale is boron depleted at the surface. The boron depletion in the outer regions of the scale may be due to volatilization of B_2O_3, which has a vapor pressure of 10^{-6} atmospheres at 1000°C.[28] At 1000°C, the intensity of the Mo (110) peak seen in the diffraction pattern increases relative to that of the Mo_5Si_3 (202) peak, and weak diffraction from Mo_3Si and Mo_2B are detected. This specimen was oxidized for longer times than other coupons. Other researchers[29] have reported that formation of lower silicides during oxidation of $MoSi_2$ occurs only after long times.

At 1050°C, the steady state oxidation behavior of Mo5Si3/B changes from mass loss to mass gain. This implies a change in the rate controlling step in oxidation, possibly from mixed mode behavior at T≤1000°C, to a diffusion controlled process at 1050°C and above. The mass gain on oxidation at 1100°C is approximately 0.05 mg/cm^2 over fifty hours. XRD indicates that the degree of crystallinity in the scale and the relative amount of molybdenum in the scale decreases at 1200° and 1300°C relative to 1000°C. An SEM

Figure 8. Micrographs of scale formed on Mo5Si3/B after oxidation in air. Top to bottom: a) 800°C for 280 hours, b) 1000°C for 410 hours, c) 1300°C for 117 hours. Voids are believed to be due to sample polishing, as no voids were observed in fracture cross sections.

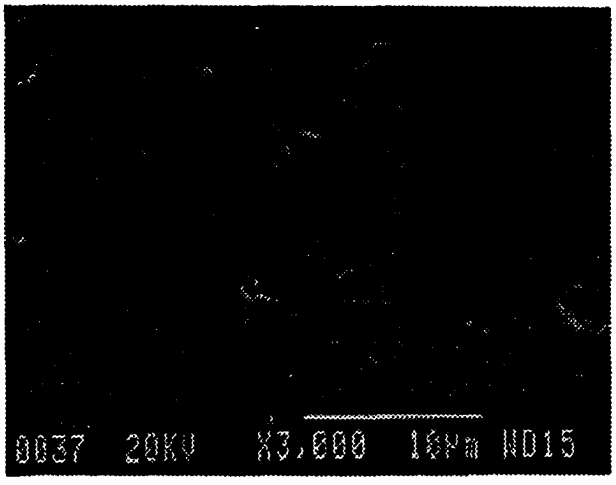
0037 20KV X3,000 10Pm WD15

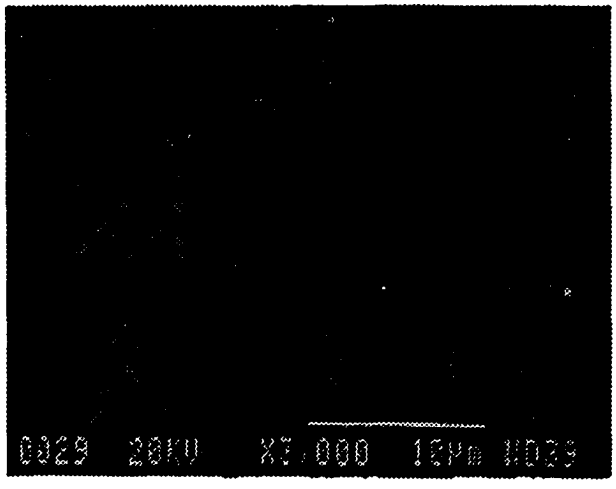
0029 20KV X3,000 10Pm WD39

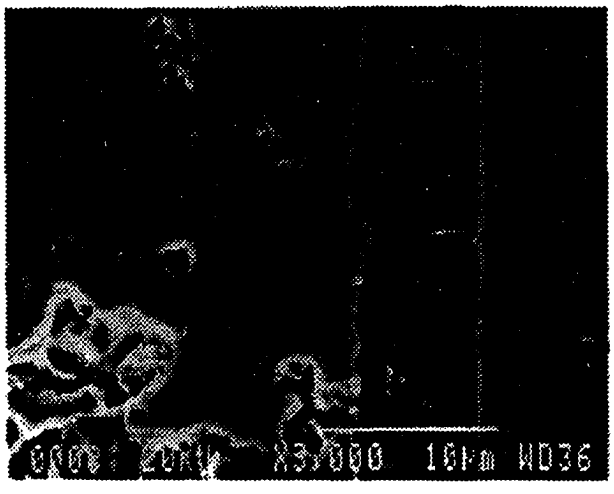
X3,000 10Pm WD36

image of a polished scale cross section after oxidation at 1300°C is shown in Figure 8(c). There is little visible change in scale morphology in the temperature regime 800°-1300°C.

IV. Discussion

(1) Oxidation of Mo_5Si_3

Three possible competing net reactions during the oxidation of Mo_5Si_3 are:

(1) $2\ Mo_5Si_3 + 21\ O_2 \longrightarrow 10\ MoO_3\ (volatile) + 6\ SiO_2$

(2) $3\ Mo_5Si_3 + 4\ O_2 \longrightarrow 5\ Mo_3Si + 4\ SiO_2$

(3) $Mo_5Si_3 + 3\ O_2 \longrightarrow 5Mo + 3SiO_2$

A mass loss on oxidation indicates that reaction (1) is dominant, while a net mass gain indicates that reaction (2) or (3) is dominating. Oxidation experiments with Mo_5Si_3 powder show that silicon loss due to SiO volatilization is negligible when compared to molybdenum oxide volatilization. When held for 300 hours in air at 950°C, Mo_5Si_3 powder converts quantitatively to SiO_2 as predicted by reaction (1).

In general oxidation rates may be limited by reactant or product gas diffusion through the boundary layer exterior to the oxidation coupon, by diffusion of the oxidizing species through the passivating scale to the reaction interface, by diffusion of oxidation products from the reaction interface through the scale, or by the rate of the governing oxidation reaction.

By comparing the rate of molybdenum volatilization from Mo_5Si_3 to that of molybdenum metal, an idea of the degree of oxidation protection provided by the scale

can be determined. The linear model used to calculate oxidation rates based on mass change represents the sum of mass gain due to silicon and molybdenum oxidation and mass loss due to molybdenum volatilization. By assuming that all silicon is converted to (non volatile) SiO_2, and that all molybdenum is oxidized and volatilized (reaction (1)), the order of magnitude of the rate of molybdenum volatilization can be calculated. These assumptions can be seen to hold true at 1200°C, where complete conversion of the silicide oxidation coupon to silica takes place in less than 1 hour. The rate of molybdenum consumption calculated during oxidation at 1200°C is on the order of 10^{17} atoms/cm^{2}s. Gulbransen et al.[30] conducted molybdenum oxidation experiments at high temperatures and found that the rate of molybdenum consumption varied with surface area from 1.05 x 10^{18} to 7.92 x 10^{18} atoms/cm^{2}s at a furnace temperature of 1200°C in 10.1 kPa (76 torr) oxygen. This reaction rate is just one order of magnitude faster than that calculated for Mo_5Si_3. It is apparent that the scale formed on undoped Mo_5Si_3 provides very little barrier to the diffusion of oxygen, i.e. oxygen has a short circuit path for transport to the oxidation interface, perhaps due to gas phase transport through a cracked or porous scale. SEM examination of scale cross sections confirms the porous nature of the scale formed on Mo_5Si_3.

At 400°-1400°C, the free energy of reactions (2) and (3) is lower than that of reaction (1).[31,32] At 1027°C, for example, the free energy of reaction (2) is calculated to be -566 kJ/molO_2, that of reaction (3) is -343 kJ/mol O2, and that of reaction (1) is -212 kJ/molO_2. If oxygen transport is rate limiting, then oxygen partial pressure (P_{O_2}) at the oxidation interface should be fixed roughly by reaction (2) at Si/SiO_2 equilibria. Oxygen partial pressure for Si/SiO_2 at this temperature is on the order of 10^{-27} atm, a value below that required for appreciable molybdenum oxidation. A molybdenum rich interlayer should thus form as silicon is depleted by oxidation.

XRD, however, indicates that no Mo_3Si or Mo is formed on oxidation of undoped Mo_5Si_3. If oxygen transport is rate limiting, net mass gain should occur as dictated by reactions (2) or (3) . In the case of undoped Mo_5Si_3, mass loss occurs at all temperatures, indicating that oxygen partial pressure is not determined by Si/SiO_2 equilibria and that molybdenum is oxidized by reaction (1). The above observations indicate that the oxidation rate is not controlled by oxygen transport to the interface. The remaining possible rate controlling mechanisms are transport of $(MoO_3)_x$ away from the oxidation interface through the scale or gas boundary layer or the rate of reaction (1).

If $(MoO_3)_x$ diffusion outward through the scale is rate limiting, then there should be a concentration gradient of $(MoO_3)_x$ across the scale,[33] with high $(MoO_3)_x$ concentration in the interior of the scale. If $(MoO_3)_x$ diffusion through the boundary layer adjacent to the scale is rate limiting, then there should be a uniform concentration of $(MoO_3)_x$ across the scale. If the rate of reaction (1) is rate controlling, then the there should be no such gradient and the $(MoO_3)_x$ concentration in the scale should be the same as in the ambient furnace atmosphere, essentially zero. On cooling, gas phase $(MoO_3)_x$ concentration gradients will be manifest as condensed phase MoO_x concentration gradients. At 900° -1100°C, it is observed (Fig 3(b)) that a large amount of MoO_x crystals were trapped in the scale after cooling from oxidation tests, indicating that outward transport of $(MoO_3)_x$ is rate limiting. Quantitative EDS analysis of the Mo content as a function of distance could not be made on the rough surface of the fracture cross section, and MoO_x crystals were removed entirely on polishing specimens, so that the rate limiting mechanism for $(MoO_3)_x$ transport could not be established.

(2) Effect of Boron Addition on Oxidation of Mo_5Si_3

The addition of boron gives a significant increase in oxidation resistance. At 1050°C and above, oxidation proceeds with a net mass gain (after the initial mass loss), indicating that reaction (2) or (3) dominates oxidation. The scale formed on Mo5Si3/B (Figure 8) is glassy and non-porous in appearance, in contrast to the porous scale formed on Mo_5Si_3. Oxidation kinetics fit well to a parabolic model at 1050°-1300°C, and formation of a molybdenum rich layer is observed, suggesting that the oxidation process is controlled by diffusion of oxygen through a coherent scale.

Further evidence is given by the close correspondence of the activation energy for oxidation of Mo5Si3/B with that for oxygen diffusion through a borosilicate glass. Figure 9 shows a plot of the temperature dependence of the parabolic oxidation rate in the temperature range 1050° -1300°C for Mo5Si3/B. The oxidation mechanism is assumed to remain constant in this regime, and an activation energy of 134 kJ/mol is calculated. The rate of oxygen diffusion through borosilicate glass was calculated by Schlichting[34] from data obtained by oxidizing silicon substrates coated with sol gel derived borosilicate glass. In the temperature range 700°-800°C, the activation energy for oxygen diffusion was calculated to be 138 kJ/mol for glasses with 10 to 30 mole percent B_2O_3 content. Assuming no change in the activated diffusional process as temperature increases,[35] the activation energy for diffusion of oxygen through borosilicate glass compares well to the activation energy for oxidation of Mo5Si3/B. The above evidence indicates that oxygen diffusion through a coherent scale is the rate limiting step in the oxidation of Mo5Si3/B at 1050°-1300°C.

During the oxidation of undoped Mo_5Si_3, a mixed SiO_2/MoO_x oxide scale initially forms, covering the surface of the specimens. At approximately 750°C, MoO_x

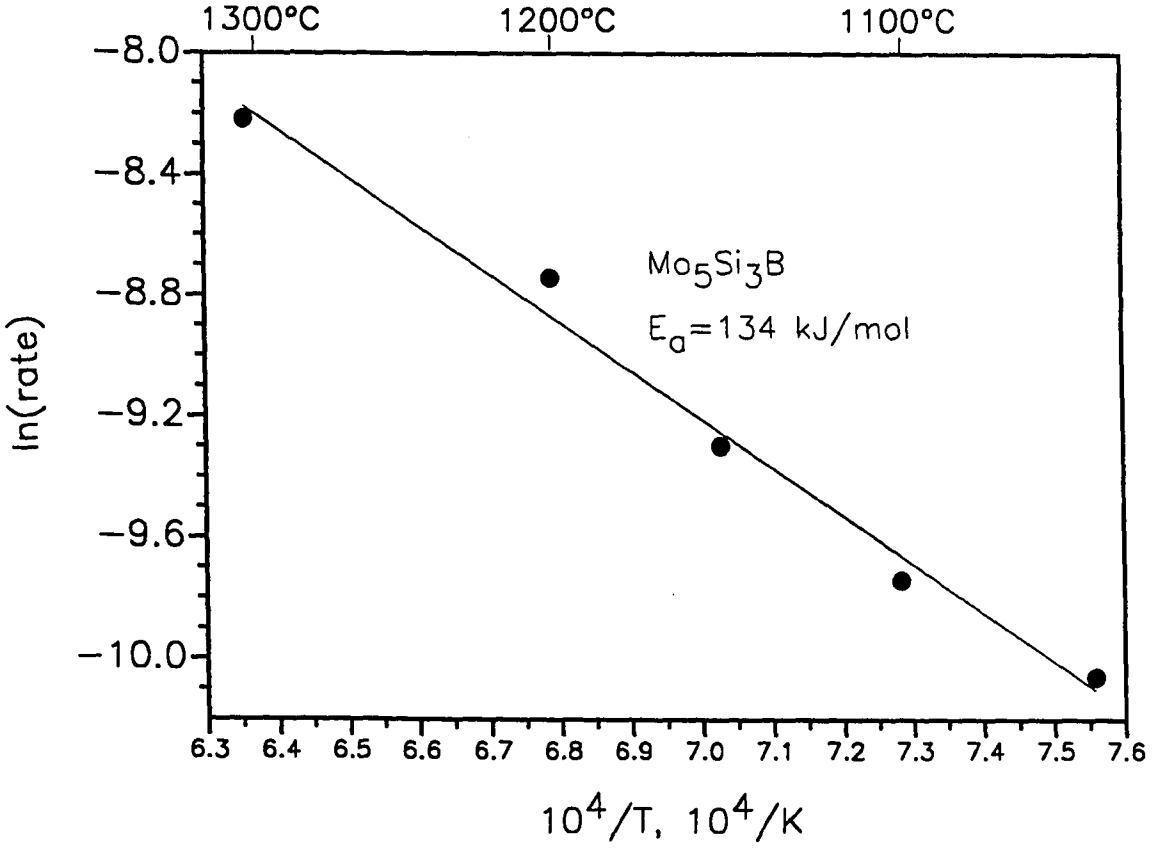

Figure 9. Arrhenius plot of temperature dependence of oxidation of Mo5Si3/B in 1050°-1300°C temperature range.

volatilizes, leaving a porous silica layer behind. This scale provides little in the way of a diffusion barrier for oxygen. The improvement in oxidation resistance provided by boron additions is attributed to formation of a low viscosity borosilicate scale which can flow to form a coherent scale. Similar behavior has been described by Fitzer[18] for germanium additions to $MoSi_2$ that prevent low temperature pest.

Mass loss during oxidation of Mo5Si3/B at 800°-1000°C may be related to lack of silicon activity at the oxidation interface, or to the lack of viscous flow of the scale at low temperatures. If diffusion of silicon to the oxidation interface is not adequate at lower temperatures, P_{O_2} will not be maintained near Si/SiO_2 equilibria. In this case, oxidation will proceed (at least partially) by reaction (1) with a mass loss and no formation of a molybdenum rich interlayer. If oxidation was controlled solely by oxygen transport, then mass gain would occur by reaction (2) or (3). It is observed by XRD (Figure 7) that less Mo rich interlayer formation occurs at 800°C relative to 1000°C. Mass loss coupled with increased Mo formation provide evidence that the oxidation interface becomes silicon and boron depleted at 800°-1000°C. Alternatively, scale viscosity may be too high to exhibit the degree of self- healing behavior due to viscous flow possible at higher temperatures. Small pores in the scale would allow short circuit paths for oxygen transport to the oxidation interface and active oxidation of molybdenum at areas local to the voids. No evidence for through scale porosity was found by SEM, although nanometer scale porosity would not be easily resolvable.

V. Conclusion

The oxidation of Mo_5Si_3 at 800°C is catastrophic, showing low temperature pest behavior similar to that seen in $MoSi_2$. In the range 900°-1100°C, oxidation proceeds with a mass loss due to volatilization of molybdenum oxide. Inspection of the scale by SEM confirms that the scale formed is cracked and porous, with many short circuit paths for oxygen diffusion. Experimentally, it was shown that the scale provides little protection from transport of oxygen to the oxidation interface, since i) oxidation proceeds by mass loss with no molybdenum rich inter layer formation and ii) large amounts of MoO_x crystals form in the scale. Oxidation at 900°-1100°C appears to be controlled by the outward diffusion of $(MoO_3)_x$. Oxidation at 1200°C is very rapid, with complete conversion of a 1 mm thick specimen to silica occurring in less than one hour.

The oxidation resistance of Mo_5Si_3 can be substantially improved with less than two weight percent boron addition. The resulting material is tri-phasic, consisting of tetragonal Mo_5Si_3, MoB, and $MoSi_2$. SEM observation of the scale shows that a glassy, non porous scale is formed at temperatures from 800°-1300°C. The activation energy for oxidation of Mo5Si3/B is calculated to be 134 kJ/mol in the temperature range 1050°-1300°C, and compares well with the activation energy for diffusion of oxygen in borosilicate glass. Oxidation occurs with mass gain above 1050°C, and kinetics fit a parabolic model. Formation of a molybdenum interlayer occurs at all temperatures tested. This evidence suggests that the reason for the improved oxidation resistance of Mo5Si3/B is the formation of a coherent scale. The rate limiting step in oxidation above 1050°-1300°C appears to be oxygen diffusion through the scale.

Acknowledgment: The authors wish to thank Jim Anderegg for ESCA measurements. Ames Laboratory is operated for the U.S. Department of Energy by Iowa State University under contract number W-7405-ENG-82. This research was supported by the Office of Basic Energy Science, Materials Science Division.

References

[1]R.M. Aiken Jr., "On the Ductile-to Brittle Transition Temperature in $MoSi_2$," *Scr. Metall. Mater.*, **26** [7] 1025-30 (1992).

[2]D.P. Mason, D.C. Van Aken, "The Effect of Microstructural Scale on the Hardness of $MoSi_2$-Mo_5Si_3 Eutectics," *Scr. Metall. Mater.*, **28** [2] 185-89 (1993).

[3]S.A. Maloy, A.H. Heuer, J.J. Lewandowski, T.E. Mitchell, "On the Slip Systems in $MoSi_2$," *Acta. Metall. Mater.*, **40** [11] 3159-65 (1992).

[4]S.R. Srinivasan, R.B. Schwarz, "Elastic Moduli of $MoSi_2$ Based Materials," *J. Mater. Res.*, **7** [7] 1610-13 (1993).

[5]S. Bose, "Engineering Aspects of Creep of Molybdenum Disilicide," *Mater. Sci. Eng.*, **A155** [1-2] 217-25 (1992).

[6]Y. Umakoshi, T. Hirano, T. Sakagami, T. Tamanee,"Slip Systems and Hardness in $MoSi_2$ Single Crystals," *Scr. Metall.*, **23** [1] 87-90 (1989).

[7]G. Sauthoff, "Intermetallic Phases as High Temperature Materials," *Z. Metallkd.*, **77** [10] 554-66 (1986).

[8]C.D. Wirkus, D.R. Wilder, "High-Temperature Oxidation of Molybdenum Disilicide," *J. Am. Ceram. Soc.*, **49** [4] 173-77 (1966).

[9]R.E. Regan, W.A. Baginski, C.A. Krier, "Oxidation Studies of Complex Silicides for Protective Coatings," *Ceram. Bull.*, **46** [5] 502-9 (1967).

[10]C.G. McKamey, P.F. Tortorelli, J.H. DeVan, C.A. Carmichael, "A Study of Pest Oxidation in Polycrystalline $MoSi_2$," *J. Mater. Res.*, **7** [10] 2747-55 (1992).

[11]P.J. Meschter, "Low-Temperature Oxidation of Molybdenum Disilicide," *Metallurgical Trans. A*, **23A** 1763-72 June 1992.

[12]A.K Vasudevan, J.J. Petrovic,"A Comparitive Overview of Molybdenum Disilicide Composites," *Mat. Sci. Eng. A*, **A155** 1-17 (1992).

[13]B.F. Gilp, P.D. Desai, C.Y. Ho, *Bibliography on Silicides*, MIAC Report 3, Metals Information and Analysis Center, West Lafayette, IN (1993).

[14]J.J. Petrovic, "$MoSi_2$-Based High-Temperature Structural Silicides," *MRS Bull.*, **18** [7] 35-40 (1993).

[15]B. Aronsson, "The Crystal Structure of Mo_5Si_3 and W_5Si_3," *Acta. Chem. Scand.*, **9** [7] 1107-10 (1955).

[16]N. Christensen, "Preparation and Characterization of Mo_3Si and Mo_5Si_3," *Acta. Chem. Scand.*, **A37** 519-22 (1983).

[17]D.L. Anton, D.M. Shah, "High Temperature Properties of Refractory Intermetallics," *Mat. Res. Soc. Symp. Proc.*, **213** 733-39 Materials Research Society, Pittsburg, PA (1991).

[18] E. Fitzer, "Oxidation of Molybdenum Disilicide," pp. 19-41 in Ceramic Transactions vol. 10: Corrosive and Erosive Degradation of Ceramics, R.B. Tressler and M. McNallan, eds., American Ceramic Society, Westerville, OH (1989).

[19]R.W. Bartlett, J.W. McCamont, P.R. Gage, "Structure and Chemistry of Oxide Films Thermally Grown on Molybdenum Silicides," *J. Am. Ceram. Soc.*, **48** [11] 551-58 (1965).

[20]R. Beyers, "Thermodynamic Considerations in Refractory Metal-Silicon-Oxygen Systems," *J. Appl. Phys.*, **56** [1] 147-52 (1984).

[21]J.B. Berkowitz-Mattuck, R.R. Dils, "High-Temperature Oxidation; II. Molybdenum Silicides," *J. Electrochem. Soc.*, **112** [6] 583-89 (1965).

[22] A.J. Thom, M.K. Meyer, M. Akinc, Y. Kim, "Evaluation of $A_5Si_3Z_x$ intermetallics for Use as High Temperature Structural Materials," pp 413-33 in *Processing and Fabrication of Advanced Materials for High Temperature Applications-III,* ed T.S. Srivatsan and V.A. Ravi, The Minerals, Metals, and Materials Society, Warrendale, PA (1993).

[23]T.C. Chou, T.G. Nieh, "Mechanism of $MoSi_2$ Pest During Low Temperature Oxidation," *J. Mater. Res.*, 1 [8] 214-27 (1993).

[24] JCPDS-International Center for Diffraction Data, Swarthmore, PA (1993).

[25]L. Chang, B. Phillips, "Phase Relations in Refractory Metal-Oxygen Systems," *J. Am. Ceram. Soc.*, **52** [10] (1969).

[26]M. S. Samant, A.S. Kerkar, S.R. Bharadwaj, S.R. Dharwadkar, " Thermodynamic Investigation of the Vaporization of Molybdenum Trioxide," *J. Alloys and Comp.*, [187] 373-9 (1992).

[27]J. Jean, T.K. Gupta,"Alumina as a Devitrification Inhibitor during Sintering of Borosilicate Glass Powders", *J. Am. Ceram. Soc.*, **76** [8] 2010-16 (1993).

[28]M.S.Chandrasekharaiah, "Volatilities of Refractory Inorganic Compounds," pp. 495-506 in *The Characterization of High Temperature Vapors*, J.L. Margrave, ed., John Wiley, New York, NY (1967).

[29] D.A. Berztiss, R.R. Cerchiara, E.A. Gulbransen, F.S. Pettit, G.H. Meier, "Oxidation of $MoSi_2$ and Comparison with Other Silicide Materials," *Mater. Sci. Eng.*, **A155** 165-81 (1992).

[30]E.A. Gulbransen, K.F. Andrew, F.A. Brassart, "Oxidation of Molybdenum at 550° to 1700°C," *J. Electrochem. Soc.*, **110** [9] 952-9 (1963).

[31]M.W. Chase, C.A. Davies, J.R. Downey, D.J. Frurip, R.A. McDonald, A.N. Syverud, *JANAF Thermochemical Tables*, 3rd edition, J. Phys. Chem. Ref. Data, Vol. 14, Suppl 1, American Chemical Society, New York, NY (1985).

[32]L.B. Pankrantz, *Thermodynamic Properties of Elements and Oxides*, U.S. Department of the Interior Bureau of Mines Bulletin 672, Washington, D.C. (1982).

[33]K.L. Luthra, "Some New Perspectives on Oxidation of Silicon Carbide and Silicon Nitride," *J. Am. Ceram. Soc.*, **74** [5] 1095-1103 (1991).

[34]J. Schlichting, "Oxygen Transport through Glass Layers Formed by A Gel Process," *J. Non-Crystall. Solid.*, **63** 173-81 (1984).

[35]J.D. Kalen, R.S. Boyce, J.D. Cawley, "Oxygen Tracer Diffusion in Vitreous Silica," *J. Am. Ceram. Soc.*, **74** [1] 203-209 (1991).

CHAPTER 3:
OXIDE SCALE FORMATION ON Mo-Si-B INTERMETALLICS AT 600°-1075°C

A manuscript to be submitted to the *Journal of the American Ceramic Society*

Mitchell K. Meyer and Mufit Akinc
Ames Laboratory and Department of Materials Science and Engineering
Iowa State University, Ames, IA 50011

Abstract

Initial scale formation in the range 600°-1075°C and isothermal oxidation behavior at 1000°C was investigated for five Mo-Si-B intermetallic compositions containing 81-88 weight percent molybdenum. All compositions exhibited an initial transient oxidation period consisting of a mass gain due to MoO_3 and SiO_2 formation, followed by a rapid mass loss starting at 750°C due to MoO_3 volatilization. The magnitude of the mass loss was found to vary with the initial pore size and total porosity of the scale. After the initial transient oxidation period, oxidation proceeded at a slower, steady state rate. During isothermal oxidation at 1000°C the oxidation rate was found to vary inversely as the ratio of B/Si in the scale, indicating that viscous flow of the scale was an important factor in determining the isothermal oxidation rate. Transient oxidation behavior was modelled using viscous sintering theory to describe the reduction in pore area available for oxygen transport. Predictions of the model agree with experimental observations of scale formation and oxidation kinetics.

I. Introduction

Mo_5Si_3 based materials are candidates for high temperature applications where good creep resistance is required. The creep resistance of Mo_5Si_3 has been shown to be about an order of magnitude higher than that of $MoSi_2$ at 1200°C.[1] Mo_5Si_3, however, has poor high temperature oxidation resistance, with a mass loss on the order of 100 mg/cm²·hr at 1200°C.[2]

The oxidation of Mo_5Si_3 has been studied previously, often in comparison to $MoSi_2$. Oxidation of Mo_5Si_3 is characterized by porous scale formation and active oxidation below 1650°C, with a transition to protective scale formation and passive oxidation at higher temperatures.[3] The reason for non-passivating scale formation has been explained in terms of two causes. The first possible cause is porous scale formation. If the scale initially forms with a high volume fraction of MoO_3, subsequent volatilization of MoO_3 (above ≈750°C) leaves a porous silica network. Alternatively, if the volume of scale produced is less than the volume of substrate consumed the scale will not completely cover the substrate surface. Both processes lead to formation of a porous scale in the abscence of viscous flow. Scale porosity allows oxygen transport via a short circuit path to the underlying silicide, allowing faster oxidation than would be expected from a diffusion controlled process.

Berkowitz-Mattuck and Dils[4] studied the oxidation of Mo_5Si_3 by monitoring oxygen consumption during oxidation at temperatures of 1107°-1737°C and oxygen pressures of 1082-1750 Pa (8.5-13.1 Torr). Oxidation times were 80-110 minutes. At 1107° and 1137°C, oxygen consumption was rapid over the duration of the oxidation test, indicating active oxidation and non-protective scale formation. Above 1377°C, specimens exhibited a plateau region of slow oxygen uptake after an initial transient period of rapid oxidation. Total oxygen consumption decreased as oxidation temperature increased. High temperature

passivation was proposed to be due to the temperature dependent lateral flow of SiO_2 to form a continuous passivating layer.

A second possible cause of oxidative instability is depletion of silicon at the oxidation interface. The conditions necessary for oxidation of the metal in a metal silicide that forms a coherent scale have been discussed by several authors in relation to silicide coatings on silicon substrates.[5,6] Bartlett, et al.[7] used this approach to explain the poor oxidation resistance in Mo_5Si_3, in contrast to the excellent oxidation resistance of $MoSi_2$. Mo_5Si_3 was oxidized between 450°-1500°C in the oxygen partial pressure range of $10\text{-}10^5$ Pa. Protective scale formation was found to occur only at temperatures greater than 1650°C at atmospheric oxygen pressure. Silicon depletion at the oxidation interface due to slow silicon diffusion (D_{Si}) from the matrix was modelled as the cause of oxidative instability. The oxidation interface may become depleted in silicon due to reaction with oxygen to form SiO_2. If the rate at which silicon is consumed by reaction to form SiO_2 is greater than D_{Si}, the interface becomes silicon depleted. The chemical activity of silicon at the interface (a_{Si}) falls, and the oxygen partial pressure (P_{O_2}) at the interface is no longer fixed by Si/SiO_2 equilibria. P_{O_2} may rise to a level where oxidation of molybdenum is thermodynamically possible. Oxidation of molybdenum and subsequent volatilization of MoO_3 may cause scale rupture, allowing active oxidation to occur. Increasing temperature was correlated with an increase in D_{Si}, thereby increasing a_{Si} and decreasing P_{O_2}, preventing oxidation of molybdenum.

Previous work in our laboratory[2] has shown that boron additions in the range 1-2 weight percent increase the oxidation resistance of Mo_5Si_3 by about five orders of magnitude at 1200°C. The present work elaborates on the mechanism of oxidation protection brought about by boron additions to the Mo-Si system in the vicinity of the Mo_5Si_3 phase field. Scale formation behavior and oxidation kinetics are examined as a function of composition for materials with 81-88 weight percent molybdenum content.

II. Experimental Procedure

(1) Preparation of Oxidation Coupons

Mo-Si-B intermetallics were synthesized by arc melting of the elements in a non-consumable tungsten arc melt furnace under argon atmosphere. The molybdenum source was molybdenum foil of 99.95% purity (Philips Elmet, Lewiston, ME). Silicon was in the form of 3-20 mm pieces (Alpha Chemicals, Danvers, MA) of purity 99.995%, and boron was 2-3 mm size material of 99.5% purity (AESAR, Ward Hill, MA). Results of chemical analysis by ICP-AES (Inductively Coupled Plasma-Atomic Emission Spectroscopy) for the five compositions examined in this work are given in Table I. Typical impurity analysis is given elsewhere.[2] Compositions were chosen in order to vary the type of matrix in the microstructure, total atomic fraction of boron and silicon relative to molybdenum, and the ratio of boron to silicon.

Arc melt buttons were ground in air to submicron size powders in a tungsten carbide lined impact mill (Model 2000 Mixer/Mill, SPEX Industries, Edison, NJ). One weight percent cellulose ether (Methocel®, Dow Corning, Midland, MI) was added to prevent powder agglomeration during milling. Powders were sieved through -635 mesh (<20 μm) after milling and pressed into 0.95 cm diameter pellets at 50 MPa. Pellets were heated under argon at 5°C/min to 600°C and held for two hours to burn off the cellulose ether added during grinding Pellets were then sintered under high purity argon at 1800°C for 2 hours to a density greater than 90% of theoretical. To further densify, samples were hot isostatically pressed at 1750°C and 280 MPa with no container. Samples were annealed at 1600°C for 24 hours under high purity argon to obtain better chemical and microstructural homenegeity. Phase arrays were determined by using x-ray diffraction (XRD, XDS 2000, Scintag USA, Sunnyvale, CA), scanning electron microscopy (SEM, JSM 6100, JEOL USA, Peabody, MA), and energy dispersive spectroscopy (EDS, Pentafet® detector, Oxford

Table I. Compositions of Mo-Si-B intermetallics

Specimen	Weight%[1]			Mol%		
Number	Mo	Si	B	Mo	Si	B
I	81.2	18.2	0.61	54.5	41.8	3.60
II	81.5	18.3	0.14	56.1	43.1	0.79
III	82.2	16.9	0.91	55.6	38.9	5.45
IV	86.3	12.6	1.1	62.2	31.1	6.72
V	88.2	10.8	1.0	65.9	27.4	6.60

[1]All compositions ±3 wt% relative

Instruments, Oak Ridge, TN). Specimens used for SEM/EDS examination were etched with Murakami's etch to better differentiate between T2 ($Mo_5(Si,B)_3$) and Mo_3Si phases, which have nearly the same BSE contrast. The etch selectively attacks the T2 and MoB phases.

Oxidation coupons 1 mm thick were cut from pellets using a diamond saw. Coupons were polished in successive steps to 0.3 μm alumina and ultrasonically cleaned and rinsed in distilled water. Specimens were rinsed in ethanol, acetone, and hexane and dried at 105°C in air before high temperature oxidation.

(2) High Temperature Oxidation

Two types of oxidation experiments were conducted. The first test was designed to allow the observation of scale development as a function of temperature from 600°-1075°C. Oxidation coupons were placed on edge in alumina boats inside a quartz tube. The tube and contents were purged with high purity synthetic air for two hours prior to oxidation. Gas flow rate and tube diameter were constant for all experiments. After purging, coupons were

heated at a rate of 10°C/min until the desired oxidation temperature was reached. At this temperature the quartz tube was immediately slid through the tube furnace to remove the designated coupon from the hot zone. In this way, samples were rapidly quenched from the oxidation temperature. Gas flow was counter current to the tube movement so that volatile oxidation products would not condense on pellets after removing from the hot zone.

Thermogravimetric oxidation experiments were used to observe transient oxidation behavior and to determine isothermal oxidation rates. Coupons were suspended from a sapphire wire in a vertical tube thermogravimetric analyzer (System 3, Cahn Instruments, Cerritos, CA). A small hole was spark machined through coupons to provide a means of hanging from the sapphire wire. The specimen chamber was purged for 2 hours with synthetic air before each run. Specimen temperature was then increased at a rate of 20°C/min to the oxidation temperature and held for 100 hours. Specimen mass change and temperature were continuously recorded.

Following oxidation runs, samples were characterized for scale composition and microstructure using SEM/EDS, XRD, and ESCA (electron spectroscopy for chemical analysis, PHI 5500, Perkin Elmer, Minneapolis, MN) techniques.

III. Results

(1) Microstructures of Oxidation Coupons

Oxidation coupons exhibited essentially three different microstructures: 1) Mo_5Si_3 single phase material with boron in solid solution, 2) Mo_5Si_3 matrix material with additional phases, and 3) Mo_3Si matrix material, as shown in Figure 1. Microstructural data are summarized in Table II.

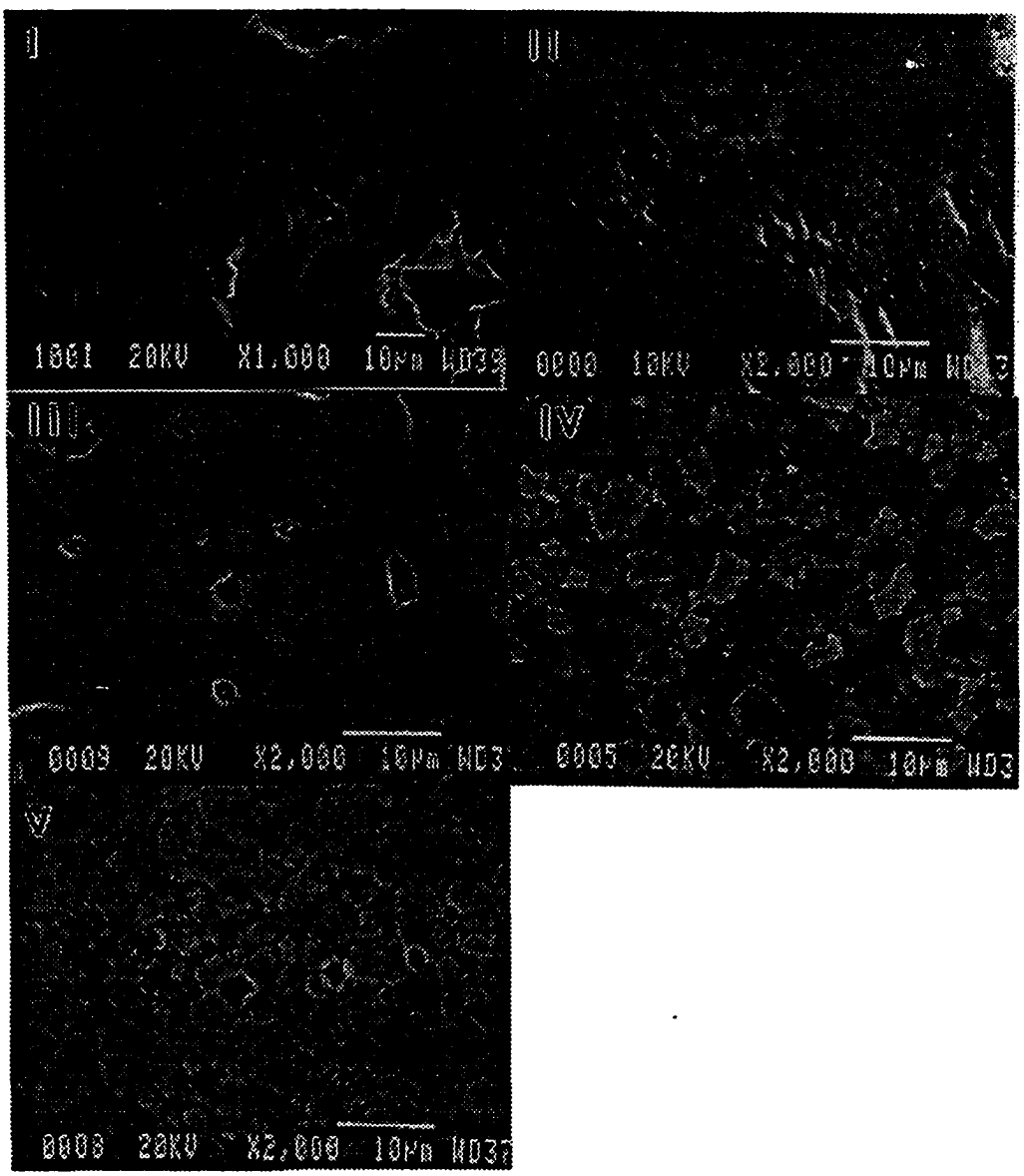

Figure 1. SEM microstructures of specimens prior to oxidation. See Table I for chemical analysis and Table II for phase identification. Top row, 1(a) and a(b). Center row, 1(c) and 1(d). Bottom left, 1(e).

Table II. Phase arrays of oxidation coupons[1]

Comp-osition	Mo_5Si_3	T2	Mo_3Si	$MoSi_2$	MoB	Glass
I	M			X	2	X
II	M					X
III	M			X	2	
IV	M	2	2			
V[2]	2	2	M			

[1]M = matrix phase, 2 = major second phase, x = minor phase. [2]XRD indicates that a small amount of metallic molybdenum is also present.

Compositions I and II have the lowest molybdenum and highest silicon levels but differ substantially in boron content (see Table I), producing different microstructures. Composition I (Figure 1(a)) is a three phase mixture with an Mo_5Si_3 matrix and MoB and $MoSi_2$ as minor intermetallic second phases. A substantial amount of borosilicate glass (dark phase) is found by SEM/EDS as an impurity phase. Some pullout of these glassy areas occurred on metallographic sample preparation. X-ray diffraction analysis indicates that composition II is nearly phase pure Mo_5Si_3, although some MoB second phase is seen in BSE images (Figure 1(b)). Also present is a smaller amount of borosilicate glass phase than found in composition I. Composition III (Figure 1(c)) is an Mo_5Si_3 matrix material similar in microstructure to composition I, but has a lower silicon and higher boron content. It does not contain a glassy impurity phase. Composition IV is a three phase Mo_5Si_3 matrix material with Mo_3Si and a ternary $Mo_5(Si,B)_3$ (T2) phase as dispersed phases (Figure 1(d)). Composition V (Figure 1(e)) is an Mo_3Si matrix material with T2 and Mo_5Si_3 as major second phases.

(2) Formation of Oxide Scale

The development of the oxide scale morphology showed significant differences with changes in specimen composition. Only the SEM/EDS/XRD analysis of scale evolution for two series of coupons are presented here for the sake of brevity. Figure 2 shows the evolution of the oxide scale on Composition V. At 600°C (Figure 2(a)), the scale is composed of three distinct areas, mirroring the makeup of the substrate. Small pockets of borosilicate glass appear as the dark phase in the micrograph, adjacent to areas of almost pure molybdenum oxide. These phases are surrounded by a matrix of mixed molybdenum and silicon oxides. XRD (Figure 3) shows no change in the diffraction pattern on oxidation to 600°C, indicating that the phases formed are not well crystallized. At 633°C, larger MoO_3 crystals begin to form in the scale around the pockets of 'pure' molybdenum oxide. The XRD pattern at 633°C shows peaks due to MoO_3 at 23.33° (110) and 27.34° (021) (Figure 3). The growth of MoO_3 crystals over the scale surface continues at 667°-725°C, as shown in Figures 2(c)-2(e) and Figure 3. At 750°C, MoO_3 begins to evaporate from the surface of the oxidation coupon, as shown by the reduction in number and size of MoO_3 crystals in Figure 2(f). As temperature is increased to 775°C, MoO_3 crystals cover only about one-half of the surface, with the remainder being composed of porous borosilicate glass with a lacy network structure, as seen in Figure 2(g). At 800°C, MoO_3 covers only about 25% of the scale surface with the remainder of the scale appearing as in Figure 2(h). MoO_3 crystals were found to be growing out of the edge of the oxidation coupon at this temperature as seen in Figure 4, indicating that active oxidation of molybdenum is occurring. Upon further heating to 900°C, the crystals growing along the edge of the coupon also volatilize, leaving a ridge of skeletal silica. At 900°C (Figure 2(i)), the scale shows signs of viscous flow, as evidenced by the dulling of edges and closure of submicron scale porosity.

Figure 2. Formation of the oxide scale on composition V at 600°-1075°C. (a)600°C, (b) 633°C, (c) 667°C, (d) 700°C, (e) 725°C, (f) 750°C. Continued next page.

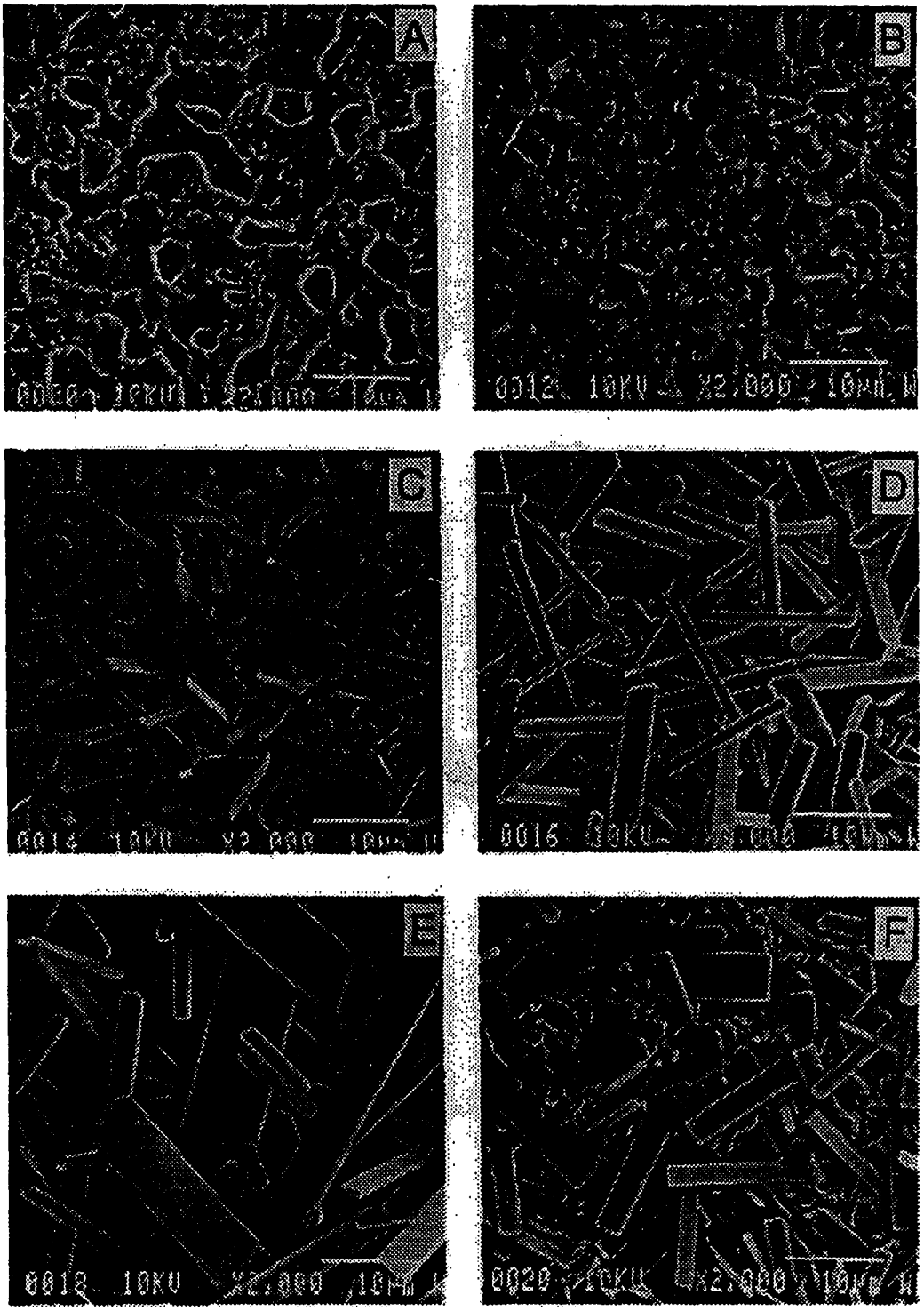
A
B
C
D
E
F

Figure 2. (Continued) Formation of the oxide scale on composition V at (g) 775°C, (h) 800°C, (i) 900°C, (j) 1000°C, (k) 1040°C, (l) 1075°C.

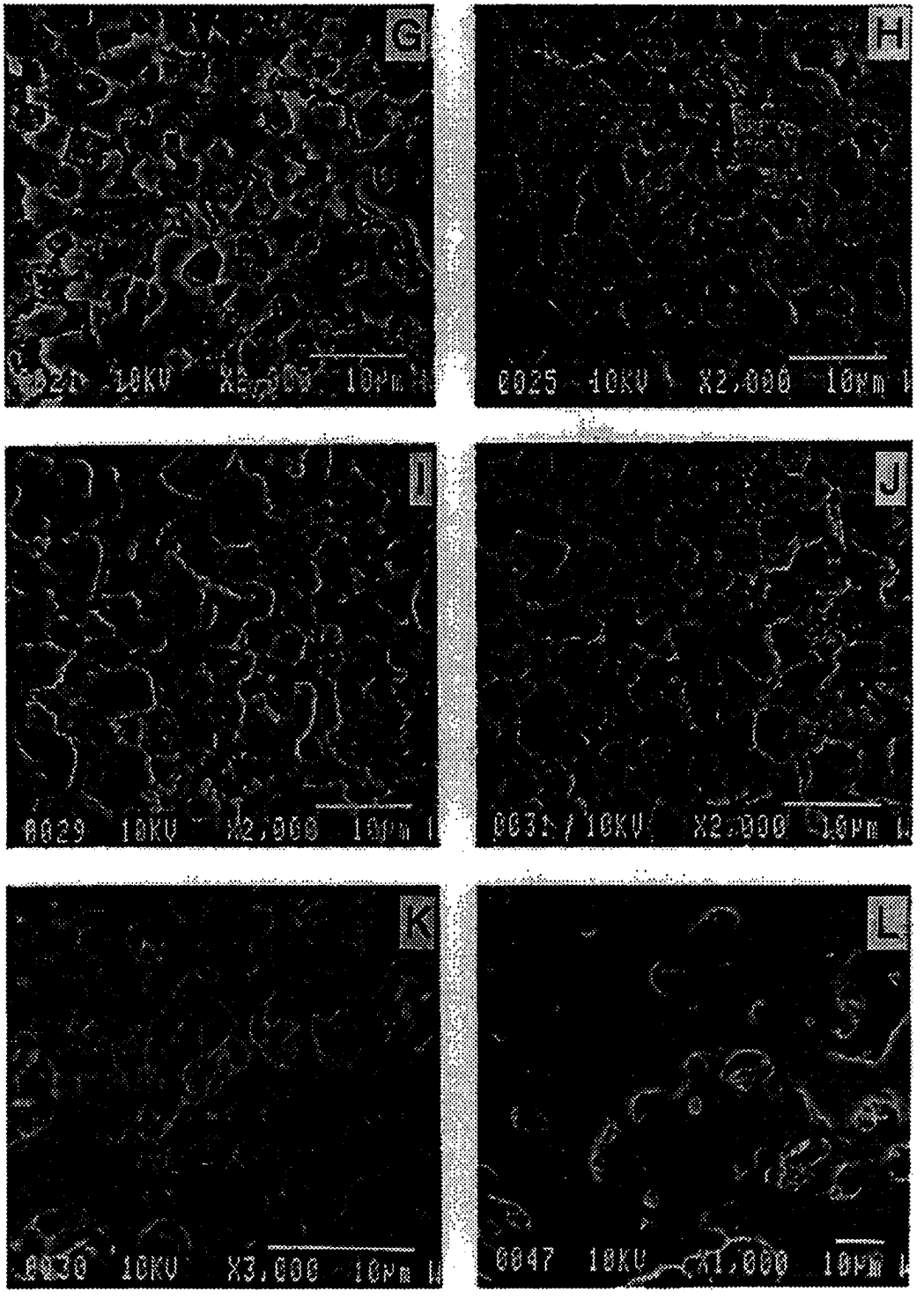
G
H
I
J
K
L

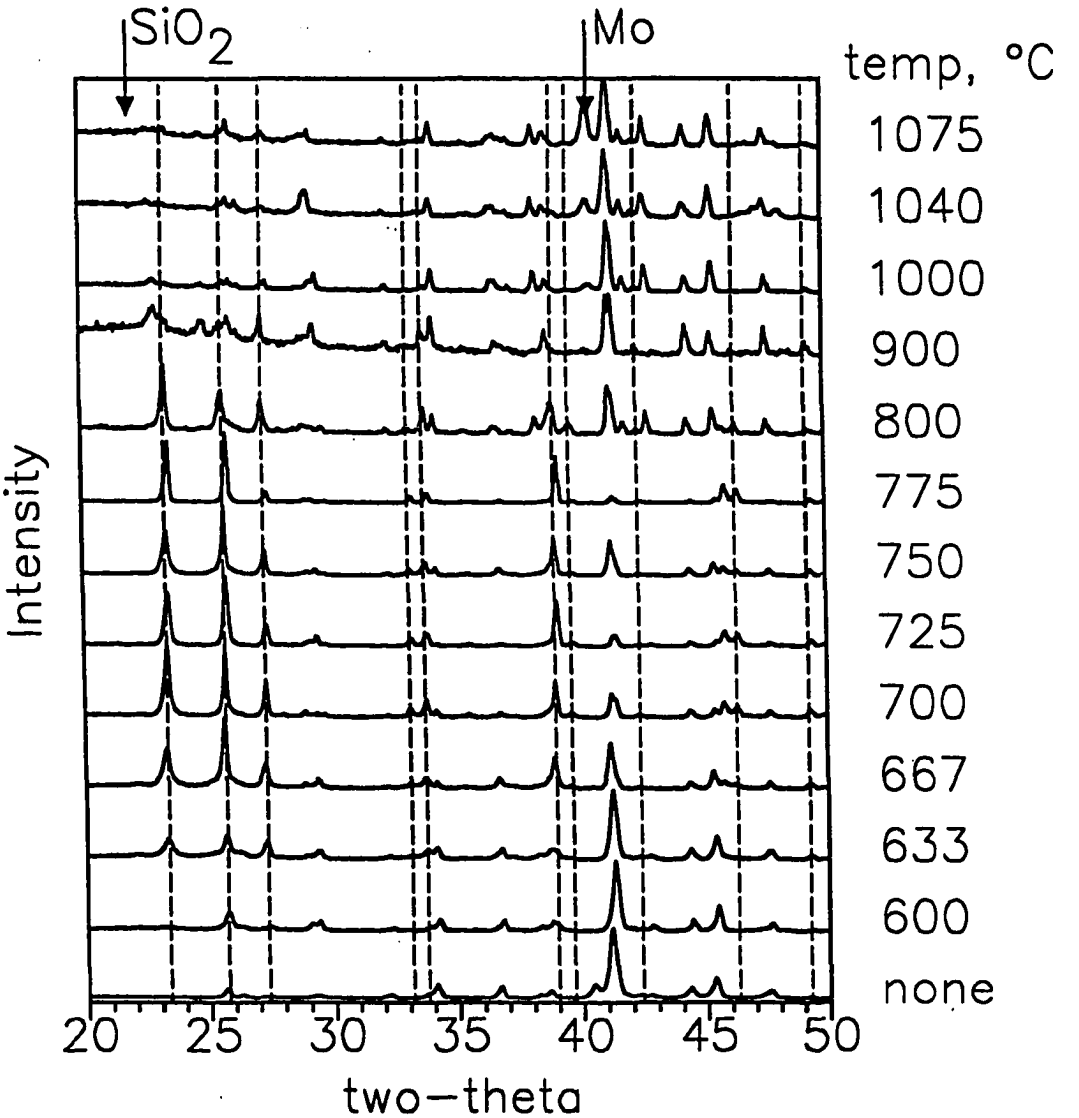

Figure 3. X-ray diffraction patterns of scale on composition V after oxidation at 600°C-1075°C. Dashed lines indicate MoO_3. Also indicated are positions of 100% intensity peaks for molybdenum and cristobalite.

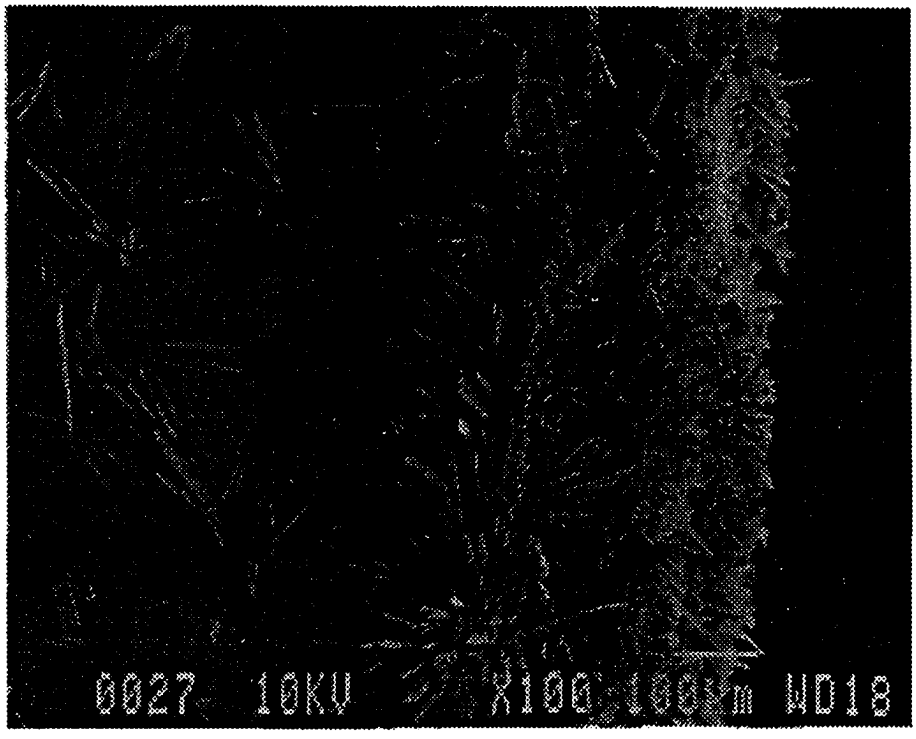

Figure 4. MoO_3 crystals growing from edge of composition V at 800°C indicating active oxidation of molybdenum is occurring

At 1000°C (Figure 2(j)), the scale is similar in appearance to 900°C, showing more than 50% porosity. XRD at 1000°C shows MoO_3 coexisting with metallic molybdenum, indicating that molybdenum is still being actively oxidized over part of the coupon, while being protected from oxidation in other areas. At 1040°C (Figure 2(k)), viscous flow is clearly occuring. XRD shows that the Mo (110) peak at 40.5° continues to grow in intensity relative to the Mo_5Si_3,T2, and Mo_3Si peaks at 41°. This provides evidence that the oxidation interface is becoming silicon depleted while preventing oxidation of molybdenum due to protective scale growth. At 1075°C (Figure 2(l)) the surface of the coupon is completely covered with a uniform glassy scale. No peaks were detected in XRD that would indicate crystallinity of the borosilicate scale.

Figure 5 shows the series of micrographs for the oxidation of composition III as a function of temperature. After heating to 600°C (Figure 5(a)), composition III shows the same 3 microstructural features as composition V, but the relative amounts differ considerably. The scale consists of a larger fraction of borosilicate glass (dark phase) and the mixed MoO_3/SiO_2 matrix, and less of the 'pure' molybdenum rich oxide. The fine structure of the mixed phase is shown at higher magnification in Figure 6. The fine bright spots are MoO_3 in a matrix of borosilicate glass. At 633°C-750°C (Figures 5(b)-5(f)) oxidation proceeds in much the same manner as for composition V. As the temperature increases, large MoO3 crystals form and evaporate. This is confirmed by XRD. After volatilization of MoO_3 at 775°C (Figure 5(g)) the scale on composition III appears considerably different than that of composition V. The scale exhibits bimodal porosity, with a few pores ≈5μm in diameter surrounded by porosity on the order of 0.3 μm in size. XRD patterns of the scale of composition III above 800°C differ significantly from those for composition V, as shown in Figure 7. No MoO_3 is detected by XRD at 900°C, in contrast to composition V. In addition, a metallic molybdenum interlayer does not form on oxidation at

Figure 5. Formation of the oxide scale on composition III at 600°-1075°C. (a)600°C, (b) 633°C, (c) 667°C, (d) 700°C, (e) 725°C, (f) 750°C. (Continued next page).

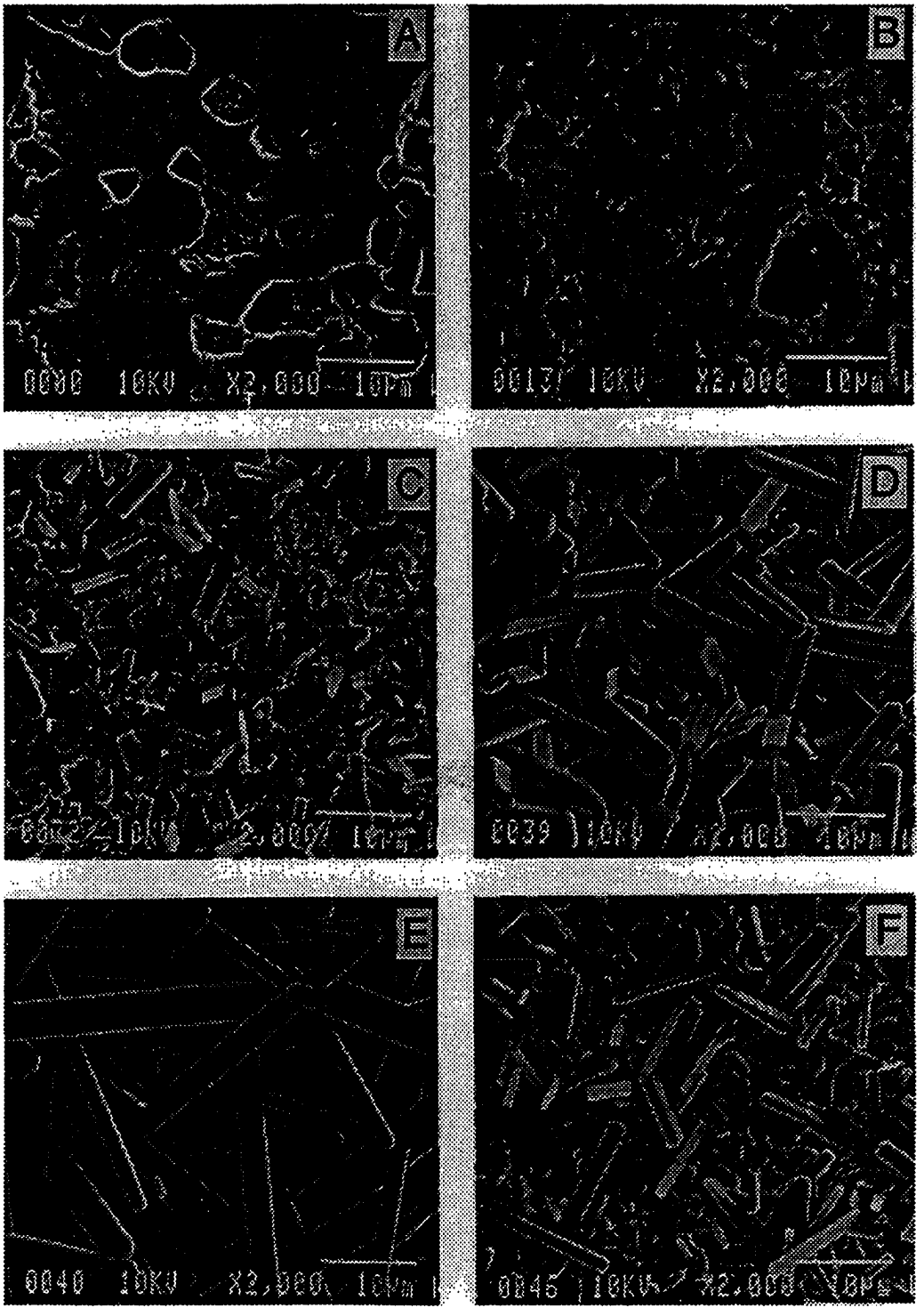
A
B
C
D
E
F

Figure 5. Formation of the oxide scale on composition III at 600°-1075°C (continued) (g) 775°C, (h) 800°C, (i) 900°C, (j) 1000°C, (k) 1040°C, (l) 1075°C.

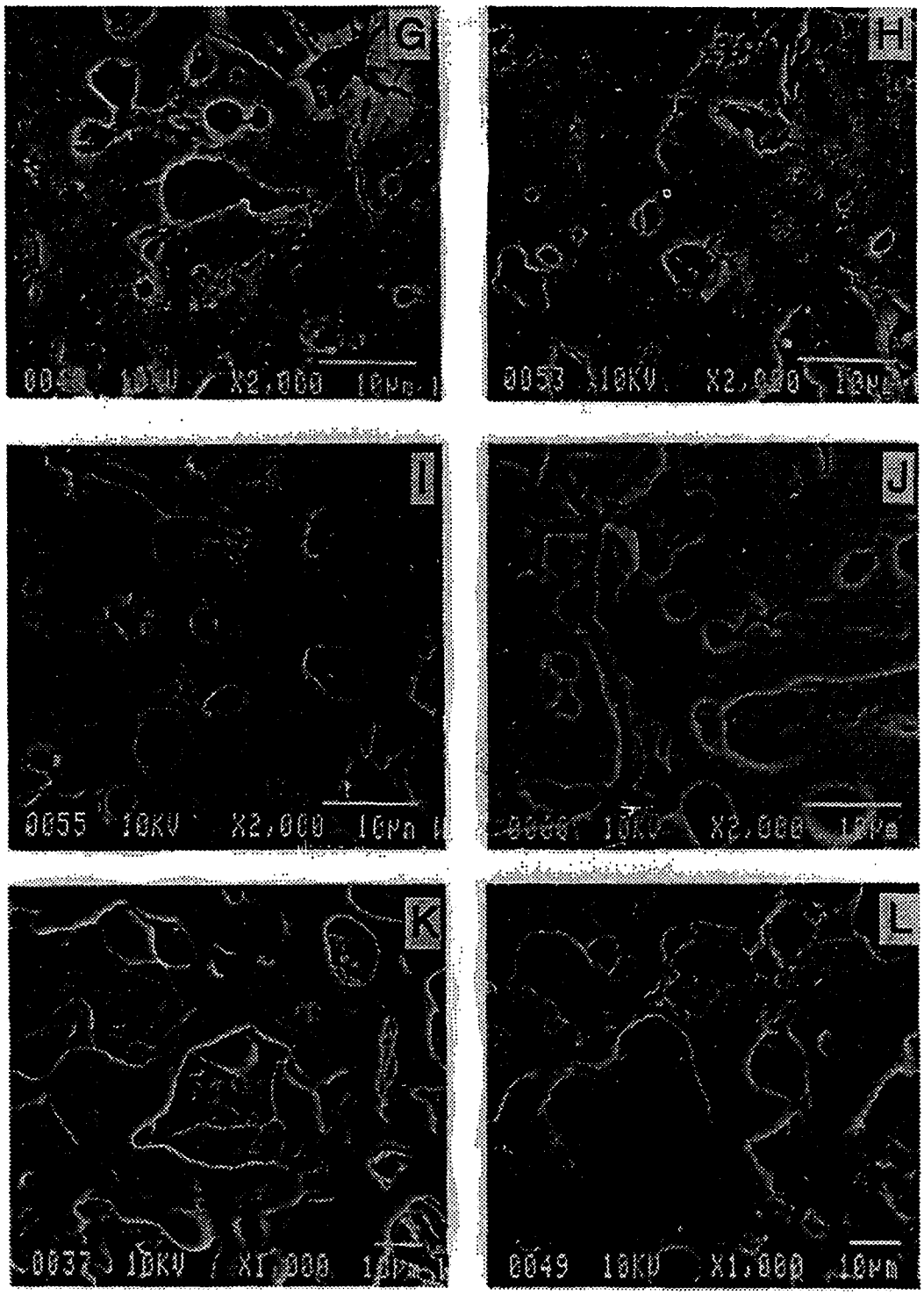
G
0053 10KV X2,000 10µm
H
0053 10KV X2,000 10µm
I
0055 10KV X2,000 10µm
J
10KV X2,000 10µm
K
10KV X1,000 10µm
L
0049 10KV X1,000 10µm

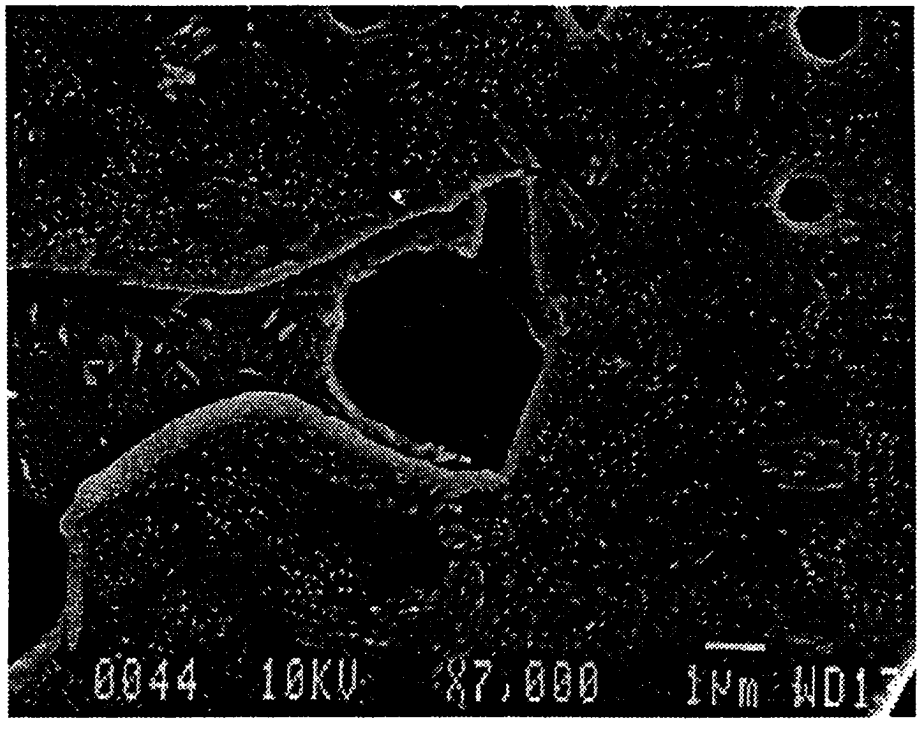

Figure 6. Fine structure of scale 'matrix' phase formed on composition III.

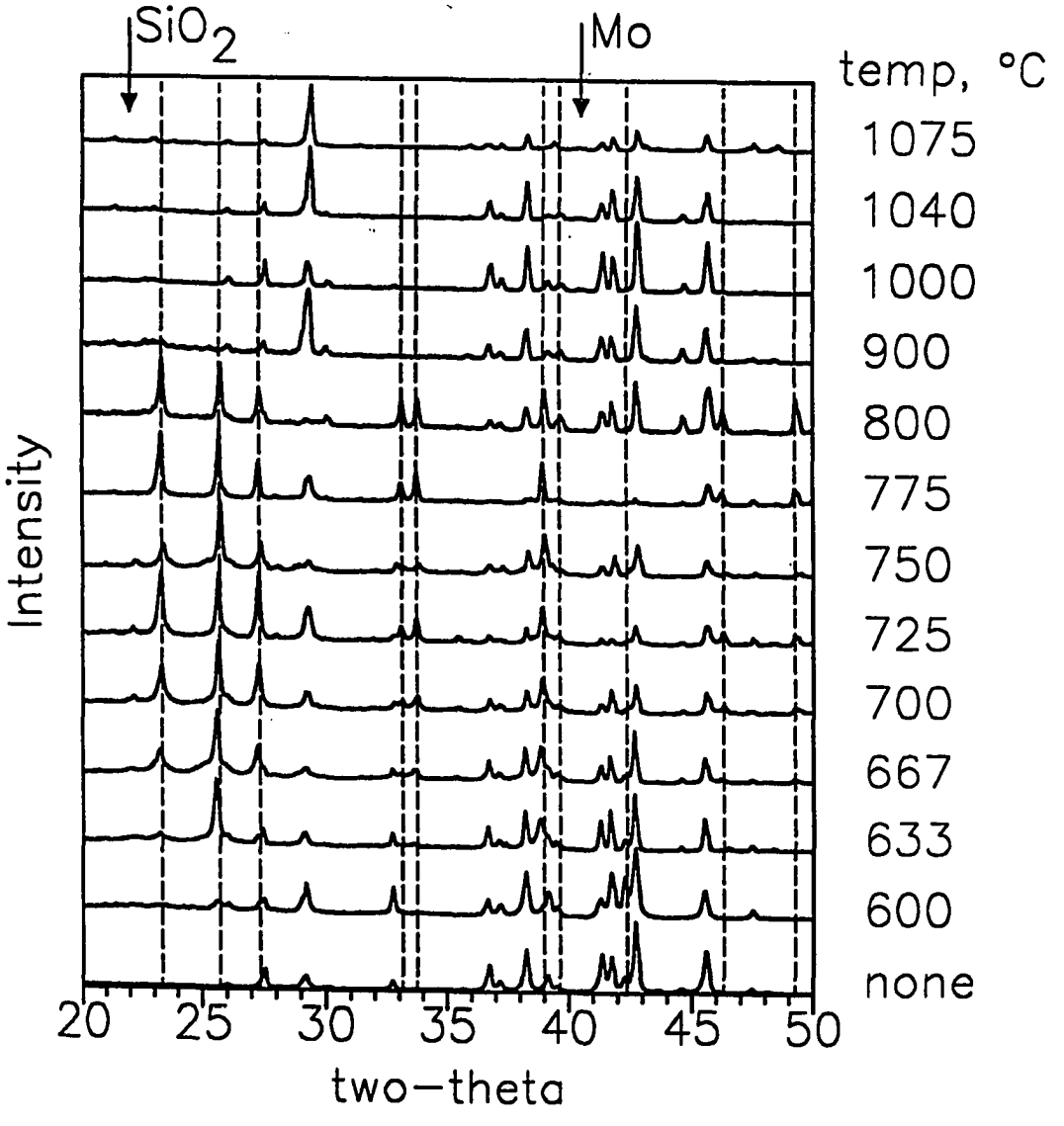

Figure 7. X-ray diffraction patterns of scale on composition III after oxidation at 600°C-1075°C. Dashed lines indicate MoO_3. Also indicated are positions of 100% intensity peaks for molybdenum and cristobalite.

1000°C and above. This indicates that active oxidation of molybdenum is occuring at a slow rate. There is little additional change in scale morphology on oxidation to 1000°C (Figures 5(h)- 5(j)). At 1040°C, (Figure 5(k)) viscous flow is evident. At 1075°C about 33% of the scale surface is covered with a featureless glassy phase, while the remainder appears as in Figure 5(l).

Qualitative chemical analysis of the scales formed on oxidation at 1075°C was conducted using ESCA. The results of this analysis are shown in Figure 8, which shows that the B/Si ratio in the scale increases with the B/Si ratio in the substrate.

(3) Thermogravimetric Analysis

Figure 9 shows plots of the isothermal mass change on oxidation at 1000°C in air. All specimens exhibited an initial mass gain followed by a rapid mass loss starting at 750°C, as shown in Figure 10. After some period of rapid mass loss, oxidation proceeded at some relatively slower, steady state rate (Figure 11). Initial mass loss and steady state oxidation rate are tabulated in Table III. $MoSi_2$ exhibits this same initial oxidation behavior[3] but it is often ignored.[8] As seen in Figures 2-7, the initial mass gain is due to formation of

Table III. Initial mass loss and steady state oxidation rates

Composition	Initial mass loss, mg/cm^2	Steady state[1] rate, $mg/cm^2 \cdot hr$
I	2.77	-3.34×10^{-3}
II	2.15	-3.63×10^{-3}
III	2.79	-1.9×10^{-3}
IV[2]	5.29	-5.0×10^{-5}
V	11.2	$+7.3 \times 10^{-4}$

[1]20-100 hrs. [2]30-100 hrs.

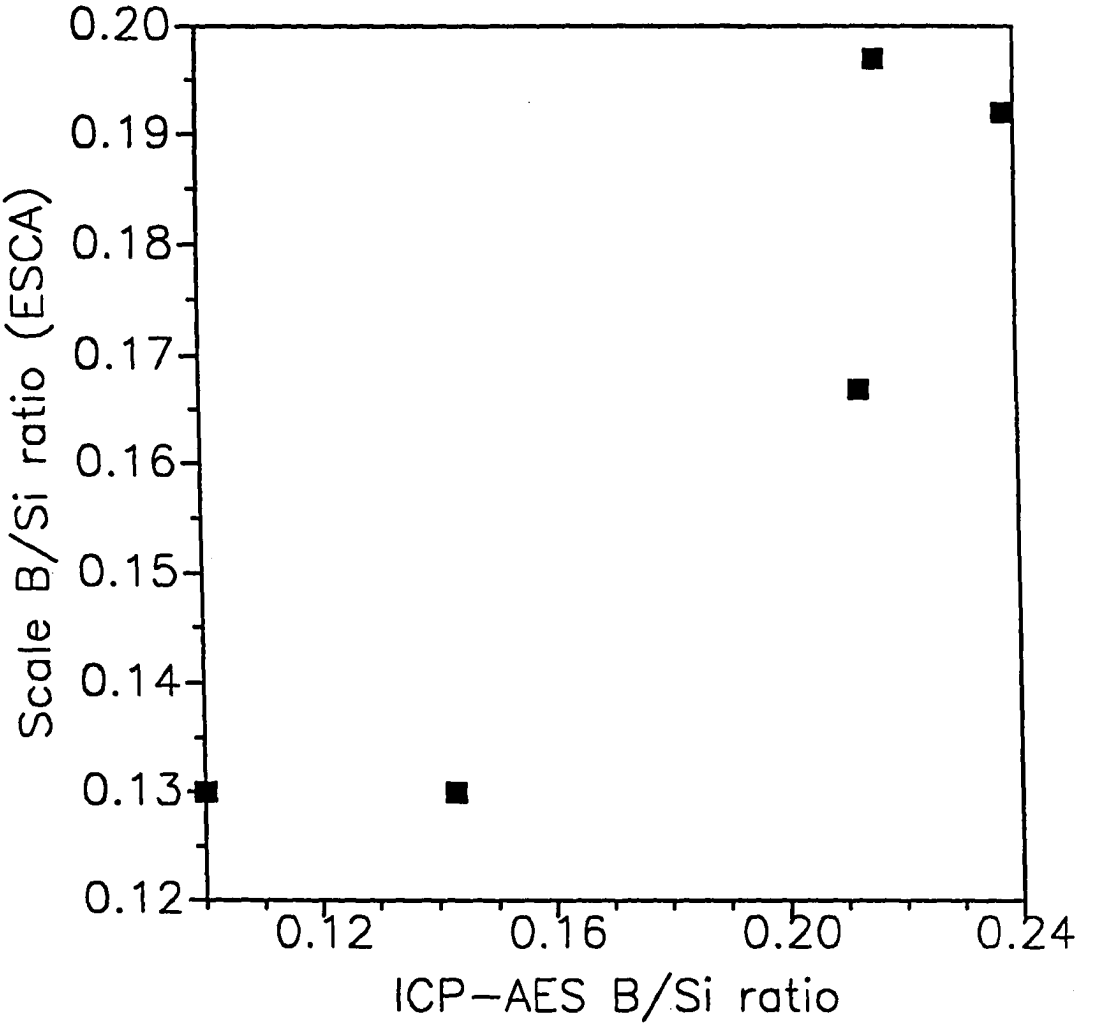

Figure 8. Results of ESCA analysis of scale surface versus ICP-AES analysis of Mo-Si-B compositions.

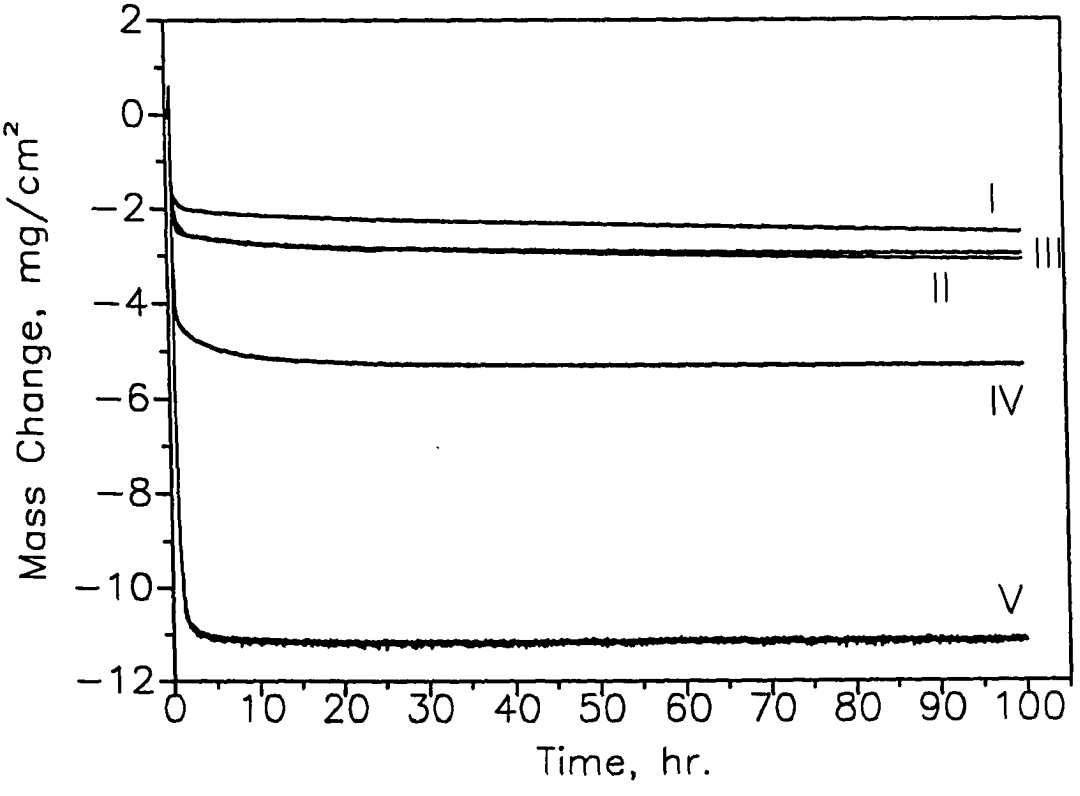

Figure 9. Mass change on oxidation of specimens I-V at 1000°C.

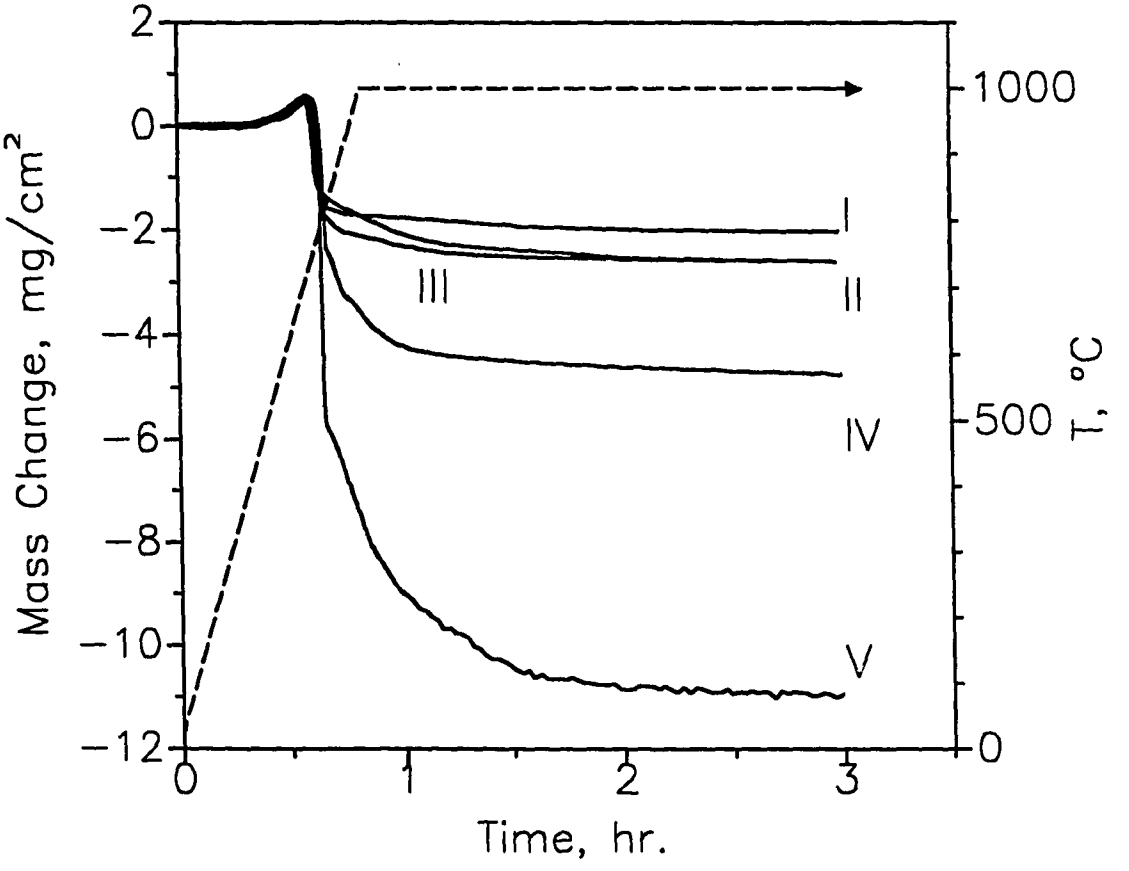

Figure 10. Initial oxidation of compositions I-V showing relative mass loss in the initial transient oxidation regime.

silicon and molybdenum oxides, and the mass loss is due to volatilization of molybdenum oxide. The initial mass loss was calculated by extrapolating a linear regression fit of the steady state portion of the curve back to the intersection of another regression line fit to the initial rapid mass loss period. The mass at the intersection of these lines was taken as the initial mass loss. Mass loss before steady state ranged from 2.8 mg/cm^2 for composition I to 11.2 mg/cm^2 for composition V.

The steady state portion of the oxidation curves for compositions I-V are shown in Figure 11. The curves have been shifted to more clearly show the differences in rates. Oxidation rates shown in Table III are arrived at by assuming a linear model for oxidation kinetics from 20-100 hours. No significance should be given to the choice of a linear model other than to give comparative mass change rate. Compositions I-III exhibit mass loss over the duration of the oxidation tests. Composition IV shows mass loss over the first 32 hours of oxidation followed by a period of almost zero net mass change. Composition V shows a small positive mass change on oxidation.

IV. Discussion

Oxidation of all compositions proceeded in two stages, an initial transient period followed by a region of steady state oxidation. The initial transient period is characterized by a mass gain starting at about 600°C due to oxygen uptake, followed by a rapid mass loss starting at 750°C. In some cases (I and II) transient mass loss is relatively small and essentially complete by 850°C, indicating rapid formation of a protective scale. In other cases (IV and V) transient mass loss continues well into the isothermal temperature regime. After the initial transient oxidation period, the rate of mass loss decreases by several orders of magnitude.

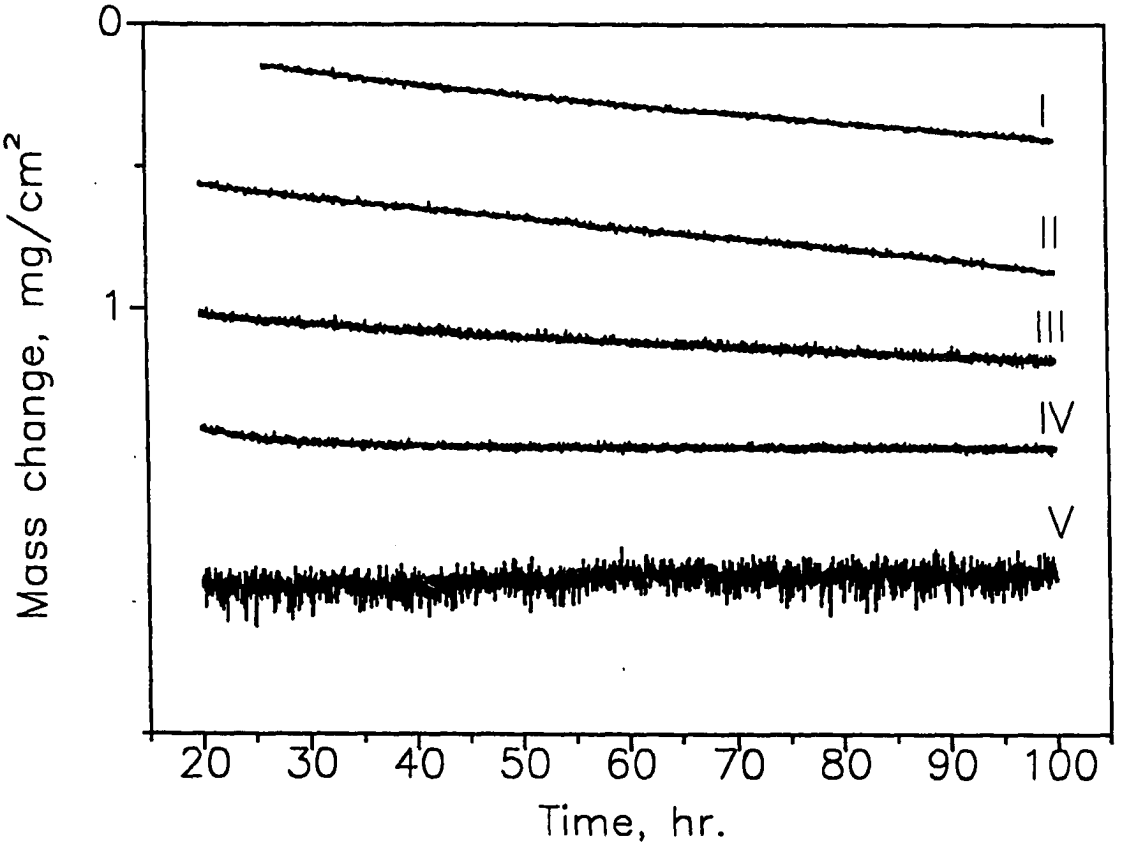

Figure 11. Steady state portion of oxidation curves for compositions I-V. Curves have been shifted for ease in comparing relative slopes.

Important variables to consider during the transient oxidation period are initial scale porosity and pore size, scale formation reaction kinetics, and diffusive or viscous flow. The same basic oxidation mechanisms were operative during scale formation on all compositions tested so that reaction kinetics can be expected to remain relatively constant. The mass loss portion of the transient oxidation regions observed here lasted from one to ten minutes. This short time frame, coupled with the relatively low temperatures involved make it unlikely that atomic scale diffusional processes play a role in the transient regime. It is also evident from Figures 2 and 5 that viscous flow does not occur at temperatures less than 900°C. Elimination of the above possibilities leaves the possibility that initial scale porosity and pore size play a predominant role during the transient oxidation regime. As the scale initially forms, it contains molybdenum oxide (Figure 2(a), 5(a)), which volatilizes to leave a porous scale. The relative volume of molybdenum oxide intially present in the scale determines the fractional porosity of the scale. The degree of segregation of molybdenum oxide determines the pore size, as was confirmed experimentally. Initial mass loss was found to be inversely proportional to the calculated porosity of the scale, as shown in Figure 12. (The calculation of scale porosity will be discussed later in the paper) Compositions with larger fractions of Mo_3Si in the microstructure have a higher degree of molybdenum oxide segregation in the scale at 600°C. These scales form a larger fraction and larger size pores at 800°C than those compositions with little or no Mo_3Si.

Regardless of the magnitude of the initial mass loss, there is a transition to a slower, steady state oxidation regime. The cause of this transition must be the eventual formation of a protective surface layer. The scale that forms may be completely passivating, a continuous protective layer, sealing the substrate surface and allowing only atomic diffusion as a means of oxygen transport to the reaction interface. Alternatively a partially passivating

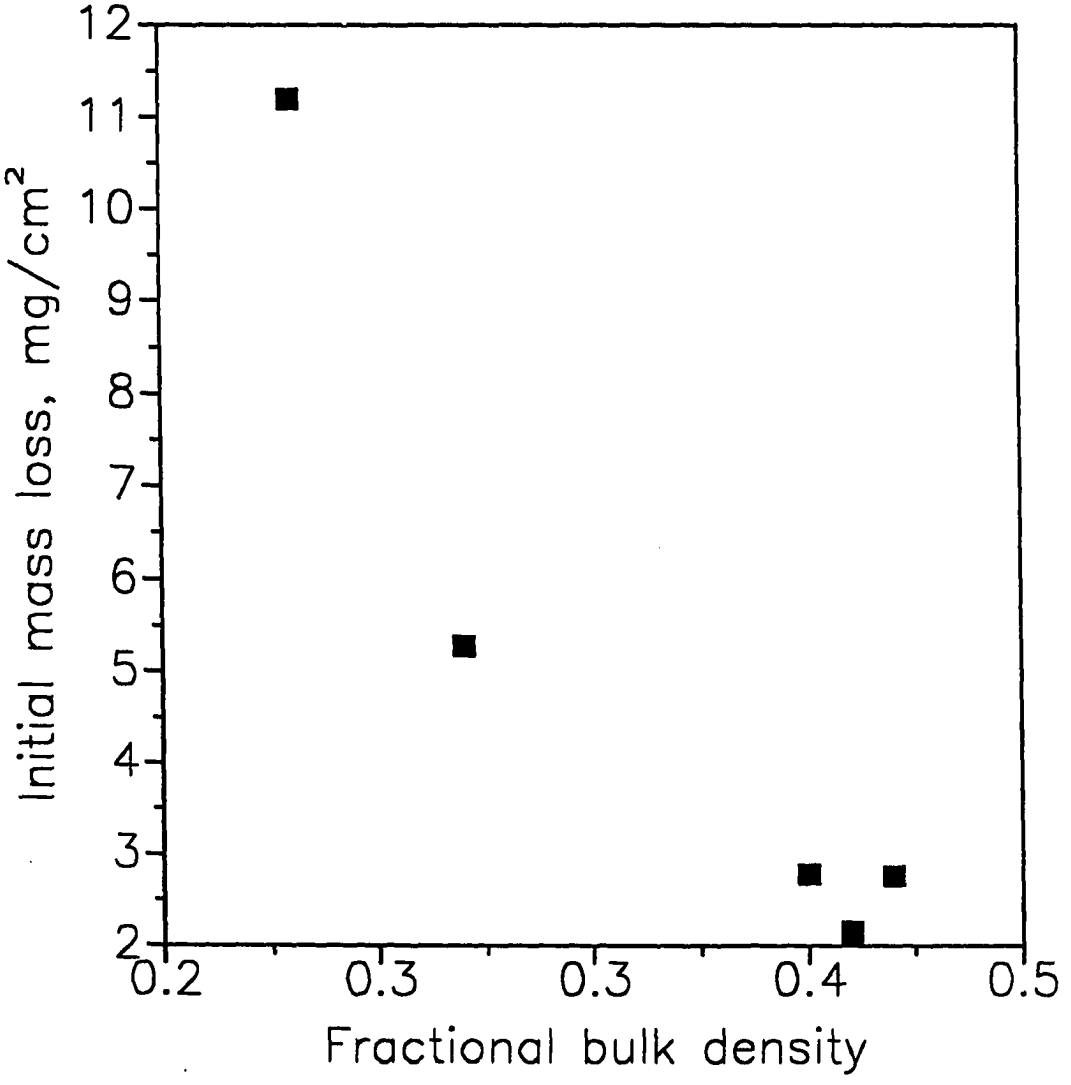

Figure 12. Dependence of initial mass loss during transient oxidation period on initial bulk density of the scale.

microporous scale may form, allowing oxygen and oxidation products to flow through a torturous path (Knudsen diffusion) to the substrate surface, slowing transport and thereby reducing the oxidation rate.

If oxidation is limited by oxygen diffusion and the silicon activity at the oxidation interface is sufficient, oxygen partial pressure will be fixed by Si/SiO_2 equilibrium at a level where molybdenum will not oxidize. The dominant oxidation reaction will be:

$$(1) \quad Mo_5Si_3 + 3\,O_2 \longrightarrow 5Mo + 3SiO_2.$$

Silicon dioxide has a much lower free energy of formation than any molybdenum oxide. A silicon depleted and molybdenum rich interlayer will thus form. It has been shown that SiO_2 can exist in equilibrium with Mo and Mo_5Si_3 so that formation of an Mo_3Si layer is not thermodynamically necessary[9]. Experimental evidence indicates that metallic molybdenum does form before Mo_3Si, so that Equation (1) is valid except at times on the order of 10^3 hours. Equation (1) predicts a net mass gain on oxidation. Composition V exhibited steady state mass gain and formation of a molybdenum interlayer after ramping to 1000°C, providing evidence that oxidation at 1000°C is controlled by oxygen diffusion through a completely passivating scale.

On the other hand, if oxidation is not oxygen diffusion limited and the partial pressure of oxygen at the interface is high enough to oxidize molybdenum, oxidation will proceed according to:

$$(2) \quad 2\,Mo_5Si_3 + 21\,O_2 \longrightarrow 10\,MoO_3\,(\text{volatile}) + 6\,SiO_2$$

Reaction (2) predicts a mass loss due to volatilization of molybdenum oxide (above≈750°C), and that a metalllic molybdenum interlayer will not form. Compositions I-III exhibited slow steady state mass loss without formation of a molybdenum interlayer (as shown by XRD), so that it can be assumed that reaction (2) is the dominant oxidation reaction for compositions I-III at 1000°C. Composition IV was an intermediate case, with a transition from mass loss to zero mass change occurring after 30 hours of oxidation. In this case, Equations (1) and (2) must be competing to yield an essentially net zero mass change.

Important variables to consider when modelling the transition to steady state oxidation are scale porosity, the diffusion rate of silicon to the interface, and the diffusion rate of oxygen through the scale. Diffusion of silicon to the oxidation interface is not expected to be rate limiting. It has been shown[7] that diffusion in Mo_3Si is slower than in Mo_5Si_3, yet an Mo_3Si matrix material (V) exhibited a greater degree of passivation than Mo_5Si_3 matrix materials. Initial scale porosity and pore size will also affect the steady state oxidation rate if viscous flow does not occur to close pores on a reasonable time scale. If viscous flow of the scale to form a coherent passivating layer does occur, however, then the steady state oxidation rate will be controlled by the diffusion rate of oxygen through the passivating layer.

Experimental evidence for the effects of viscous flow is given in Figure 13. Figure 13 shows the dependence of steady state oxidation rate on the viscosity of the scale as calculated from the B/Si ratio of the substrate. The rate of steady state mass loss rate can be seen to increase with increasing scale viscosity.

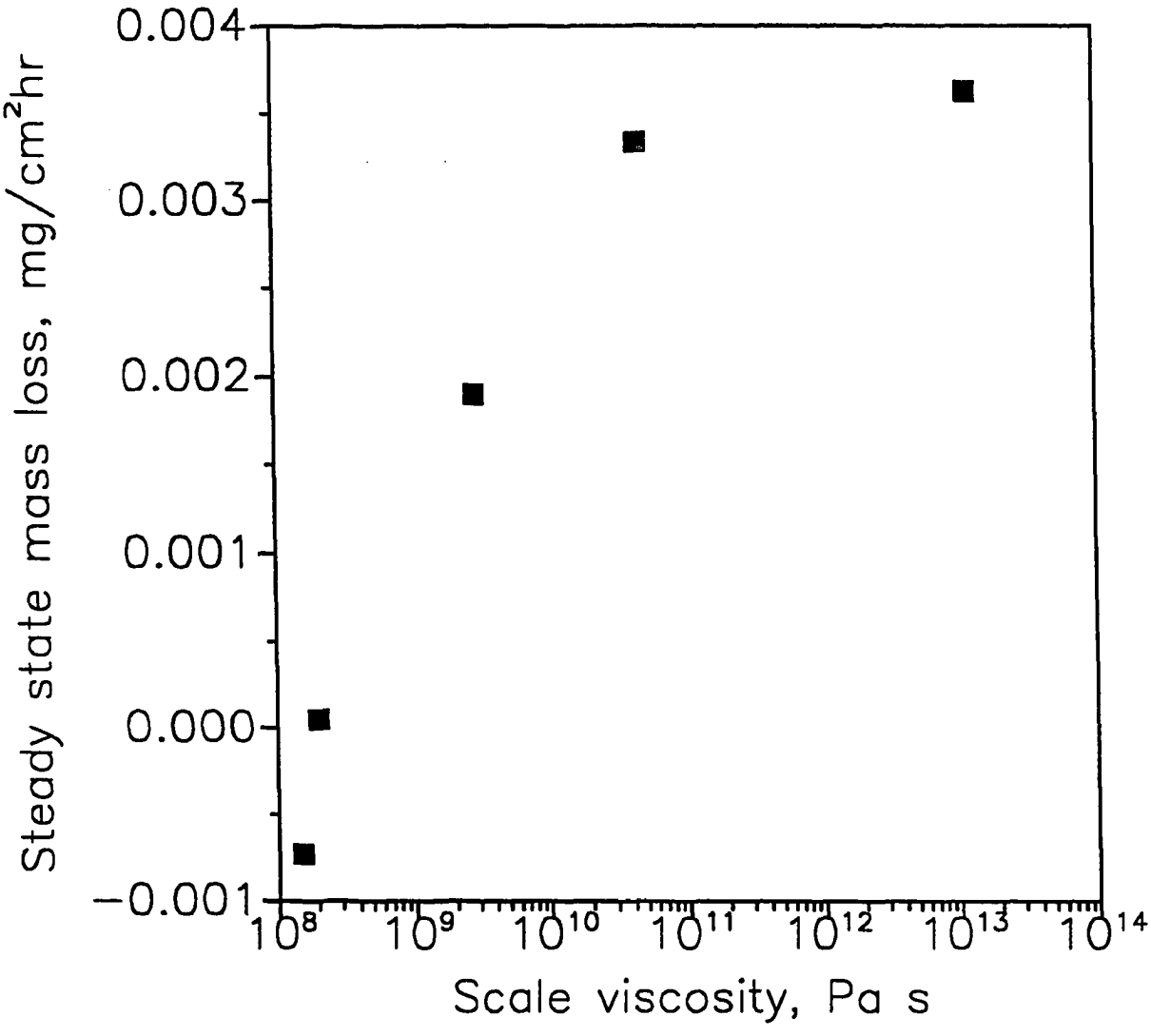

Figure 13. Steady state oxidation rate as a function of scale viscosity for compositions I-V.

(I) Oxidation Model

A model for the transient oxidation behavior of Mo-Si-B intermetallics was formulated based on the above kinetic and microstructural observations. The model assumes that initially the oxidation rate is controlled by the transport of oxygen through a porous scale. The total pore area available for oxygen diffusion and the individual pore size are time dependant and controlled by the viscous flow properties of the scale. A schematic of the salient features of the model are shown in Figure 14 for two extreme cases. Figure 14(a) shows the case where a low viscosity, low density scale with large pores is formed (composition V). Initially, the scale forms at 600°C with pockets of almost pure MoO_3, as shown in Figure 2(a). At 800°C, MoO_3 has volatilized, leaving a network of borosilicate glass with voids on the order of 10 μm in diameter. These voids allow for fast oxygen transport to the interface and active oxidation and volatilization of molybdenum. Oxidation of molybdenum continues until densification of the scale by viscous flow closes the pores and forms a coherent oxide layer. After scale porosity is closed the only path for oxygen transport to the interface is by diffusion through a borosilicate glass and oxidation kinetics become diffusion controlled. Figure 14(b) shows the case for a composition that forms a higher density, high viscosity scale (composition II). Initially the scale forms as a uniform microstructure of finely divided MoO_3 and borosilicate glass. At 800°C, MoO_3 has volatilized, leaving a porous borosilicate glass behind. The pore size is on the order of 0.1 μ m, so that oxygen transport to the interface is controlled by Knudsen diffusion at a much slower rate. Viscous flow does not occur on the time scale of 10^2 hours, so that oxygen diffusion kinetics remain relatively constant, and the oxidation rate remains at some value determined by the oxygen transport rate through a porous scale.

The flow behavior of the scale was modeled by using the theory of Sherer and Garino[10] for viscous sintering on a rigid substrate. The model assumes that the

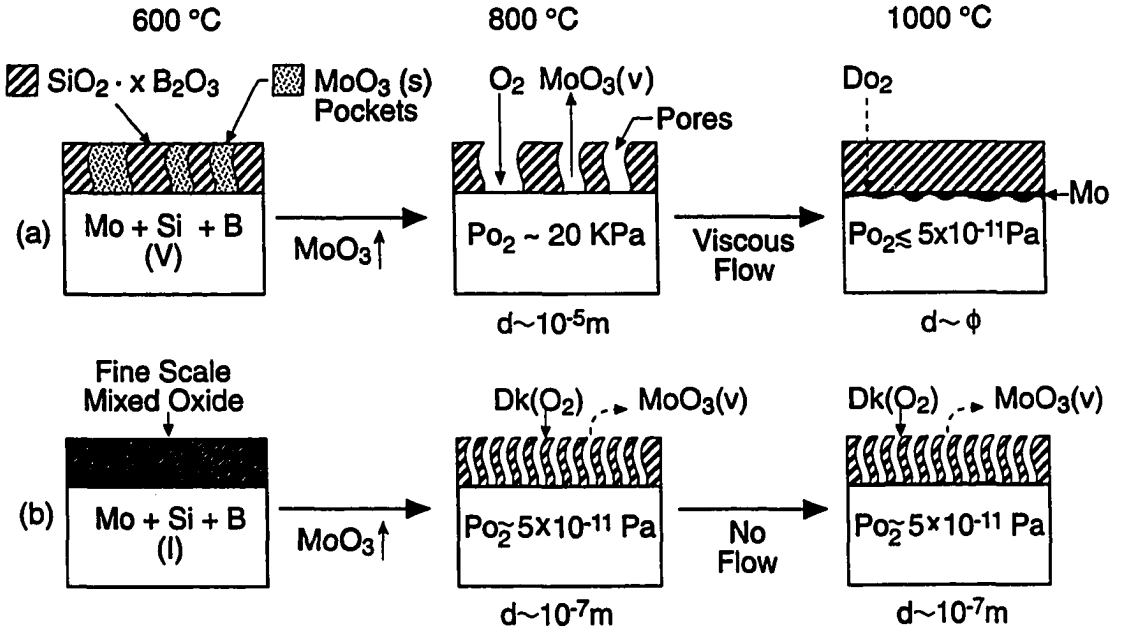

Figure 14. Schematic of oxidation process. (a) case for formation of porous (low density), low viscosity scale, (b) case for formation of lower porosity, high viscosity scale.

microstructure of a porous body can be described by a network of cylindrical rods resembling a scaffold. The rods have radius a and length l. The parameters a and l can be related to particles size and pore size of the body being sintered. Changes in a and l are driven by the lowering of system energy due to reduction in surface energy. This system energy loss is partially balanced by energy gain due to viscous flow. The density of the body can be calculated as a function of a/l using the relation:

(3) $\rho/\rho_T = 3\pi(a/l)^2[1-1.2(a/l)]$

where ρ/ρ_T fractional density. The quantity a/l as a function of time is determined by:

(4) $K(t-t_f) = -1.493 + 2.6727f(y/\alpha_2) - 4.4357f(y/\alpha_1)$

where

(5) $y = \left(\frac{3\pi}{a/l} - 8\sqrt{2}\right)^{\frac{1}{3}}$,

α_1, α_2 are constants, and f is a function given by Sherer. $K(t-t_f)$ is dimensionless time, where t is the real sintering time, and t_f is the time to reach theoretical density. K is given by:

(6) $K= (\gamma/\eta l_o)(\rho_T/\rho_o)^{1/3}$

where γ is surface energy, η is viscosity, l_o is the initial value of l, and ρ_o and ρ_T are the initial and theoretical densities of the glass layer being sintered. For calculations, surface energy (γ) was assumed constant at 0.28 J/m^2. Viscosity (η) was estimated from the B/Si ratio in the bulk compositions using an empirical equation given by Yan[11], modified slightly to give a better fit to viscosity data in the composition and temperature range of interest. The parameter l_o was estimated from the initial pore size of the scale as observed by SEM after oxidation at 1000°C. It was assumed for the estimation of l_o that the relations given by Sherer[12]:

$$(7)\ \rho_o/\rho_T = 3\pi(a/l_o)^2 - 8\sqrt{2}\,(a/l_o)^3$$

for estimating a/l_o as a function of density and:

$$(8)\ \pi d_2/4 \approx (l_o-2a)^2$$

for estimating l_o as a function of pore diameter (d) held initially for this system. Pore diameter (d) for use in equation (8) was estimated from micrographs after oxidation at 1000°C. The initial density of the scale (ρ_o) was calculated by assuming that molybdenum, silicon, and boron were oxidized in the molar ratios present in the substrate to crystalline MoO_3 and SiO_2·B_2O_3 glass. The relative density of the scale after volatilization of MoO_3 was then calculated as:

$$(9)\ \rho_o/\rho_T = (X_{Si}+\tfrac{1}{2}X_B)(V_{SiO_2\cdot B_2O_3})/((X_{Mo}V_{MoO_3} + (X_{Si}+\tfrac{1}{2}X_B)(V_{SiO_2\cdot B_2O_3}))$$

where X_{Mo}, X_{Si}, and X_B are the atomic fractions of the elements in the substrate and V_{MoO_3} and $V_{SiO_2 \cdot B_2O_3}$ are molar volumes. The theoretical density ρ_T of the borosilicate glass forming the scale (after MoO_3 volatilization) was calculated by least squares fitting of a linear equation to density data for borosilicate glass found in the literature.[13] The resullting equation relating borosilicate glass density to mole fraction B_2O_3 is:

$$(10)\quad \rho_T = 2.2 - 0.43\, X_{B_2O_3}$$

The correlation coefficient (R^2) of this equation to the data is 0.987.

Values of t_f for use in equation (4) were estimated by using sintering data for a 6 wt% borosilicate glass.[11] The time (t_{94}) to reach 94.2% theoretical density was first estimated as a function of viscosity. This relation was found to be:

$$(11)\quad \log_{10}(t_{94}) = -10.898 + 1.075\log_{10}(\eta_p)$$

where η_p is glass viscosity in Poise and t_{94} is in hours. It should be noted that t_{94} is a function of l_o and ρ_o as well as η, however literature data was too limited to allow a fit to all three parameters. The parameter t_f was calculated from t_{94} through the relation:

$$(12)\quad K(t_f - t_{94}) = 0.4827$$

from the Mackenzie-Shuttleworth[14,10] theory for viscous sintering of bodies with isolated pores. Parameters calculated for the model are given in Table IV.

Diffusion of oxygen through the initially porous scale to the oxidation interface was

Table IV. Parameters for oxidation model at 1000°C.

Composition	ρ_T, g/cm^3	d, μm	ρ_o/ρ_T	η, Pa·s	t_{94}, hr.
I	2.13	0.5	0.42	4.5×10^{10}	42.0
II	2.15	0.5	0.41	1.2×10^{13}	1.7×10^{6}
III	2.12	1.0	0.40	2.9×10^{9}	2.24
IV	2.10	10.0	0.32	2.0×10^{8}	0.13
V	2.08	10.0	0.28	1.5×10^{8}	0.09

assumed to be controlled by Knudsen diffusion. The governing equation for the effective diffusivity (D_e) is given by[15]:

$$(13)\quad D_e = \left(\frac{4r}{3}\right)\left(\frac{\varepsilon}{\tau}\right)\sqrt{\frac{2RT}{\pi M}}$$

where r is capillary radius, ε is fractional porosity ($1-\rho/\rho_T$), τ is a tortuosity factor, R is the gas constant, T is absolute temperature, and M is the molecular weight of the diffusing gas, oxygen in this case. The tortuosity (τ) was taken as constant at 1. The capillary radius (r) was assumed to be equal to one half the pore diameter (d). (It should be noted that this equation strictly applies only when the pore size is smaller than the mean free path of the diffusing gas, however, for simplification of the model Knudsen diffusion was assumed to operate over the entire pore size regime) Pore diameter as a function of density was calculated by assuming that the number of pores per unit area (N) remained constant and that the diameter of each pore decreased at the same rate:

$$(14)\quad d = 2\sqrt{\frac{\varepsilon}{N\pi}}$$

The net result of the model is that oxidation rate is initially controlled by pore size and pore volume of the scale as it forms. As the scale densifies at the oxidation temperature, pore area and pore size decrease, thus decreasing the flux of oxygen. When the scale is 94% dense, Sherer's model predicts that only closed porosity remains. At this density a transition from Knudsen diffusion to atomic diffusion will occur. The of atomic diffusion regime was not considered by this model. The derivation of theoretical minimum rates for diffusion controlled oxidation processes can be found elsewhere.[16]

(2) Comparison of Model Predictions with Experimental Results

Predictions of the oxidation model are shown in Figure 15, which plots relative diffusion rate of oxygen through the scale as a function of time for each of the compositions oxidized in this study. The arrows in Figure 15 indicate the time at which the scale reaches 94% density and atomic diffusion becomes the predominant transport mechanism. It can be seen by comparison of Figure 15 with Table III and Figures 8-10 that the predictions of the model are qualitatively correct. The fastest steady state oxidation rates are predicted for compositions I and II, due to lack of scale porosity closure caused by slow viscous flow kinetics. In addition, the model predicts that composition II should have faster oxidation kinetics than composition I. Compositions IV and V are shown to have rapid initial oxidation kinetics due to the large amount and size of the initial porosity present. These predictions are confirmed by experimental observation, as shown in Figure 10. The rate quickly decreases, however, due to viscous sintering of the scale to close porosity, as confirmed by data shown in Figure 11. After closure of porosity compositionV exhibits parabolic kinetics and mass gain. Composition III is shown to have intermediate behavior, with initial mass loss similar to I and II and steady state oxidation kinetics intermediate to II and IV.

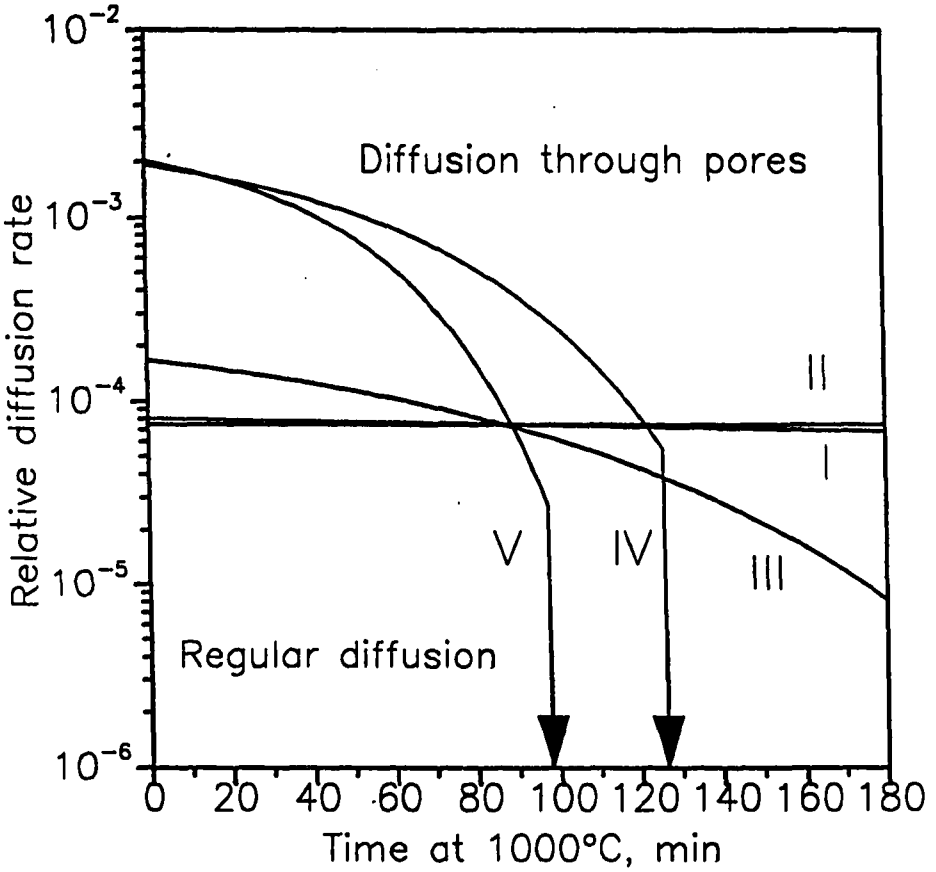

Figure 15. Predictions of oxidation model for compositions I-V.

We have previously[2] studied the oxidation kinetics as a function of temperature for a composition similar to III, and found that oxidation changes from mass loss to mass gain behavior near 1075°C. Above 1075°C for times of 20-300 hours, oxidation kinetics appear to be controlled by diffusion of oxygen through the scale. Given sufficient time and/or temperature, all compositions tested should develop a fully dense scale. If this occurs oxidation kinetics will be controlled by the rate of oxygen diffusion through the scale. The rate of oxygen diffusion through borosilicate glass increases with boron content.[17] It is expected then, that the rate of oxidation in the oxygen diffusion controlled regime will scale will increase with the boron content in the intermetallic.

V. Summary

The oxidation behavior of molybdenum rich Mo-Si-B compositions was studied using x-ray diffraction, thermogravimetric analysis, and microscopic observation of the scale at different stages of growth. It was found that in compositions with high molybdenum content (such as V) the scale at 600°C is composed of islands of nearly pure molybdenum oxide in a matrix of mixed Mo-Si oxide. Small pockets of borosilicate glass also form. As temperature is increased, well defined MoO_3 crystals grow out of the scale. MoO_3 begins to volatilize at 750°C. At 800°C, the scale surface is a porous borosilicate glass. At 900°C, the scale shows signs of viscous deformation. Mass loss data indicates that rapid oxidation of molybdenum is occurring up to 1000°C for short times. The isothermal oxidation rate at 1000°C is small and positive, and a molybdenum interlayer forms, indicating that the scale is acting as an effective passivating layer. SEM/EDS and XRD data confirm that the scale is a coherent layer of borosilicate glass.

Compositions with a higher relative fraction of boron and silicon exhibit initial formation of a scale at 600°C with a larger fraction of borosilicate glass and finely mixed oxide and a smaller fraction of 'pure' molybdenum oxide. The change from the initial transient oxidation period to a region of slower mass loss occurs at about 800°C, indicating that the transient mass loss is due to volatilization of MoO_3 originally formed in the scale at 600°C, and that rapid active oxidation of molybdenum is not occuring at T>800°C.

After the transient oxidation period, a slower 'steady state' regime was reached. The isothermal oxidation rate at 1000°C was found to vary inversely with scale viscosity. Phase array of the substrate coupon did not have an effect on long term oxidation behavior. Of the binary silicides, Mo_3Si has the poorest oxidation resistance. Composition V, however, which has the largest fraction of Mo_3Si had the lowest steady state oxidation rate. This indicates that flow of the scale to form a coherent passivating layer is more important than the diffusion rate of silicon to the interface in determining oxidation behavior at 1000°C.

A model for the transient oxidation behavior of Mo-Si-B intermetallics was formulated based on the initial porosity and sintering kinetics of the scale. The model assumes that initially the oxidation rate is controlled by the transport of oxygen through a porous scale layer. Total pore area and pore size are time dependent and controlled by the viscous flow properties of the scale. The model predictions of the oxidation behavior are in good agreement with experimental results.

Acknowledgment

The authors would like to thank Jim Anderegg for ESCA measurements and Andrew Thom for valuable discussions. Ames Laboratory is operated for the U.S. Department of Energy by Iowa State University under contract number W-7405-ENG-82. This research was supported by the Office of Basic Energy Science, Materials Science Division.

References

[1]D.L. Anton, D.M. Shah, "High Temperature Properties of Refractory Intermetallics," *Mat. Res. Soc. Symp. Proc.*, **213** 733-39, Materials Research Society, Pittsburgh (1991).

[2]M.K. Meyer, M. Akinc, " Oxidation behavior of Boron Modified Mo_5Si_3 at 800°-1200°C," Submitted to *J. Am. Ceram. Soc.* (1994).

[3] E. Fitzer, "Oxidation of Molybdenum Disilicide," pp. 19-41 in Ceramic Transactions vol. 10: Corrosive and Erosive Degradation of Ceramics, R.B. Tressler and M. McNallan, eds., American Ceramic Society, Westerville, OH (1989).

[4]J.B. Berkowitz-Mattuck, R.R. Dils, "High-Temperature Oxidation; II. Molybdenum Silicides," *J. Electrochem. Soc.*, **112** [6] 583-89 (1965).

[5]S.-L. Zhang, R. Ghez, F.M. d'Heurle, "A Mathematical Model for Silicide Oxidation," *J. Electrochem. Soc.* **137** [2] (1990).

[6]F.M. D'Heurle, A. Crs, R.D. Framptom, E.A. Irene," Thermal Oxidation of Silicides on Silicon," *Phil. Mag.* **B55** [2] 291-308 (1987).

[7]R.W. Bartlett, J.W. McCamont, P.R. Gage, "Structure and Chemistry of Oxide Films Thermally Grown on Molybdenum Silicides," *J. Am. Ceram. Soc.*, **48** [11] 551-58 (1965).

[8]D.A. Berztiss, R.R. Cerchiara, E.A. Gulbransen, F.S. Petit, G.H. Meier, "Oxidation of $MoSi_2$ and Comparison with other Silicide Materials," *Mat. Sci. Eng.* **A155** 165-81 (1992).

[9]R. Beyers, "Thermodynamic Considerations in Refractory Metal-Silicon-Oxygen Systems," *J. Appl. Phys.*, **56** [1] 147-52 (1984).

[10]G.W. Scherer, T. Garino, "Viscous Sintering on a Rigid Substrate," *J. Am. Ceram. Soc.*, **68** [4] 216-20 (1985).

[11]M.F. Yan, J.B.MacChesney, S.R. Nagel, W.W. Rhodes, "Sintering of Optical Wave-Guide Glasses," *J. Mater. Sci.* **15** 1371-78 (1980).

[12]G.W. Sherer, "Sintering of Low Density Glasses: I, Theory," *J. Am. Ceram. Soc.*, **60** [5-6] 236-39 (1977).

[13]R. Jabra, J. Phalippou, J. Zarzycki, "Synthese et caracterisation des verres du systeme SiO_2-B_2O_3 obtenus par pressage a chaud de gels," *Rev.Chim. Min.* **16** [4] 245-66 (1979).

[14]J.K. Mackenzie, R. Shuttleworth, "A Phenomenological Theory of Sintering," *Proc. Phys. Soc. (Lond.)* **B62** [12] 833-52 (1949).

[15]D.G.Huizenga, D.M. Smith ,"Knudsen Diffusion in Random Assemblages of Uniform Spheres," *AIChE Journ.* **32** [1] 1-6 (1986).

[16]O. Kubaschewki, B.E. Hopkins, Oxidation of Metals and Alloys, Academic Press, New York (1962).

[17] J. Schlichting, "Oxygen Transport through Glass Layers Formed by A Gel Process," *J. Non-Crystall. Solids*, **63** 173-81 (1984).

CHAPTER 4: COMPRESSIVE CREEP BEHAVIOR OF SINTERED Mo_5Si_3 WITH THE ADDITION OF BORON

A manuscript to be submitted for publication in the *Journal of the American Ceramic Society*

Mitchell K. Meyer[1], Matthew J. Kramer, and Mufit Akinc[1]

Ames Laboratory and [1]Department of Materials Science and Engineering

Abstract

Mo_5Si_3 shows high creep resistance but poor high temperature oxidation resistance. Previous work has shown that the oxidation rate of Mo_5Si_3 can be decreased with the addition of boron. By adding 1.3 weight percent boron to a silicon deficient composition, a three phase microstructure composed of Mo_5Si_3 (T1), Mo_3Si, and a ternary $Mo_5(Si,B)_3$ (T2) phase was synthesized. The compressive creep rate of this composition was evaluated at 1240°-1320°C and 120-180 MPa. The average creep stress exponent and activation energy for the three phase material were found to be $n=4.3$ and $E_a=396$ kJ/mol. TEM analysis of the crept microstructure of the boron modified material reveals no evidence for dislocation activity in T1. Only basal slip was observed in the T2 phase. $\{001\}<100>$ dislocations and polygonal subgrain structures were observed in Mo_3Si. Mo_3Si and T2 were found to stop cracks that nucleate in the T1 phase during creep.

I. Introduction

Of the three compounds in the molybdenum-silicon phase equilibria, only $MoSi_2$ has been well characterized; it is well known for excellent oxidation resistance in the 800°C - 1700°C range. Mechanical properties[1,2,3,4] and oxidation resistance[5,6,7,8,9,10] of molybdenum disilicide ($MoSi_2$) have been investigated over the last several decades.[11] Although $MoSi_2$ has excellent oxidation resistance at temperatures up to 1700°C in air, it has a high creep rate above 1100°C, making it unsuitable as a high temperature load bearing material in the monolithic state.[12,13]

In the absence of impurities Mo_5Si_3 has a body centered tetragonal crystal structure of space group I4/mcm (No. 140[14]). The unit cell is large and complex, composed of four Mo_5Si_3 formula units. Mo_5Si_3 is the most refractory compound in the Mo-Si binary diagram with a melting point of 2180°C, and has a homegeneity range of 2.5 atomic percent silicon.[15] The ternary Mo-Si-C phase, which has a carbon stabilized hexagonal structure, was reported in 1954 by Nowotny, et al.[16] The stabilization of the hexagonal phase by carbon led to research into other light element additions, and generation of an isothermal (1600°C) Mo-Si-B ternary phase diagram.[17]

Mechanical properties data on Mo_5Si_3 is sparse. The compressive creep rate and some mechanical properties of Mo_5Si_3 prepared by arc casting were recently reported.[18] A creep rate of 4×10^{-8} s^{-1} was measured at 1200°C and 69 MPa. In comparison, the creep rate of $MoSi_2$ in the same paper was reported as 2.1×10^{-7} sec^{-1}, nearly an order of magnitude higher. No quantitative study of creep mechanisms in Mo_5Si_3 has been performed. Likewise, no data is available for Mo_3Si or the ternary T2 ($Mo_5(Si,B)_3$) phase, the two other phases present in the creep specimens tested in this work.

Experimental data from several studies[18,19,20] indicates that Mo_5Si_3 has poor high temperature oxidation resistance. Since Mo_5Si_3 exhibits high creep resistance, it is desirable

to improve oxidation resistance while retaining creep resistance. By adding 0.8 to 1.9 wt% boron, the oxidation resistance of Mo_5Si_3 is improved to a level near that of $MoSi_2$ in the temperature range of 800°-1300°C.[21] Since there is only a small solid solubility of boron in Mo-Si compounds, a two or three phase microstructure forms on addition of boron. This can be exploited to produce an Mo_5Si_3 matrix material that includes a phase that exhibits high temperature ductility. $MoSi_2$ and Mo_3Si are two possible ductile phases. Inclusion of a phase that exhibits ductile behavior at high temperature has the potential to reduce catastrophic failure due to blunting of cracks that form under high temperature service conditions.

The region of interest on the 1600°C isotherm of the Mo-Si-B phase diagram is shown in Figure 1. Possible ternary microstructures are a) MoB + $MoSi_2$ + T1, b) MoB + T1 + T2, and c) Mo_3Si + T1 + T2. There have been several studies[22,23,24,25,26,27] concerning the high temperature creep behavior and slip systems in tetragonal $MoSi_2$. There has not, however, been general agreement on the availability of the 5 independent slip systems[28] required for general plastic deformation.[29] Although we know of no creep deformation studies of Mo_3Si, other materials with the same primitive cubic A15 crystal structure have been of interest for some time as superconducting materials and more recently as high temperature structural materials.[30,31,32] Several studies have investigated creep behavior and slip systems, and all have reported <100> type Burgers vectors. In V_3Si single crystal studies, the slip plane has generally been reported as (100).[33,34] {001}<100> slip with formation of stacking faults between dislocation pairs has been observed in Nb_3Al alloys that exhibited yielding and subsequent plastic flow behavior.[35] Some recent studies of Nb_3Al,[36,37] have established {012}<100> slip.

The system chosen for creep experiments was the ternary T1 + Mo_3Si + T2. Since

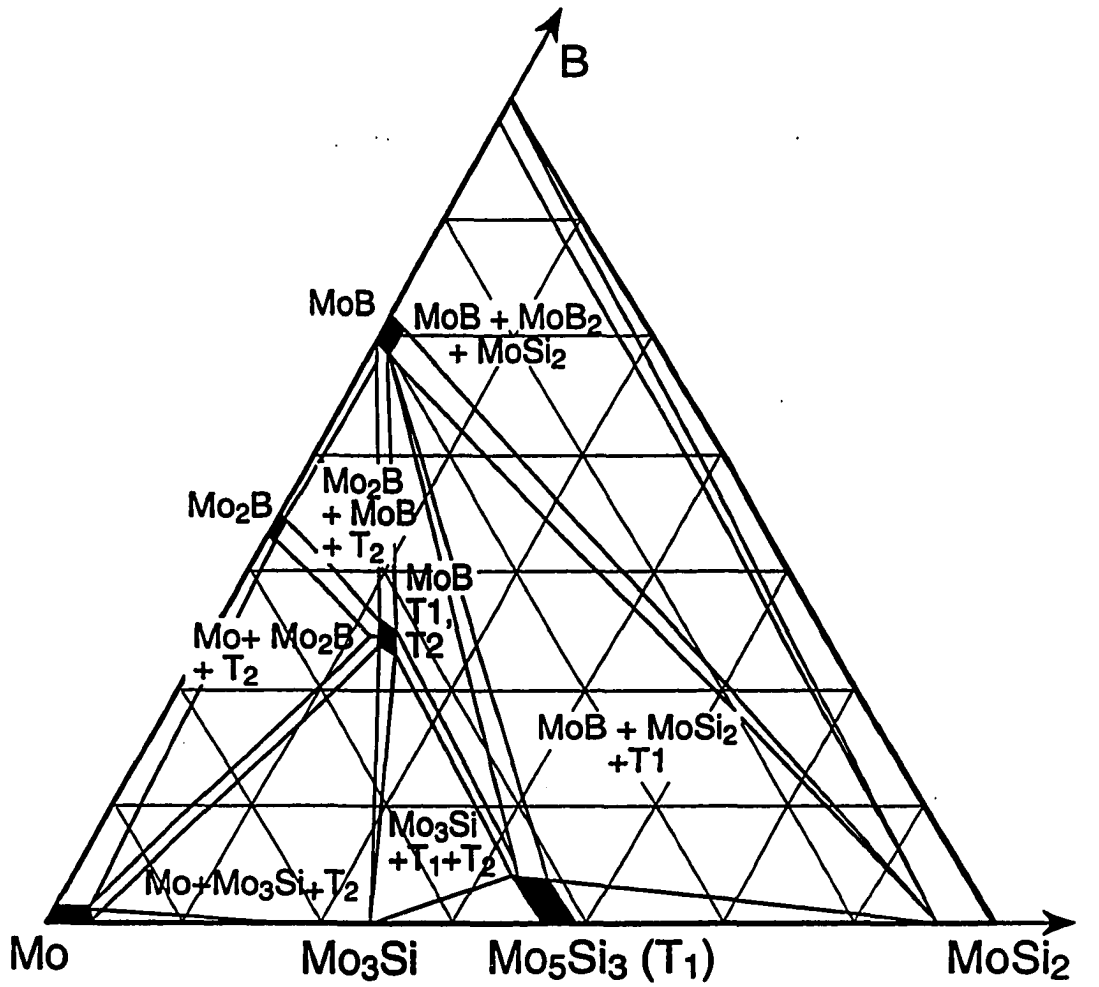

Figure 1. Molybdenum rich area of Mo-Si-B phase diagram at 1600°C (after Nowotny[17]).

Mo_3Si is a cubic phase, it is expected to exhibit the five independent slip systems necessary to satisfy von Mises' criterion for arbitrary plastic deformation more easily than tetragonal $MoSi_2$.

II. Experimental Procedure

(1) Sample Preparation

Mo_5Si_3 and boron doped Mo_5Si_3 were synthesized by arc melting of the elements in a non-consumable tungsten arc melt furnace under argon atmosphere. Boron doping formed a three phase material that will be subsequently referred to as B2. X-ray diffraction was performed to verify the phase array. Molybdenum, silicon, and boron content were verified by using ICP-AES (Inductively Coupled Plasma-Atomic Emission Spectroscopy). Results of chemical analysis are shown in Table I.

Table I. Elemental analysis of B2 creep specimens.

Element	wt. %	at. %
Molybdenum	85.7±2.6	60.5±2.7
Silicon	13.0±0.4	31.4±1.4
Boron	1.3±0.04	8.1±0.4

Arc melt buttons were ground to submicron size powders in an impact mill (Model 2000 Mixer/Mill, SPEX Industries, Edison, NJ). After milling, powders were sieved through -635 mesh (<20 μm) and dry pressed into right circular cylinders at 158 MPa (23,500 psi). B2 pellets were sintered at 1800°C for two hours under argon to a bulk density of 97.8% of

theoretical. Mo_5Si_3 was sintered at the same profile to 96% theoretical density. Final dimensions of creep specimens were 5 mm in diameter by 5 mm in length. Prior to creep testing, ends of creep specimens were polished flat and parallel.

(2) Creep Testing

Creep testing was conducted under constant stress using a feedback controlled servo motor system. The load necessary for a constant stress was calculated by assuming a constant volume to adjust for changes in sample area as the specimen deformed. Calculated in this way, stress was kept constant to within 1% for the duration of the creep run. Sample chamber temperature was measured with a type R thermocouple and kept constant to within ±2°C. Samples were deformed between silicon carbide platens. Platens were lubricated with hexagonal boron nitride spray prior to each run to minimize barrelling. All creep was carried out in a sealed system under flowing argon. Creep tests were carried out in the temperature range 1220°-1320°C and the stress range 140 -180 MPa (20.3 -26.1 ksi). Creep specimens were held at constant stress and temperature until approximately 1% strain was observed, at which time temperature was increased 20°C, and another data point taken. Total strain on each sample was 5-7%. Time for 1% strain ranged from 1 to 27 hours for the range of conditions tested. Creep behavior was modelled using a simplified power law creep equation:

$$(1) \qquad \dot{\varepsilon} = A\sigma^n \exp\left(\frac{-Q_a}{RT}\right).$$

to determine stress dependence and activation energy. In Equation (1) A is a parameter which incorporates the diffusion constant, Burgers vector magnitude, and

grain size dependence of creep, treated as constant throughout this work. Q_a is the apparent activation energy for creep, σ is the creep stress, and n is the creep stress exponent.

(3) Characterization

Microstructures of samples were characterized before and after creep testing by scanning electron microscopy (SEM, JSM 6100, JEOL USA, Peabody, MA) energy dispersive spectroscopy (EDS, Pentafet, Oxford Instruments, Oak Ridge, TN) and transmission electron microscopy (TEM, Philips CM30, Philips Instruments, Eindhoven, Netherlands). One B2 creep specimen was made by cutting two vertical faces on a cylindrical specimen parallel and flat with a diamond saw. The flat sides were metallographically polished and inspected by SEM prior to deformation. The creep sample required repolishing after the creep test due to formation of a thin surface oxide layer, so that direct one to one correspondence of grains before and after creep was not possible. The same areas of the specimen were examined after creep strains of 3.4, 5.6, and 13.3 percent to observe creep induced cracking and to measure changes in porosity. Image analysis was carried out on digitally acquired micrographs to determine phase composition and the amount of porosity present before and after deformation. Ninety-five percent confidence intervals for porosity were established using Student's t distribution. Confidence intervals are wide due to the distribution of pore area from surface to center of the specimens. X-ray powder diffraction patterns (XRD, Scintag XDS 2000, Scintag USA, Sunnyvale, CA) were taken from the same powders that creep samples were prepared from, and from specimens before and after creep to verify that no changes in the phase assemblage occurred during creep. Because many diffraction peaks overlap in the ternary system, diffraction patterns were deconvoluted and then indexed using least squares lattice parameter refinement.

TEM specimens were prepared from sections cut along the axis of applied stress with a diamond saw. Sections were core drilled and mechanically dimpled to perforation. Final thinning was completed by ion milling for 2 hours on a liquid nitrogen cooled stage at -100°C.

III. Results and Discussion

(1) Microstructural Analysis

An SEM back scattered electron image (BSE) of a typical sintered creep sample is shown in Figure 2(a), showing a three phase microstructure composed of tetragonal Mo_5Si_3 (T1, JCPDS 34-371), cubic Mo_3Si (JCPDS 4-814), and tetragonal $Mo_5(Si,B)_3$ (T2, JCPDS 9-0292). An etched specimen is shown in Figure 2(b). Murakami's reagent was used here to selectively etch the T2 phase, since BSE contrast of Mo_3Si and T2 were almost identical. SEM/EDS analysis indicates that the dark matrix phase is Mo_5Si_3, the etched phase producing intermediate BSE signal is the T2 phase, and the bright phase is Mo_3Si. The presence of these three phases was confirmed by x-ray and elecron diffraction. Image analysis of the microstructure shows that the T1 matrix makes up 54% by volume, while Mo_3Si and T2 are approximately equally represented in the remainder. Image analysis showed that sintered samples contained 2.2 percent porosity prior to creep.

Table II gives the deformation history of the sample shown in Figure 2. The specimen was repolished after each succesive deformation to remove a thin oxide scale that formed due to residual oxygen in the chamber of the creep appartus. Porosity of the specimen decreased to 1.5 percent after 3.8% strain was introduced, indicating that a portion of the measured deformation was associated with elimination of porosity. There is no noticeable change in grain size or shape for any of the three phases and no SEM evidence

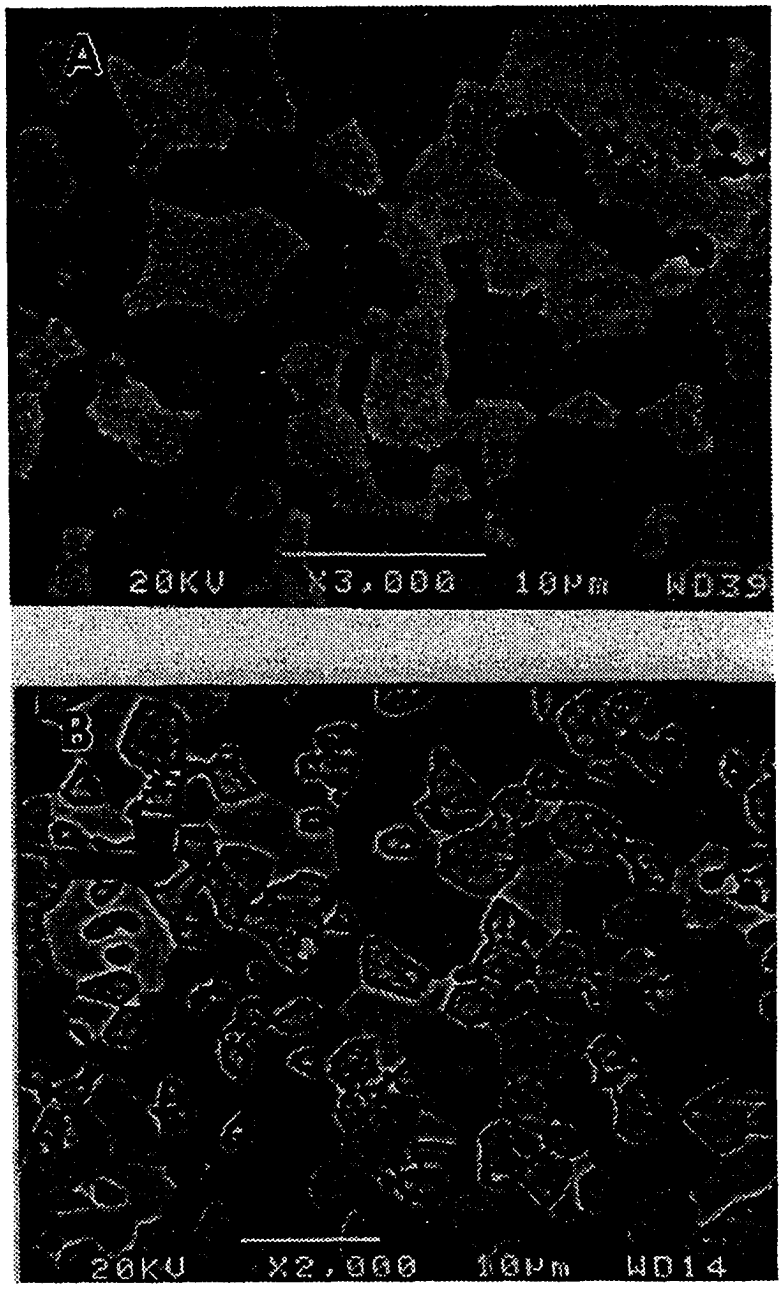

Figure 2. Microstructure of specimen B2 before and after creep. (a) No deformation, unetched, (b) no deformation; etched with Murakami's etch to enhance contrast between T2 and Mo_3Si. (continued next page).

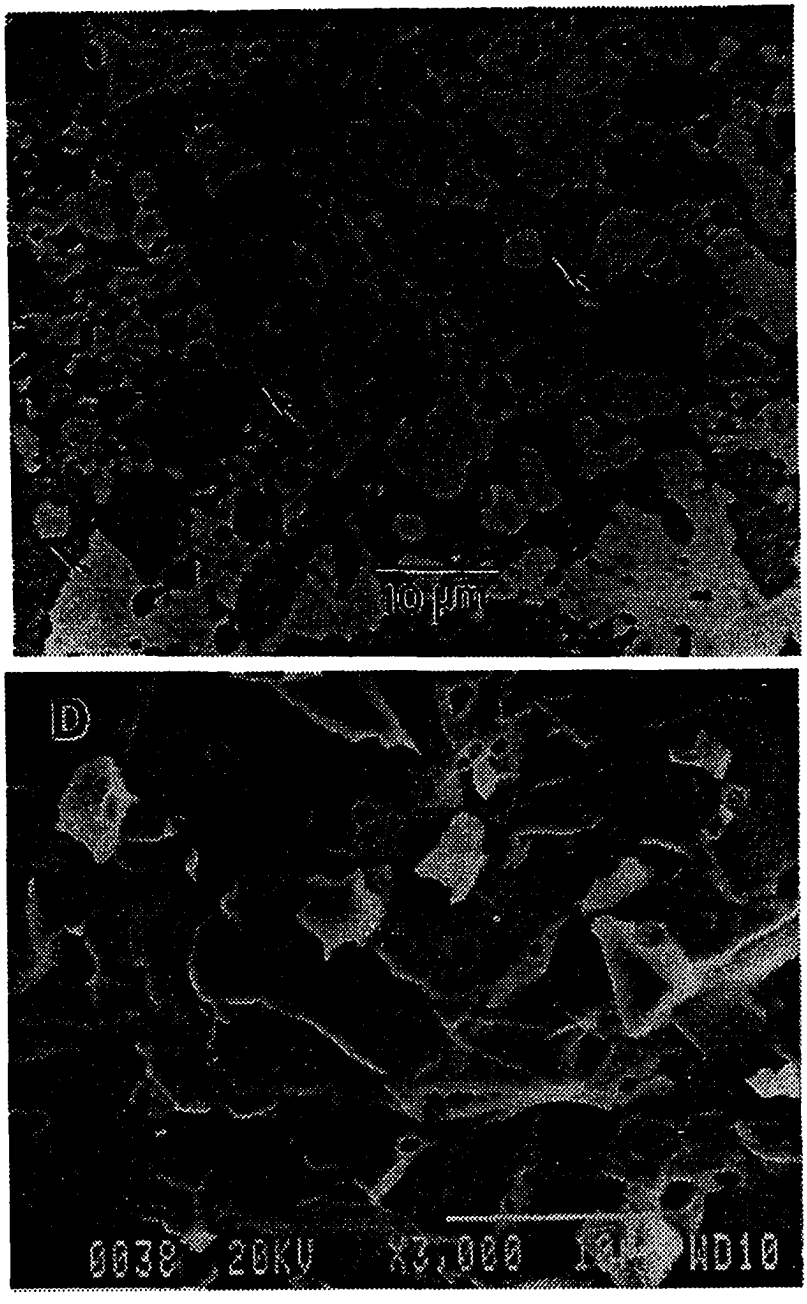

Figure 2. (continued from previous) (c) polished section after 13.3% strain showing cracking in Mo_5Si_3 and lack of cracks in T2 and Mo_3Si, (d) longitudinal fracture surface after 13.3% strain. Fracture is transgranular.

Table II. Deformation history of creep sample shown in Figure 2.

Strain Range, %T.S.	Deformation Temp., °C	Deformation Stress, MPa	Porosity, Vol. % (±95% C.I.)	Micro-Cracking Observed
no creep			2.2 (±0.4)	N
0-3.8	1300	148	1.5 (±0.4)	N
3.8-5.6	1240-1320	180	2.6 (±1.0)	N
5.6-13.3	1320	140	3.3(±0.4)	Y

for development of new grain boundary porosity due cavitation creep processes at this strain. After creep to 5.6% strain, the microstructure of the specimen appeared similar to that at 3.8% strain, with no macro or microstructural cracking noted. After creep to 13.8% strain a large macroscopic crack formed in the sample, and approximately 10% of the sample volume chipped off on handling. Figure 2(c) shows the microstructure after 13.8% strain. Measured porosity was 3.3%. At this strain, the sample shows extensive cracking of the T1 matrix, while the occurrence of cracks in the Mo_3Si and T2 phases is much lower. Cracks that extend through T1 grains stop at the boundaries with the other phases. The sample was fractured parallel to the axis of applied load for microstructural evaluation. A micrograph of the fracture surface is shown in Figure 2(d). Fracture is transgranular, with no microstructural evidence for the formation of classical[38,39] grain boundary porosity due to cavitation during compressive creep.

(2) Creep Rates

A typical creep plot for boron modified Mo_5Si_3 is shown in Figure 3. This creep data was taken during the initial deformation (0-3.8% strain) of the creep sample in Figure 2. Creep curves did not exhibit well defined primary and secondary regions. Figure 4 shows a plot of strain rate versus strain. Figure 4 indicates that the specimen is in the steady state creep regime during the majority of the experiment. All regression lines fit to creep data had correlation coefficients (R^2) better than 0.98.

Creep rates for temperatures from 1220°-1320°C and loads of 138-180 MPa are plotted as a function of reciprocal temperature in Figure 5. No appreciable creep was measured for the combination of stresses less than 100 MPa and temperatures of less than 1200°C. Apparent activation energies were obtained from a least squares fit to the data in Figure 5. These activation energies are tabulated in Table III, and fall in the range 386-412 MPa. This indicates the same or similarly activated creep processes dominate the creep behavior throughout this regime. Also included in Figure 5 is the temperature dependence of the creep of Mo_5Si_3 at 140 MPa. The creep rate of Mo_5Si_3 is slightly slower than that of B2 under the same deformation conditions. Activation energies are similar. Figure 6 shows calculated creep stress exponents for B2, along with errors associated with the calculation of the stress exponent. The stress exponent appears to decrease with increasing temperature from a value of 5.0 at 1242°C to a value of 3.7 at 1302°C. The errors associated with the calculation of the stress exponent are on the order of 0.5 to 0.7 and prevent any conclusions as to change in creep mechanism with applied stress from being drawn from this data. The average stress exponent for all conditions tested is 4.3. Stress exponents in this range often indicate creep by dislocation related processes.

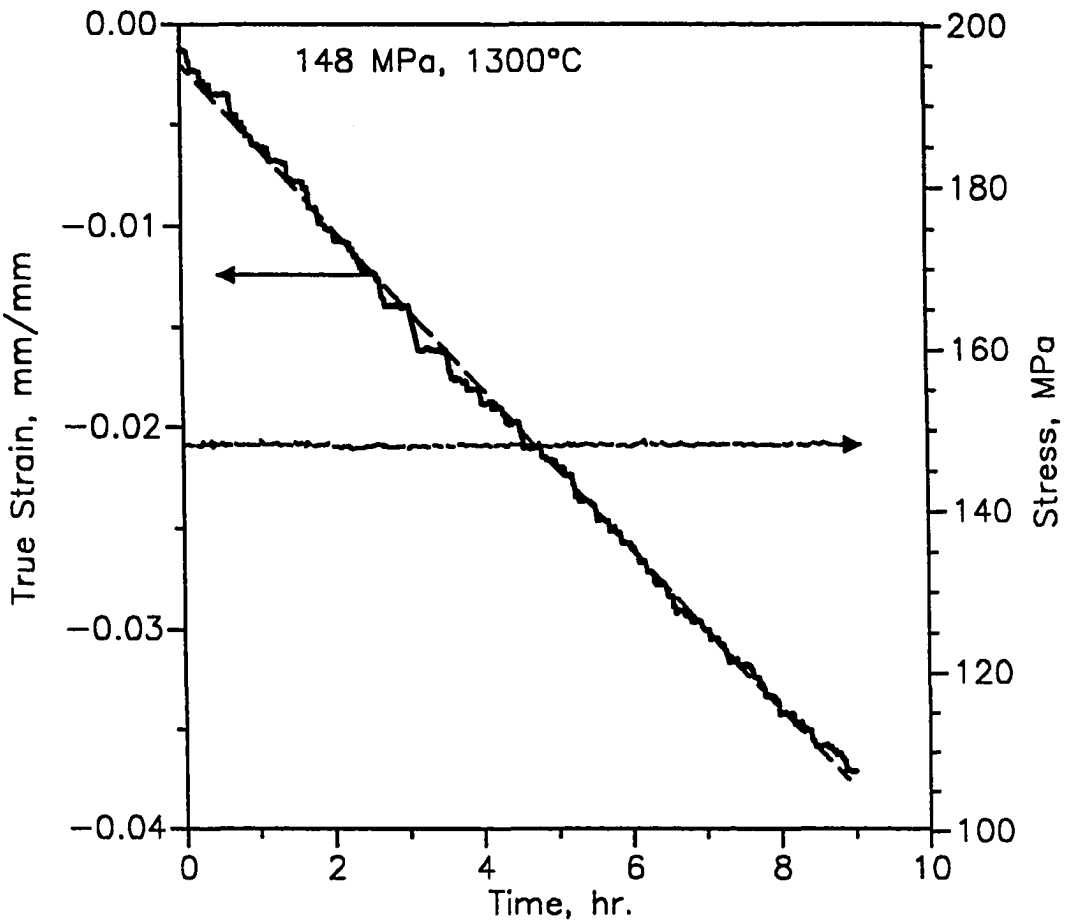

Figure 3. Typical Creep Curve for B2. Creep rate is 1.11×10^{-6} s^{-1} at 148 MPa and 1300°C.

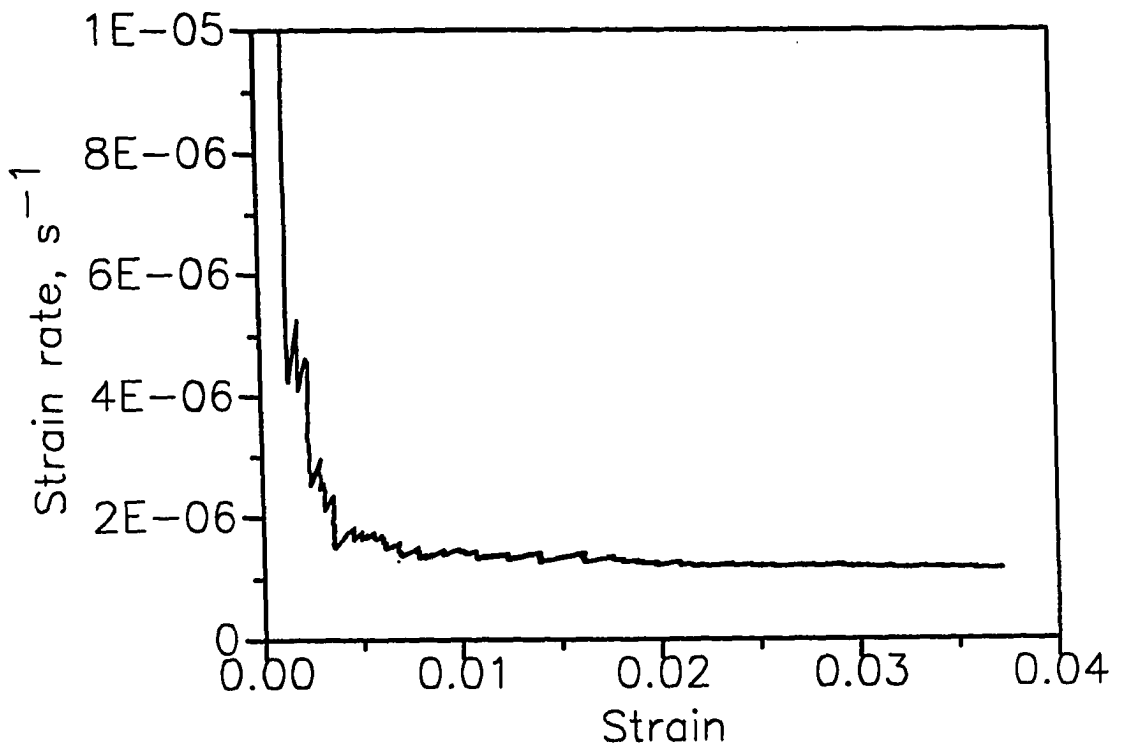

Figure 4. Plot of strain rate as a function of strain for data of Figure 4. Specimen is in steady state creep regime for majority of test.

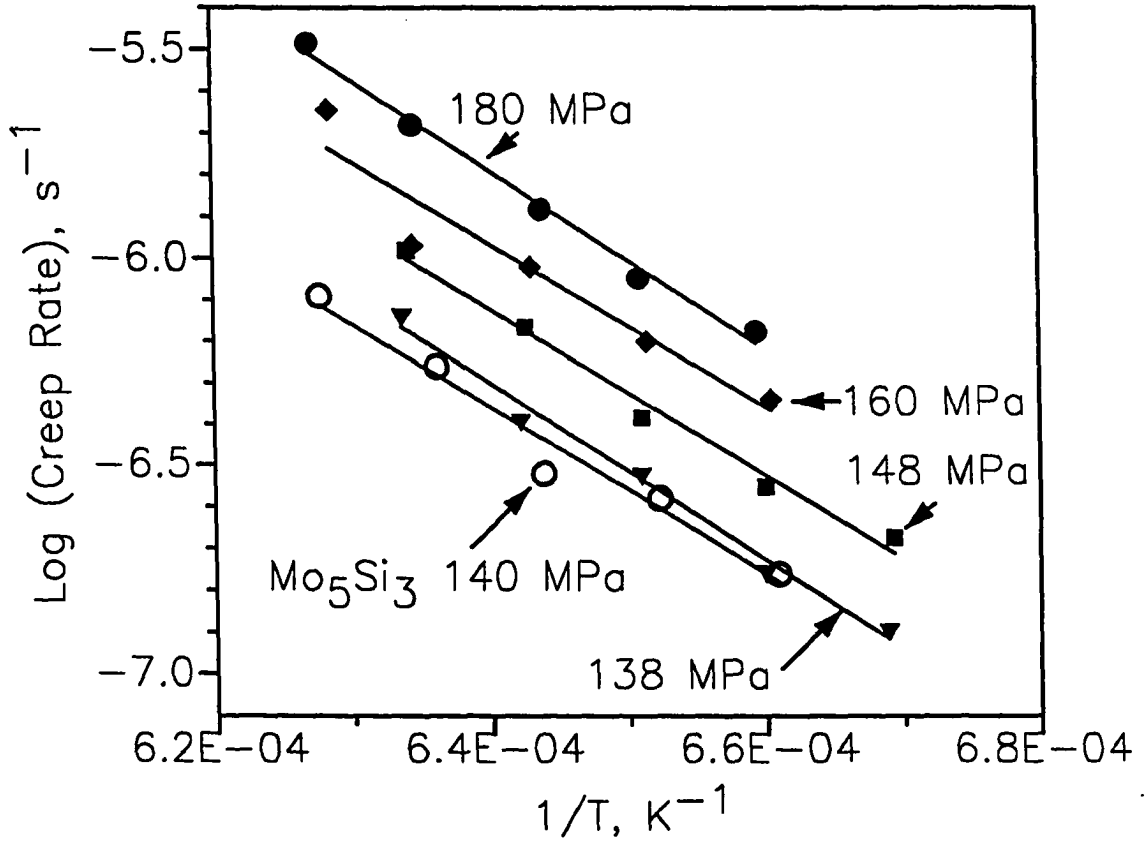

Figure 5. Arrhenius plot of the steady state rate constants for the creep of Mo_5Si_3 with and without boron additions. Filled symbols are B2, open symbols are Mo_5Si_3.

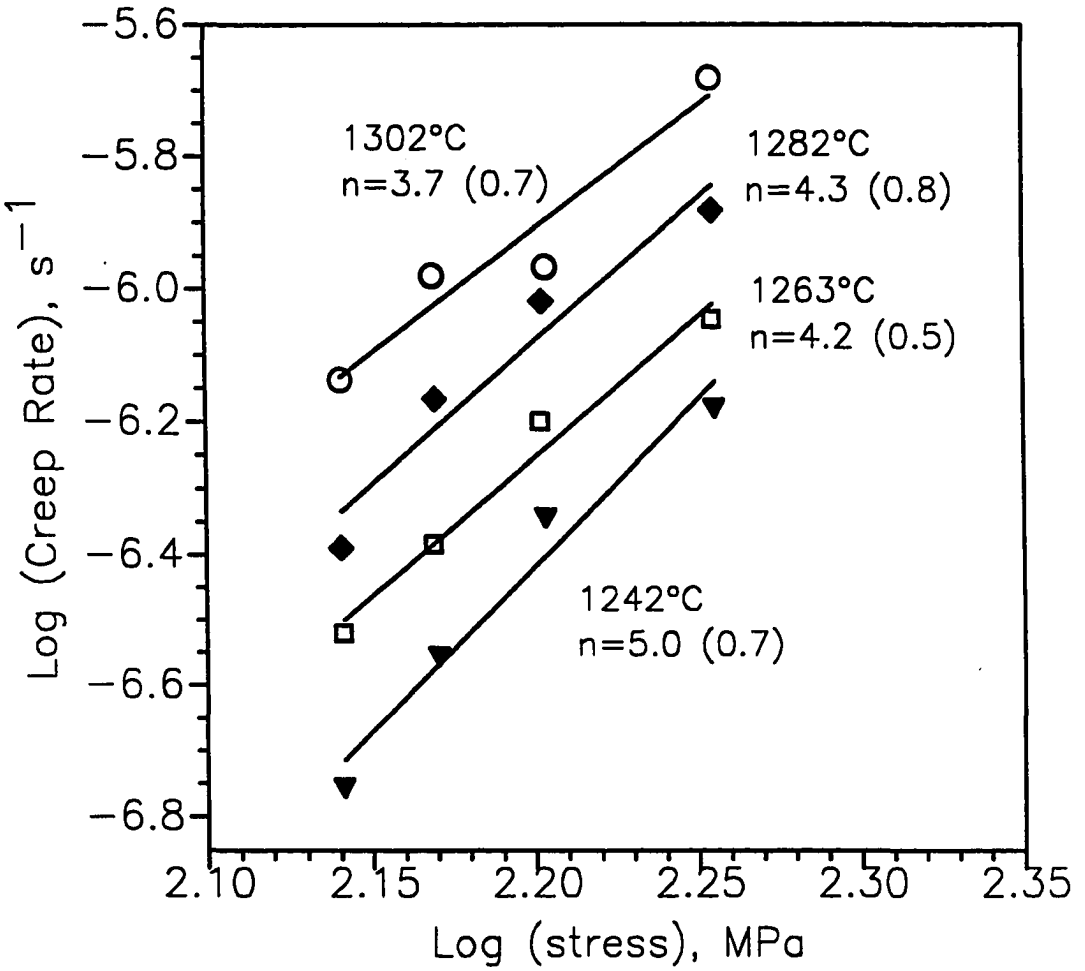

Figure 6. Stress dependence of the creep rate for B2 from 1242°-1302°C.

Table III. Apparent activation energies for creep.

Creep Stress, MPa	Activation Energy, KJ/mol
B2	
138	407
148	386
160	377
180	412
Mo_5Si_3	
140	399

(3) Effect of Porosity on Creep Rate

Experimentally, the creep strain due to elimination of porosity can be separated from the creep strain due to other creep processes if the change in density is known. The fractional creep strain due to creep processes excluding changes in porosity can be expressed as:[40]

(2) $$\varepsilon_e = 1/3(3\varepsilon_z - \Delta\rho/\rho)$$

where ε_e is the creep strain due to processes not involving pores or cavitation, ε_z is the recorded uniaxial strain, and $\Delta\rho/\rho$ is the fractional density change due to elimination or

creation of porosity. The theoretical density of material used in this study is 8.2 g/cm^3. Using equation (2), of the 3.8% longitudinal strain recorded for initial deformation of the specimen of Figure 2, 3.6% was due to creep processes other than elimination of porosity, while the remaining 0.2% was due to reduction of porosity during creep. If the strain due to reduction in porosity is subtracted from the strain due to other creep processes a 'true' creep rate can be calculated. This ratio of the 'true' creep rate to the porous creep rate in this case is 1.06. This indicates that closure of porosity accelerated the creep rate of B2 by about six percent.

(4) TEM Analysis of Crept Microstructure

Low magnification TEM bright field images of B2 before and after 5.0% deformation are shown in Figure 7(a) and 7(b) respectively. It was observed that grain size as shown in the TEM was much finer than the grain size observed in SEM/BSE imaging. SAD (selected area diffraction) patterns taken on neighboring grains indicate that there are clusters of grains aligned to within a few degrees of each other over areas of several μm^2. This subgrain structure must be a remnant of powder processing and sintering, since it appears in both the deformed and undeformed microstructures. It is apparent from Figure 7 that pore coalesence has occured during deformation. Prior to deformation, nearly spherical pores 0.1-0.3 μm in size are distributed along grain boundaries. The post deformation pore size is 0.3-3 μm, with pores more often found at three grain junctions and as elogated voids between grains. The appearance of larger voids in the microstructure indicates that pullout of small grains has occurred in agreement with the noted increase in porosity (Table II). Room temperature post creep fracture after large strains was transgranular. This may indicate that fracture has occurred along creep

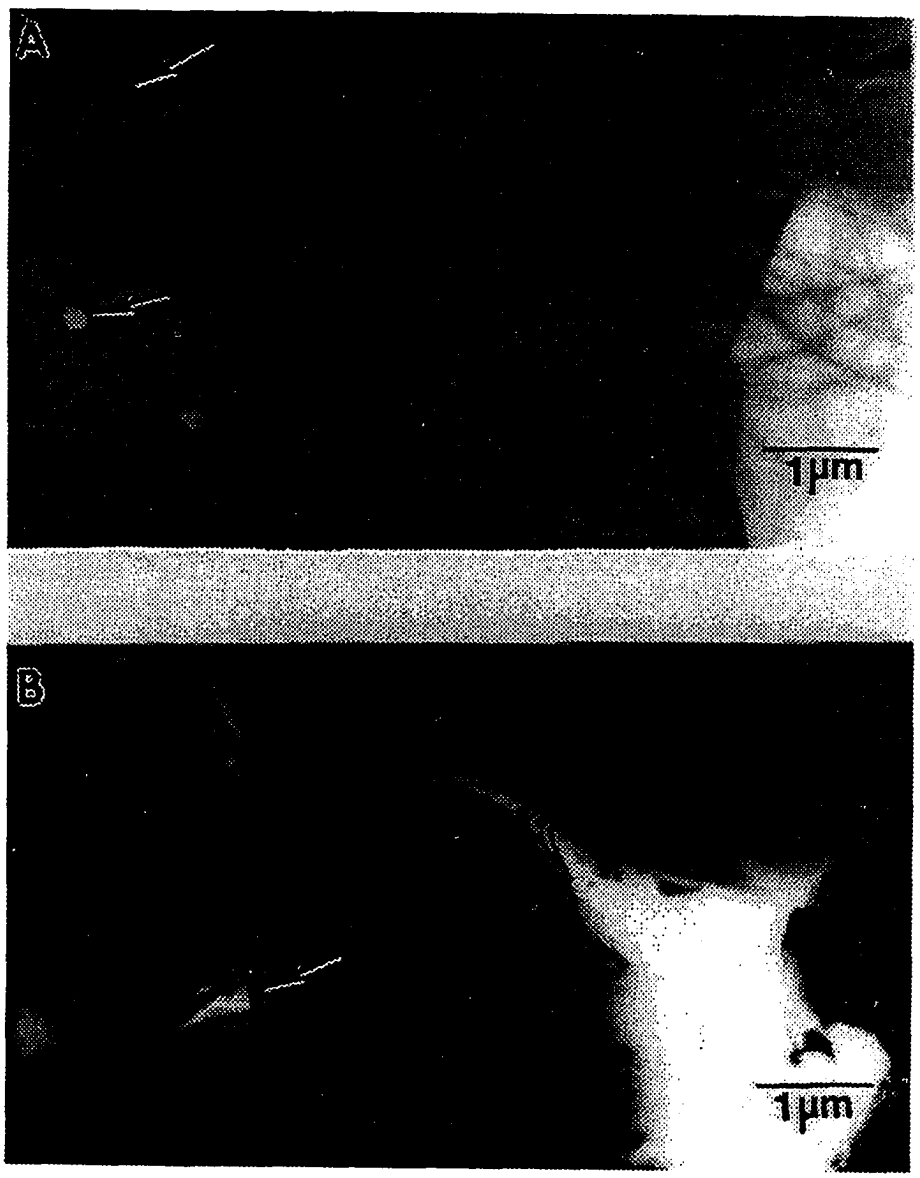

Figure 7. Low magnification TEM brightfield images of microstructure before deformation and after 5.0% strain. (a) undeformed microstructure (b) deformed microstructure.

induced cracks in the T1 phase and continued along junctions of these cracks with Mo_3Si and T2 grains.

A higher magnification TEM brightfield image of an Mo_5Si_3 grain after 5.0% strain is shown in Figure 8. No dislocations were observed in the Mo_5Si_3 matrix phase. TEM evidence for dislocation activity was found in the T2 phase during TEM investigation. Figure 9 shows a weak beam darkfield image of dislocations typical in the T2 phase. Beam direction in this image is near [001]. Stereographic analysis shows that dislocations marked A, B and C have line directions of $[\bar{1}30]$, $[\bar{1}10]$, and $[\bar{2}10]$ respectively. Imaging of these dislocations was carried out using several **g** vectors. Isotropic extinction criteria (**g.b** analysis) was used to determine Burgers vectors. Dislocations A were out of contrast for **g** of $(\bar{1}10)$ and in contrast for $(\bar{1}00)$, (010), (110), $(\bar{1}\bar{1}0)$, $(\bar{2}\bar{1}1)$, and $(\bar{1}01)$. Dislocation B was out of contrast for $(\bar{1}01)$ and in contrast for the other imaging conditions given above. No clear extinction conditions were noted for dislocation C. Based on extinction conditions it is possible that dislocation A in Figure 9 has a [110] Burgers vector, and dislocation B a [010] Burgers vector. These are the shortest unit translation vectors available in the unit cell. Dislocation A would then be pure edge dislocation, while B is within 10 degrees of being pure edge. Both systems operate in the basal plane. The foil normal for the crystal in Figure 9 is 17° from [001], and the strain axis is in the plane of the micrograph, so that the critical resolved shear stress on (001) is large. It is not suprising that {100} slip systems are activated. The {001}<010> and {001}<110> systems combined give only 2 independant slip systems[41] so that additional slip systems not observed here must be activated for intragranular plastic deformation to occur without cracking.

Mo_3Si exhibited a high density of dislocations after creep relative to the other phases present. The dislocation structure is qualitatively similar to that of deformed metals, with grains divided into well defined subgrains containing free dislocations. An example

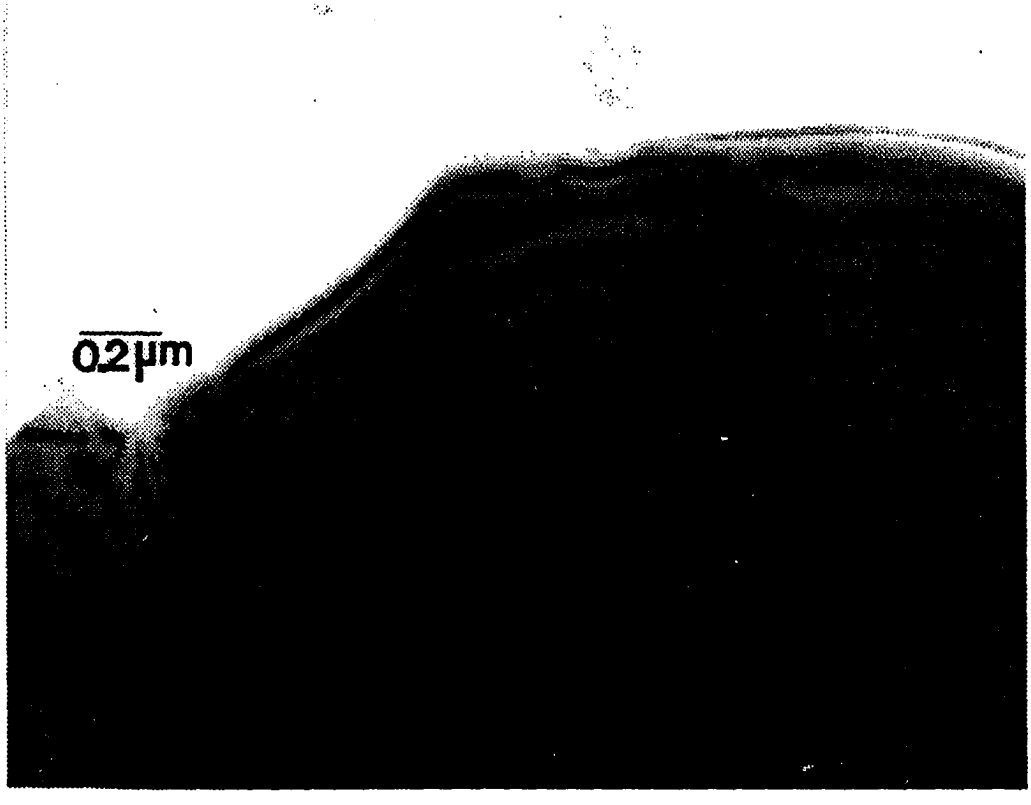

Figure 8. Higher magnification TEM brightfield image of T1 grain. No dislocations were found in T1.

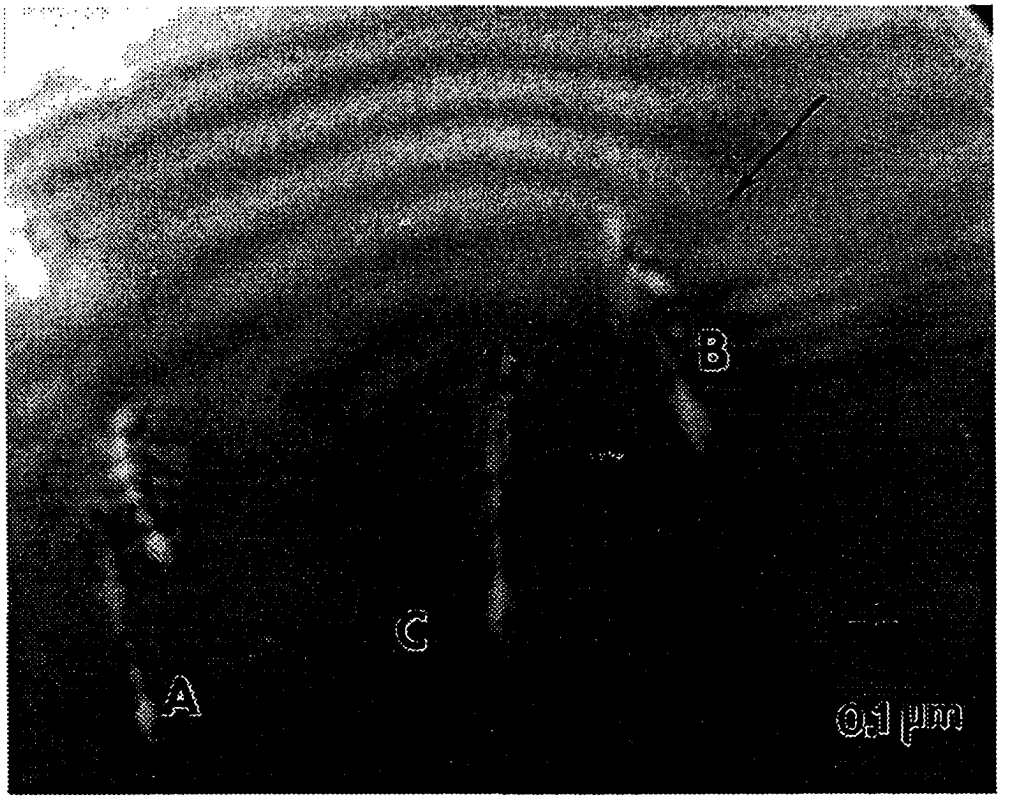

Figure 9. TEM weak beam darkfield image of dislocations in T2 phase. Arrow indicates g=(121), foil normal 17° from [001].

of this subgrain structure is shown in Figure 10 for a grain oriented 23° from [001]. Two types of dislocation networks were noted. The first, indicated by the arrows in Figure 10, is a well developed subgrain boundary. The second is a loose network of nearly perpendicular dislocations, ie. the predecessor to the subgrain boundary. This indicates that polygonization is actively occuring in Mo_3Si at 5% strain, and is evidence for dislocation climb. Dislocations A, B, and C in Figure 10(a) were found to lie in $[\bar{1}\,\bar{1}\,0]$, $[\bar{1}\,10]$, and $[\bar{2}10]$ directions respectively. Extinction conditions for dislocations A and C were well defined as shown in Figure 11. Dislocation B exhibited residual contrast under all imaging conditions which varied in intensity as dislocation C came in and out of contrast. In Figure 11(a), dislocation A is out of contrast while B and C are in contrast for $\mathbf{g}=(100)$. In 11(b), A is in contrast and B and C are in out of contrast for $\mathbf{g}=(02\bar{1})$. Further imaging conditions are listed in Table IV. Based on Table IV and duplication of extinction conditions at other zone axes, the Burgers vector determined by isotropic extinction criteria is $[0\bar{1}0]$ for the $[\bar{1}\,\bar{1}\,0]$ line direction (A), giving a mixed character and an (001) glide plane. Dislocations B and C have a $[\bar{1}00]$ Burgers vector, again indicating mixed dislocations with an (001) glide plane. The observed (001)<100> slip system for Mo_3Si is consistent with previous work on V_3Si. Observed dislocation systems for the phases present are summarized in Table V.

(5) Rate Controlling Mechanism

The value of creep stress exponents obtained in this study were in the range n=3.8-5.0. Stress exponents in this range and the observation of dislocations in Mo_3Si and T2 suggest that dislocation related processes are rate controlling processes during creep.

Table IV. Imaging and observed extinction conditions for Mo_3Si.

g	Dislocation contrast		
	A	B	C
$\bar{1}00$	OUT	IN	IN
$1\bar{1}0$	IN	IN	IN
$\bar{1}20$	IN	IN	IN
$0\bar{2}1$	IN	OUT	W.
$\bar{2}01$	OUT	IN	IN
$12\bar{1}$	IN	IN	IN
$2\bar{1}0$	IN	IN	IN
$1\bar{2}0$	IN	IN	IN
$0\bar{1}1$	IN	OUT	W.
100	OUT	IN	IN
$02\bar{1}$	IN	OUT	OUT

Table V. Summary of observed dislocation systems.

Phase	Relative Dislocation Density	Observed Slip Systems
Mo_5Si_3	very low	none
T2	moderate	{001}<010>
		{001}<110>
Mo_3Si	highest	{001}<100>

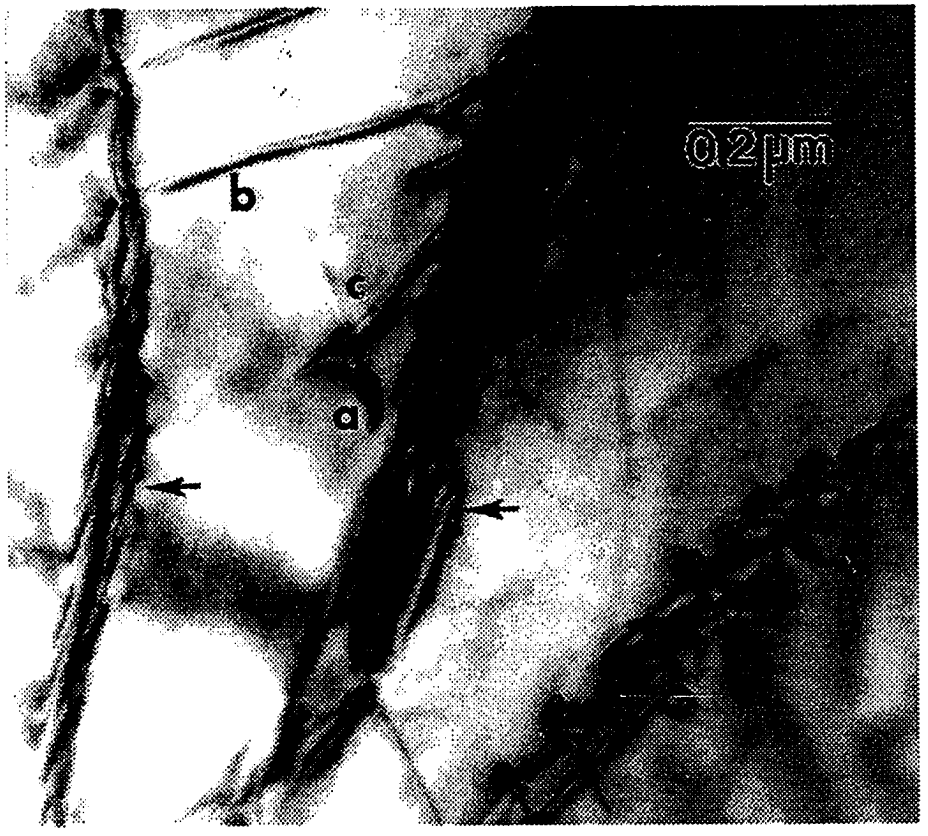

Figure 10. TEM weak beam darkfield image of dislocation structures in Mo_3Si. Arrows indicate subgrain boundaries.

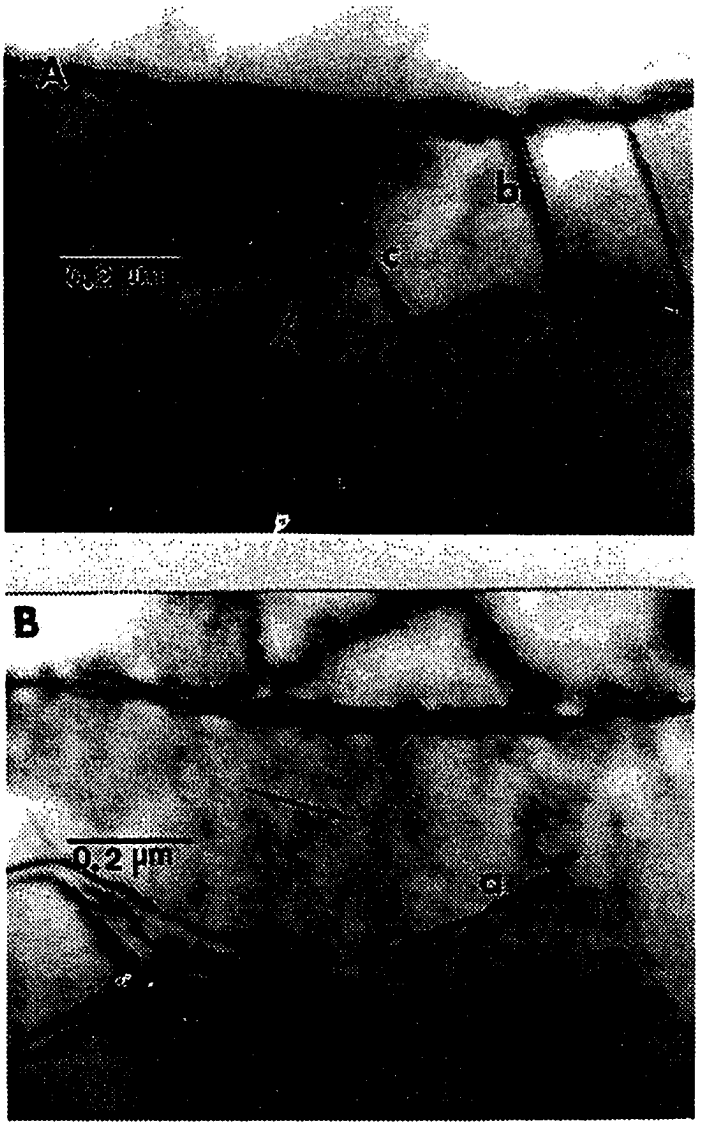

Figure 11. Isotropic extinction criteria for Mo_3Si. Arrow indicates g. (a) g=(100), dislocation A out of contrast. (b) B and C out of contrast for g=$(02\bar{1})$.

Theoretical models that generate stress exponents of 4 or 5 are mechanisms in which creep rate is controlled by dislocation climb.[42] The lack of dislocation activity in the T1 phase, the cracking behavior of T1 at large strains, the lack of extensive cracking in T2 and Mo_3Si, and the relative creep rates of Mo_5Si_3 and B2 suggest that T1 is acting as a creep resistant phase in the ternary system. French, et al.[43] have modelled creep in duplex microstructures using standard composite theory. The duplex microstructure is modeled as an assemblage of lamellar plates of alternating phases. The alignment of the plates is either parallel to the stress axis for the isostrain case, or perpendicular to the stress axis for the isostress case. Good agreement was found for predictions of the isostrain model to experimental data for 50 volume percent composites of cubic zirconia and alumina and YAG with alumina. The isostrain model predicts that creep of each phase will be coupled and occur at the same rate. The more creep resistant material will then bear a larger portion of the stress than the 'soft' phase, and the measured creep rate of the composite will be intermediate to that of the end members. If stress exponents for the two phases are similar, the creep rate changes slowly with changes in volume fractions of the phase assemblage.

Analogous logic can be applied to a ternary system if it is considered to be an assemblage of two soft phases and one hard phase or two hard phases and one soft phase. At small strains, the rate limiting deformation mechanism for the three phase B2 material appears be plastic deformation due to dislocation motion within the Mo_3Si and/or T2 phases. The creep rate may be decreased below that of monolithic Mo_3Si or T2 by partitioning of stress onto the creep resistant Mo_5Si_3 phase. At small strains ($\approx$3%) sliding and rotation of T1 grains may be accomodated by softer phases. Accomodation of T1 grain motion by a soft phase would account for the lack of cracking and cavitation at small strains. At larger strains ($\approx$13%) the T1 phase did exhibit cracking, indicating that grain motion was not

completely accomodated. The fact that cracks nucleating in T1 did not propagate through T2 and Mo_3Si suggests that these phases exhibit resistance to crack growth due to ductile behavior at high temperatures. Although Mo_3Si and T2 do not appear to have adequate slip systems for arbitrary plastic deformation, dislocations analysis was conducted on grains favorably oriented for {001} slip. These observations do not preclude the possibility that other slip systems may be operating.

IV. Summary

A three phase Mo_5Si_3 matrix material composed of tetragonal Mo_5Si_3 (T1), Mo_3Si, and a $Mo_5(Si,B)_3$ (T2) phase was synthesized by powder processing and sintering at 1800°C. The addition of boron was previously shown to substantially improve oxidation resistance of Mo_5Si_3. Creep tests indicate that the effect of boron on creep resistance is small. Specimens were creep tested in compression at 1240°-1320°C and stresses of 140-180 MPa. The average activation energy for creep in the temperature range 1220°-1320°C was 396 KJ/mol. An average stress exponent of 4.3 suggests that dislocation climb is the rate controlling deformation mechanism. No dislocations were found in the T1 phase. Basal plane dislocations were observed in the T2 phase, and {001}<100> dislocations were observed in Mo_3Si. At small strains, the rate limiting deformation mechanism for the three phase B2 material appears be plastic deformation due to dislocation motion within the Mo_3Si and/or T2 phases. The creep rate may be decreased below that of Mo_3Si or T2 by partitioning of stress onto the creep resistant Mo_5Si_3 phase.

After 13.3% deformation, microstructural cracking was observed in T1. These cracks did not in propagate through Mo_3Si or T2, indicating that these phases stopped crack growth, apparently due to ductile behavior at high temperature.

Acknowledgement: Ames Laboratory is operated for the U.S. Department of Energy by Iowa State University under contract number W-7405-ENG-82. This research was supported by the Office of Basic Energy Science, Materials Science Division.

References

[1]R.M. Aiken Jr., "On the Ductile-to Brittle Transition Temperature in $MoSi_2$," *Scr. Metall. Mater.*, **26** [7] 1025-30 (1992).

[2]D.P. Mason, D.C. Van Aken, "The Effect of Microstructural Scale on the Hardness of $MoSi_2$-Mo_5Si_3 Eutectics," *Scr. Metall. Mater.*, **28** [2] 185-89 (1993).

[3] S.R. Srinivasan, R.B. Schwarz, "Elastic Moduli of $MoSi_2$ Based Materials," *J. Mater. Res.*, 7 [7] 1610-13 (1993).

[4]G. Sauthoff, "Intermetallic Phases as High Temperature Materials," *Z. Metallkd.*, 77 [10] 554-66 (1986).

[5]C.D. Wirkus, D.R. Wilder, "High-Temperature Oxidation of Molybdenum Disilicide," *J. Am. Ceram. Soc.*, **49** [4] 173-77 (1966).

[6]R.E. Regan, W.A. Baginski, C.A. Krier, "Oxidation Studies of Complex Silicides for Protective Coatings," *Cer. Bull.*, **46** [5] 502-9 (1967).

[7] E. Fitzer, "Oxidation of Molybdenum Disilicide," in Ceramic Transactions vol. 10: Corrosive and Erosive Degradation of Ceramics, ed. R.B. Tressler and M. McNallan, American Ceramic Society, Westerville, OH (1989).

[8]C.G. McKamey, P.F. Tortorelli, J.H. DeVan, C.A. Carmichael, "A Study of Pest Oxidation in Polycrystalline $MoSi_2$," *J. Mater. Res.*, 7 [10] 2747-55 (1992).

[9]P.J. Meschter, "Low-Temperature Oxidation of Molybdenum Disilicide," *Metall. Trans.*, **23A** [6]1763-72 (1992).

[10]T.C. Chou, T.G. Nieh, "Mechanism of $MoSi_2$ Pest During Low Temperature Oxidation," *J. Mater. Res.*, **8** [1] 214-27 (1993).

[11]B.F. Gilp, P.D. Desai, C.Y. Ho, Bibliography on Silicides, MIAC Report 3, Metals Information and Analysis Center, West Lafayette, IN (1993).

[12]S. Bose, "Engineering Aspects of Creep of Molybdenum Disilicide," *Mater. Sci. Eng.*, **A155** [1-2] 217-25 (1992).

[13]J.J. Petrovic, "$MoSi_2$-Based High-Temperature Structural Silicides," *MRS Bull.*, **18** [7] 35-40 (1993).

[14]International Tables for Crystallography, eds. T. Hahn, A.J. Wilson, Kluwer Academic Publishers, Norwell, MA (1992).

[15]Binary Alloy Phase Diagrams, ed. T. Massaslki, ASM International, Materials Park, OH (1990).

[16]H. Nowotny, E. Parthe', R. Kieffer, F. Benesovsky, " Das Dreistoffsystem: Molybdan-Silizium-Kohlenstoff," *Monatsh. Chem.*, **85** 255-72 (1954).

[17]H. Nowotny, E. Dimakopoulu, H. Kudielka, "Untersuchungen in den Dreistoffsystemen: Molybdan-Silizium-Bor, Wolfram-Silizium-Bor und in dem System: VSi_2-TaSi," *Monatsh. Chem.*, **88** 180-92 (1957).

[18]D.L. Anton, D.M. Shah, "High Temperature Properties of Refractory Intermetallics," *Mat. Res. Soc. Symp. Proc.*, **213** 733-39 (1991).

[19] R.W. Bartlett, J.W. McCamont, P.R. Gage, "Structure and Chemistry of Oxide Films Thermally Grown on Molybdenum Silicides," *J. Am. Ceram. Soc.*, **48** [11] 551-58 (1965).

[20]J.B. Berkowitz-Mattuck, R.R. Dils," High Temperature Oxidation; II. Molybdenum Silicides," *J. Electrochem. Soc.*, **112** [6] 583-89 (1965).

[21]A.J. Thom, M.K. Meyer, M. Akinc, Y. Kim, "Evaluation of $A_5Si_3Z_x$ Intermetallics for Use as High Temperature Structural Materials," in Processing and Fabrication of Advanced Materials for High Temperature Applications-III, ed. T.S. Srivatsan and V.A. Ravi. The Minerals, Metals, and Materials Society, Warrendale, PA (1993).

[22]Y. Umakoshi, T. Hirano, T. Sakagami, T. Tamanee,"Slip Systems and Hardness in $MoSi_2$ Single Crystals," *Scr. Metall,*. **23** [1] 87-90 (1989).

[23]Y. Umakoshi, T. Sakagami, T. Hirano, T. Yamane, "High Temperature Deformation of $MoSi_2$ Single Crystals with the C11b Structure," *Acta. Metall. Mat.*, **6** 909-15 (1990).

[24]K. Kimura, M. Nakamura, T. Hirano, "High Temperature Deformation Behavior of $MoSi_2$ and WSi_2 Single Crystals," *J. Mat. Sci.*, **25** 2887-92 (1990).

[25]O. Unal, J.J. Petrovic, D.H. Carter, T.E. Mitchell, "Dislocations and Plastic Deformation in Molybdenum Silicide," *J. Am. Ceram. Soc.*, **73** [6] 1752-57 (1990).

[26]T.E. Mitchell, R.G. Castro, J.J. Petrovic, S.A. Maloy, O. Unal, M.M. Chadwick, " Dislocations, Twins, Grain Boundaries, and Precipitates in $MoSi_2$," *Mat. Sci. Eng.*, **A155** 241-49 (1992).

[27]S.A. Maloy, A.H. Heuer, J.J. Lewandowski, T.E. Mitchell, "On the Slip Systems in $MoSi_2$," *Acta. Metall. Mater.*, **40** [11] 3159-65 (1992).

[28]R. Von Mises, *Z. Angew. Math. Mech.*, **8** 161 (1928).

[29]K. Ito, H. Inui, M. Yamaguchi, "Plastic Deformation of $MoSi_2$ Single Crystals," submitted to *Phil. Mag.*, (1994).

[30]D.M. Shah, D.L. Anton, "Evaluation of Refractory Intermetallics with A15 Structure for High Temperature Structural Applications," *Mat. Sci. Eng.*, **A153** 402-409 (1992).

[31]P. Paufler, E. Zedler, H.-J. Ullrich, K.-H. Berhtel, U. Kramer, M. Jurisch, K. Richter, K. Eichler, "Influence of Chemical Composition within the Range of Homogeniety on Phase Transition and Transition Temperature of V_3Si Single Crystals. II. On the Defect Structure of V_3Si Single Crystals," *Phys. Stat. Sol.*, **44** 499-504 (1977).

[32]J.W. Newkirk, J. A. Sago, "Ductile Phase Toughening of Cr_3Si with Chromium," *Mat. Res. Soc. Symp. Proc.*, **194** 183-89 (1990).

[33]H.J. Levinstein, E.S. Greiner, H. Mason, Jr.," Observation of Dislocations in V_3Si Single Crystals," *J. Appl. Phys.*, **37** [1] 164-66 (1966).

[34]U. Essman, H. Haag, G. Zerweck, "Dislocations in V_3Si," *Comm. Phys.*, **2** 127-130 (1977).

[35]Y. Murayama, T.Kumagai, S. Hanada, "Processing and High Temperature Deformation of Nb_3Al," *Mat. Res. Soc. Symp. Proc.*, **288** 95-106 (1993).

[36]M. Aindow, J. Shyue, T.A. Gaspar, H.L. Fraser, " Concerning the Dissociation of Grown-In Dislocations in Melt Spun Ribbons of the Intermetallic Compound Nb_3Al," *Phil. Mag. Lett.* **64** [2] 59-65 (1991).

[37]L.S. Smith, M. Aindow, M.H. Loretto, "Microstructures, Defects, and Deformation Mechanisms in Vanadium Modified Nb_3Al," *Mat. Res. Soc. Symp. Proc.*, **322** 453-58 (1994).

[38]C.R. Blanchard, K.S. Chan, "Evidence of Grain-Boundary-Sliding-Induced Cavitation in Ceramics under Compresssion," *J. Am. Ceram. Soc.*, **76** [7] 1651-60 (1993).

[39]M.N. Menon, H.T. Fang, D.C. Wu, M.K. Ferber, K.L. More, C.R. Hubbard, T.A. Nolan, "Creep and Stress Rupture Behavior of an Advanced Silicon Nitride: Part I, Experimental Observations,"*J. Am. Ceram. Soc.*, **77** [5] 1217-27 (1994).

[40] R. Raj, "Separation of Cavitation-Strain and Creep-Strain During Deformation," *J. Am. Ceram. Soc.*, **65** [3] C-46 (1982).

[41]J.D. Cotton, M.J. Kaufman, "A Simplified Method for Determining the Number of Independant Slip Systems in Crystals," *Scr. Met.*, **25** 2395-98 (1991).

[42]A.H. Choksi, T.G. Langdon, "Characteristics of Creep Deformation in Ceramics," *Mat. Sci. Tech.*, **7** [7] 577-84 (1991).

[43]J.D. French, J. Zhao, M.P. Harmer, H.M. Chan, G.A. Miller, "Creep of Duplex Microstructures," *J. Am Ceram. Soc.*, **77** [11] 2857-65 (1994).

CHAPTER 5: GENERAL CONCLUSION

I. Oxidation Behavior

The oxidation of Mo_5Si_3 at 800°C is catastrophic, showing low temperature pest behavior similar to that seen in $MoSi_2$. In the range 900°-1100°C, oxidation proceeds with a mass loss due to volatilization of molybdenum oxide. Inspection of the scale by SEM confirms that the scale formed is cracked and porous, with many short circuit paths for oxygen diffusion. Experimentally, it was shown that the scale provides little protection from transport of oxygen to the oxidation interface, since i) oxidation proceeds by mass loss with no molybdenum rich inter layer formation and ii) large amounts of MoO_x crystals form in the scale. Oxidation at 900°-1100°C appears to be controlled by the outward diffusion of $(MoO_3)_x$. Oxidation at 1200°C is very rapid, with complete conversion to silica occurring in less than one hour.

Small boron additions have a major effect on the oxidation resistance of molybdenum rich silicides. The oxidation resistance of Mo_5Si_3 is decreased approximately 5 orders of magnitude by less than 2 weight percent boron addition. The oxidation behavior of molybdenum rich Mo-Si-B compositions was studied using x-ray diffraction, thermogravimetric analysis, and microscopic observation of the scale at different stages of growth. Experiments were conducted to determine oxidation behavior as a function of both temperature and composition.

Oxidation tests were conducted as a function of temperature for the composition (wt%) 82.0% Mo, 16.1% Si, 1.24% B. SEM observation of the scale shows that a glassy, non porous scale is formed after oxidation for long times (≈300 hr.) at temperatures from 800°-1300°C. Oxidation occurs with mass gain above 1050°C, and kinetics fit a parabolic

model. Formation of a molybdenum interlayer occurs at all temperatures tested. The activation energy for oxidation was measured to be 134 kJ/mol in the temperature range 1050°-1300°C, and compares well with the activation energy for diffusion of oxygen in borosilicate glass. The rate limiting step in oxidation in the range 1050°-1300°C appears to be oxygen diffusion through the scale. This evidence indicates that the reason for the improved oxidation resistance of boron modified compounds is the formation of a coherent scale due to glass modification by boron.

Oxidation tests as a function of composition were conducted for compositions ranging from (wt%) 81.2% to 88.2% molybdenum. All compositions showed an initial transient period of mass gain due to oxidation of molybdenum and silicon followed by rapid mass loss starting near 750°C due to volatilization of MoO_3. The magnitude of the transient mass loss was found to be proportional to the atomic fraction of molybdenum present in the substrate. The atomic fraction of molybdenum controls the amount and size of porosity in the scale as it initially forms. More and/or larger pores allow faster (short circuit) diffusion of oxygen to the oxidation interface.

After the rapid kinetics of the initial transient oxidation period, a slower 'steady state' regime was reached. The isothermal oxidation rate was found to scale inversely with the ratio B/Si. ESCA results indicate that compositions with high B/Si ratios form scales with high B/Si ratios. Glass viscosity decreases as the ratio of B/Si increases, indicating that at 1000°C time dependent lateral flow is important in providing a passivating oxide layer. Phase array of the substrate coupon does not have a major effect on long term oxidation behavior.

The initial transient oxidation period and transition to steady state behavior were modelled by using glass sintering theory to describe the closure of porosity by densification of the scale as a function of time at the oxidation temperature. The effective

diffusion of oxygen through the pores was approximated by Knudsen diffusion. It was found that the predictions of the model qualitatively agree with experimental results.

II. Creep Behavior

Creep testing was performed on a three phase Mo_5Si_3 matrix material synthesized by powder processing and sintering. The material was composed of tetragonal Mo_5Si_3 (T1), Mo_3Si, and a ternary $Mo_5(Si,B)_3$ (T2) phase. Composition was (wt%) 85.7% Mo, 13.5% Si, and 1.3% B. Creep tests indicate that the effect of boron on creep resistance is small. The average activation energy for creep in the temperature range 1220°-1320°C was 396 KJ/mol. An average stress exponent of 4.3 suggests that dislocation climb is the rate controlling deformation mechanism. No dislocations were found in the T1 phase. Basal plane dislocations were observed in the T2 phase, and {001}<100> dislocations were observed in Mo_3Si.

After 13.3% deformation, microstructural cracking was observed in T1. These cracks did not in propagate through Mo_3Si or T2, indicating that these phases stopped crack growth, apparently due to ductile behavior at high temperature. The creep rate of the three phase boron modified material was slightly faster than single phase Mo_5Si_3 tested under the same conditions. The mechanism for deformation of the three phase B2 material at small strains appears to be sliding of Mo_5Si_3 grains accomodated by plastic deformation within the Mo_3Si and/or T2 phases.

III. Outlook and Suggestions for Future Work

Mo_5Si_3 based materials hold promise for use as high temperature structural materials. Creep resistance of materials prepared by a low cost sintering process is as

good or better than the creep resistance of exotic $MoSi_2$ composites. Oxidation resistance is similar to published values for $MoSi_2$ to at least 1300°C. Improvements in hot strength,[41] hardness,[42] and creep resistance[43] have also been reported with Mo_5Si_3 additions to $MoSi_2$. All of these improvements in properties comes with little effort in optimizing composition and microstructure. In addition this work shows that there is the possibility for gains in high temperature fracture toughness due to the crack stopping ability of Mo_3Si (or $MoSi_2$) second phases. All of this evidence indicates that Mo_5Si_3 based materials should be the subject of further research. Some suggestions follow.

1) Higher temperature oxidation resistance studies of Mo_5Si_3 with boron additions. Although viscous flow due to boron is the reason for improvement in oxidation resistance at 800°C< T <1300°C this may come at the expense of high temperature oxidation resistance. The diffusion rate for oxygen through a borosilicate glass is much higher then for diffusion through pure vitreous silica. This is likely to cause an increase in oxidation rate as temperature is increased beyond 1300°C. It is possible, however, that B_2O_3 volatilizes from the scale at high temperatures, leaving a silica rich scale. In fact, this does seem to be occurring at 1200°C and 1300°C, where oxidation rates are lower than expected. Anecdotal evidence for this effect has also been provided by Schlichting[44] for the oxidation of silicon carbide with one weight percent boron addition, were it was found that the oxidation rate decreased in the range 1200°-1300°C relative to 1000°C. Evidence for this effect is also provided by the fact that the surface of the scales becomes boron depleted after long times (Chapter 2). This may be especially true in wet atmospheres.

2) Investigation of electrical properties. One potential application of these materials is for use as high temperature (T>800°C) heating elements. Mo_5Si_3 based

materials may be useable in applications were long unsupported spans are required. $MoSi_2$ heating elements are not suitable for these applications.

3) High temperature strength and fracture toughness testing. There exists the possibility for improvement in high temperature srength and fracture toughness due to the crack stopping ability of Mo_3Si or $MoSi_2$ phases. Strength enhancements due to alloying $MoSi_2$ with Mo_5Si_3 have already been noted. The high temperature mechanical properties of Mo_5Si_3 with T2 and Mo_3Si second phase are not known.

4) Investigations into creep behavior of single phase Mo_5Si_3, Mo_3Si, and T2 phases. Understanding of the creep behavior of the individual constituents will lead to predictive capability of the creep behavior of binary and ternary systems.

5) Investigations into the temperature dependence of hardness and elastic modulus. T2, Mo_5Si_3, and Mo_3Si have not been characterized. Several other interesting possibilities also exist. In particular, MoB is a very hard, high modulus phase that may increase high temperature wear resistance of the silicide.

6) The $Mo_5Si_3/MoSi_2$ system offers the opportunity for a modelling study of the creep behavior of two phase systems which incorporate a hard phase (Mo_5Si_3)and a phase that exhibits plasticity due to dislocation related processes ($MoSi_2$). In particular, the simple model suggested by French and Wiederhorn[45] could be tested for isostress and isostrain orientations of directionally solidified material.

ACKNOWLEDGEMENT

Ames Laboratory is operated for the U.S. Department of Energy by Iowa State University under contract number W-7405-ENG-82. This research was supported by the Office of Basic Energy Science, Materials Science Division. The United States government has assigned the DOE report number IS-T 1737 to this thesis.

I would like to dedicate this dissertation to my family. My wife Beth has always supported and encouraged me to continue my education, putting off her own priorities for me. Little Nolan has been very patient and understanding about Dad's extended working hours. I love them both dearly. My parents Bob and Millie, parent in-laws Lyle and Darla, and uncle Dale have seen us through the hard times, helping us when we needed help. I owe all of these people a great deal.

I would like to thank my major professor, Dr. Mufit Akinc. He has been a patient man, a wise mentor, a staunch advocate, and a good friend.

I would like to thank Andy Thom for valuable silicide discussions and a good laugh, and Yong Han for his interesting and objective perpectives.

Last, but not least, I would like to thank Dr. Scott Chumbley and Dr. Matt Kramer for technical help on questions related to microscopy.

GENERAL REFERENCES

[1]Jay R. Smyth, "Advanced Gas Turbines," p. 995-1002 in Engineered Materials Handbook, Volume IV: Ceramics and Glasses S. J. Schneider, Tech. Chair. ASM International, Materials Park, OH (1987).

[2]E.G. Butler, "Engineering Ceramics: Applications and Testing Requirements," in Mechanical Testing of Engineering Ceramics at High Temperatures, eds. B.F. Dyson, R.D. Lohr, R. Morrell. Elsevier Applied Science, New York (1989).

[3]S. Bose, "Engineering Aspect of Creep Deformation in Molybdenum Disilicide," *Mat. Sci. Eng.*, **A155** 217-25 (1992).

[4]International Tables for Crystallography, eds. T. Hahn, A.J. Wilson, Kluwer Academic Publishers, Boston (1992).

[5]L. Brewer, A.W. Searcy, D.H. Templeton, C.H. Dauben, "High Melting Silicides," *J. Am. Ceram. Soc.*, **33** 291 (1950).

[6]H. Nowotny, E. Parthe', R. Kieffer, F. Benesovsky, " Das Dreistoffsystem: Molybdan-Silizium-Kohlenstoff," *Monatsh. Chem.*, **85** 255-72 (1954).

[7]B. Aronsson, "The crystal structure of Mo_5Si_3 and W_5Si_3," *Acta Chem. Scand.*, **9** [7] 1107-1110 (1955).

[8]N. Christensen, "Preparation and Characterization of Mo_3Si and Mo_5Si_3," *Acta Chem. Scand.*, **37A** 519-22 (1983).

[9]E. Parthe', W. Jeitschko, V. Sadagopan, "A Neutron Diffraction Study of the Nowotny Phase Mo<5Si3C<1," *Acta Cryst.*, **19** 1031-37 (1965).

[10]A.W. Searcy, "Predicting the Thermodynamic Stabilities and Oxidation Resistances of Silicide Cermets," *J. Am. Ceram. Soc.*, **40** [12] 431-35 (1957).

[11]G. B. Cherniak, A. G. Elliot, "High Temperature Behavior of $MoSi_2$ and Mo_5Si_3", *J. Am. Ceram. Soc.*, **47** [3] 136-41 (1964).

[12]A.W. Searcy, A.G. Tharp, "Dissociation Pressures and Heats of Formation of the Molybdenum Silicides," *J. Phys. Chem.*, **64** [10] 1539-42 (1960).

[13]S. Maloy, A.H. Heuer, J. Lewandowski, J. Petrovic, "Carbon Additions to Molybdenum Disilicide: Improved High-Temperature Mechanical Properties," *J. Am. Ceram. Soc.*, **74** [10] 2704-6 (1991).

[14]D.L Anton, D.M. Shah, "High Temperature Properties of Refractory Intermetallics," *Mat. Res. Soc. Symp. Proc.*, **213** 733-39 (1991).

[15]S.R. Srinivasan, R.B. Schwarz, "Elastic Moduli of $MoSi_2$-based Materials," *J. Mater. Res.*, 7 [7] 1610-12 (1992).

[16]T. Y. Kosolapova, Handbook of High Temperature Compounds: Properties, Production, Applications. Hemisphere Publishing Corporation, New York (1990).

[17]R.L. Fleischer, "Review: High-Strength, High-Temperature Intermetallic Compounds," *J. Mater. Sci.*, **22** 2281 (1987).

[18]J.J. Petrovich, P.E. Honnell, "SiC Reinforced-$MoSi_2$/WSi_2 Alloy Matrix Composites," *Ceram. Eng. Sci. Proc.*, **11** [7-8] 734-44 (1990).

[19]E. Fitzer, " Oxidation of Molybdenum Disilicide," in Ceramic Transactions, Vol. 10: Corrosive and Erosive Degradation of Ceramics, eds. R.B. Tressler and M. McNallan. American Ceramic Society, Westerville, OH (1989).

[20]R.K. Wade, J.J. Petrovic, "Processing Temperature Effects on Molybdenum Disilicide," *J. Am. Ceram. Soc.*, **75** [11] 3160-62 (1992).

[21]C.D. Wirkus, D.R. Wilder, "High-Temperature Oxidation of Molybdenum Disilicide," *J. Am. Ceram. Soc.*, **49** [4] 173-77 (1966).

[22]R.E. Regan, W.A. Baginski, C.A. Krier, "Oxidation Studies of Complex Silicides for Protective Coatings," *Cer. Bull.*, **46** [5] 502-9 (1967).

[23]C.G. McKamey, P.F. Tortorelli, J.H. DeVan, C.A. Carmichael, "A Study of Pest Oxidation in Polycrystalline $MoSi_2$," *J. Mater. Res.*, **7** [10] 2747-55 (1992).

[24]P.J. Meschter, "Low-Temperature Oxidation of Molybdenum Disilicide," *Met. Trans.*, **23A** 1763-72 June 1992.

[25]T.C. Chou, T.G. Nieh, "Mechanism of $MoSi_2$ Pest During Low Temperature Oxidation," *J. Mater. Res.*, **8** [1] 214-27 (1993).

[26]T.C. Chou, T.G Nieh, "Mechanism of $MoSi_2$ Pest during Low Temperature Oxidation," *J. Mater. Res.*, **8** [1] 214-27 (1993).

[27]R.W. Bartlett, J.W. McCamont, P.R. Gage, "Structure and Chemistry of Oxide Films Thermally Grown on Molybdenum Silicides," *J. Am. Ceram. Soc.*, **48** [11] 551-58 (1965).

[28]A.J. Thom, Y. Kim, M. Akinc, "Effect of Processing on Oxidation of Ti_5Si_3," *Mat. Res. Soc. Symp. Proc.*, **288** 1037-42 (1993).

[29]Per Kofstad, High Temperature Corrosion, Elsevier Science, New York (1988).

[30]R. Beyers, "Thermodynamic Considerations in Refractory Metal-Silicon-Oxygen Systems," *J. Appl. Phys.*, **56** [1] 147-52 (1984).

[31]J.B. Berkowitz-Mattuck, R.R. Dils, "High-Temperature Oxidation; II. Molybdenum Silicides," *J. Electrochem. Soc.*, **112** [6] 583-89 (1965).

[32]A. Mueller, G. Wang, R.A. Rapp, E. L. Courtright, T. A. Kircher, "Oxidation behavior of Tungsten and Germanium-alloyed Molybdenum Disilicide Coatings," *Mat. Sci. Eng.*, **A155** 199-207 (1992).

[33]Karen L. Breitbach, Synthesis and Characterization of Nanocrystalline Silicide Compounds, M.S. Thesis, Iowa State University (1991).

[34]J.D. French, M.P. Harmer, H.M. Chan, G.A. Miller, "Coarsening Resistant Dual Phase Interpenetrating Microstructures," *J. Am. Ceram. Soc.*, **73** [8] 2508-10 (1990).

[35]B.R Lawn, A.G. Evans, D.B. Marshall, "Elastic/Plastic Indentation Damage in Ceramics: The Median Radial Crack System," *J. Am. Ceram. Soc.*, **63** [9-10] 574-81 (1980).

[36]A.G. Evans, E.A. Charles, "Fracture Toughness Determinations by Indentation," *J. Am. Ceram. Soc.*, **59** [7-8] 371-2 (1976).

[37]S.S. Chiang, D.B. Marshall, A.G. Evans, "The Response of Solids to Elastic/Plastic Indentation. I. Stresses and Residual Stresses," *J. Appl. Phys.*, **53** [1] 298-311 (1982).

[38]G.R. Anstis, P. Chantikul, B.R. Lawn, D.B Marshall, "A Critical Evaluation of Indentation Techniques for Measuring Fracture Toughness: I, Direct Crack Measurements and II. Strength Method," *J. Am. Ceram. Soc.*, **64** [9] 533-43 (1981).

[39]R. Raj, "Fundamental Research in Structural Ceramics for Service Near 2000°C," *J. Ame. Ceram. Soc.*, **76** [9] 2147-74 (1993).

[40]N. Birks, Introduction to High Temperature Oxidation of Metals, Edward Arnold, London (1983).

[41]R.B. Schwarz, S.R. Srinivasan, J.J. Petrovic, C.J. Maggiore, " Synthesis of Molybdenum Disilicide by Mechanical Alloying," *Materials Science and Engineering*, **A155** [1] 75-83 (1991).

[42]D.P.Mason, D.C. Van Aken, "The Effect of Microstructural Scale on the Hardness of $MoSi_2$-Mo_5Si_3 Eutectics," *Scr. Metall. Mater.*, **28** [2] 185-89 (1993).

[43]D.P. Mason, D.C. Van Aken, "Creep Deformation in Directionally Solidified $MoSi_2$-Mo_5Si_3 Eutectics," *Mat. Res. Soc. Symp. Proc.*, **288** 1129-34 (1993).

[44]J. Schlichting, K. Schwetz, "Oxidationsverhalten von Gesintertem α-Siliciumcarbid," *High Temp. High Press.*, **14** 219-23 (1982).

[45]J.D. French, J. Zhao, M.P. Harmer, H.M. Chan, G.A. Miller, "Creep of Duplex Microstructures," *J. Am. Ceram. Soc.*, 77 [11] 2857-65 (1994).